On the Scalar Scattering Theory for Thin-Film Solar Cells

On the Scalar Scattering Theory for Thin-Film Solar Cells

Proefschrift

ter verkrijging van de graad van doctor
aan de Technische Universiteit Delft,
op gezag van de Rector Magnificus prof.ir. K.C.A.M. Luyben,
voorzitter van het College voor Promoties,
in het openbaar te verdedigen
op maandag 26 november 2012 om 12:30 uur

door

Klaus JÄGER

Diplomphysiker ETH, Eidgenössische Technische Hochschule Zürich
geboren te Wörgl, Oostenrijk

Dit proefschrift is goedgekeurd door de promotor:
Prof.dr. M. Zeman

Copromotor:
Dr. R.A.C.M.M. van Swaaij

Samenstelling promotiecommissie:

Rector Magnificus,	*voorzitter*
Prof.dr. M. Zeman,	Technische Universiteit Delft, *promotor*
Dr. R.A.C.M.M. van Swaaij,	Technische Universiteit Delft, *copromotor*
Prof.dr. H.P. Urbach,	Technische Universiteit Delft
Prof.Dr.-Ing. D. Knipp,	Jacobs University Bremen, Duitsland
Prof.Dr.rer.nat. C. Rockstuhl,	Friedrich-Schiller-Universität Jena, Duitsland
Prof.dr. M. Topič,	Univerza v Ljubljani, Slovenië
Prof.dr.ir. M. Burgelman,	Universiteit Gent, België
Prof.dr. P.M. Sarro,	Technische Universiteit Delft, *reservelid*

The project described in this thesis was funded by Nuon Helianthos

Front cover photo by K. Jäger *Viewing South from the Hohe Ifen, Austria*
Back cover photo by T. van Dijk *The author with a flexible thin-film silicon module from Nuon Helianthos in between wafer-based silicon solar cells*
Typeset in Bera Sans and URW Palatino with LaTeX
Printed and bound in the Netherlands by Wöhrmann Print Service B.V., Zutphen

ISBN 978-94-6203-177-7

A digital copy is available at `http:\\repository.tudelft.nl`

To Willem-Jan

Preface

In September 2008, I started as a PhD student in the Photovoltaic Materials and Devices (PVMD) Laboratory. The goal of my PhD project was to develop a theoretical model that can describe scattering by nano-textured interfaces in thin-film solar cells. Further, the model should enable us to study the effect of nano-textured interfaces on the solar cell performance. I succeeded in doing so as I show in this thesis. I am convinced that we – the thin-film solar cell community – now understand scattering at nano-textured interfaces much better than four years ago, also because of the results presented in this thesis. My goal was to develop a scattering model based on rigorous physics that uses no or only very few empirical assumptions. However, I did not quite manage in formulating the scattering model as rigorously as I had wanted to. For example, I used a normalisation that works well for our purpose, but still is heuristic. I hope that people with new insights can put things on a more rigorous ground in the near future.

After keeping myself busy with renewable energy for many years I still believe that the transition of the global energy system towards a system that is fed solely from renewable sources is one of the most important issues of these times – and maybe one of the biggest challenges mankind has ever faced. The financial crisis that has been spreading across the whole western world for the last five years shows that we have to change our economical system such that sustainable long-term developments are more profitable than short-term results. Developing and implementing renewable energy conversion methods is one of the most important tasks in the work for a sustainable society. I am very grateful that I was given the chance to contribute to this field in the last years.

I would like to thank my promotor Professor Dr Miro Zeman, who accepted me as a PhD student even though I was a complete newcomer to solar cells. Miro, it was a great honour to work in your group and I am very grateful for everything that I learned from you. During my PhD project I spent hours in discussion with Associate Professor Dr René van Swaaij, so he finally was appointed as co-promotor. René, thank you very much for all the debates and critical views on my research, thank you that you were always ready to listen to my questions and thank you for letting me be your assistant in the *Advanced Semiconductor Device Physics* course for MSc students. Assistant Professor Dr Arno Smets, who was my next-door neighbour at the university during the last year, has my grateful acknowledgement for all the profound and often funny scientific discussions.

My appreciation goes to the external members of my *PhD defence committee*:

Professor Dr Paul Urbach, Professor Dr-Ing Dietmar Knipp, Professor Dr Carsten Rockstuhl, Professor Dr Marko Topič, Professor Dr Ir Mark Burgelmann, and Professor Dr Lina Sarro.

I also would like to thank all the *Post Docs* working at PVMD during the last four years: Dr Braňo Grančič, Dr Sergiy Dobrovolskiy, Dr Rudi Santbergen, Dr Sergey Solntsev, Dr Tristan Temple, Dr Karol Jarolimek, and Dr Do Yun Kim. Tristan, thank you for introducing me to the different deposition setups. Karol, thank you so much for all the nice discussions and conversations. Rudi, your background of optics helped me a lot in developing my model, thank you for all the conversations. Serge, thank you very much for sharing all your knowledge about modelling with me.

My colleague *PhD students*, it was a great honour and pleasure for me to work together with all of you: Dr Gijs van Elzakker, Bas Vet, Dr Michael Wank, Dr Karol Jarolimek (already mentioned above), Olindo Isabella, Dr Solomon Agbo, Joke Westra, Dong Zhang, Marinus Fischer, Pavel Babal, Guangtao Yang, Mirjam Theelen, Wendelin Sprenger, Jimmy Melskens, Mark Workum, Andrea Ingenito, Lihao Han, Hairen Tan, Ravi Vasudevan, Dimitris Deligiannis, and Martijn van Sebille. Thank you for coming to the PhD peer group meetings that helped enormously to make us a group not only of colleagues, but also of friends. Olindo, from the moment of my interview you made me feel very welcome. Thank you for introducing me to many experimental techniques during my first months and for the many discussions on light trapping issues. Marinus, I especially am grateful for all the discussions that led to many new ideas and for helping me with the renovation my apartment. Solomon and Lihao, you were my office mates. Thank you very much for being such a good company.

I had the honour to be the daily supervisor of five *students* during their MSc projects: Zhao Lu, Chare Ap Man Nek, Jeroen Sap, Michiel Wiggers, and Michail Ampatzis. With your work you contributed a lot to my research. I tried to be a good supervisor, however I did not always succeed; but by working together with you I learned much about supervising people. Thank you very much for your patience and I wish you all the best for your future careers.

My PhD project would not have been possible without all the *technical and support staff*: Laura Bruns, Iris de Jel, Rinske Koop, Marian Roozenburg-de Bree, Bianca Knot, and Marisya Lagendijk-Korzeniewski: thank you all for helping me with all the bureaucratic procedures and daily-life problems during the last four years. Martijn Tijssen, Stefaan Heirman, and Kaspar Zwetsloot, without your work as PVMD technicians the experimental part of my project could not have been completed. Jan-Chris Staalenburg, thank you very much for helping me to get a functioning IT infrastructure. Johan van der Cingel, thank you very much for all your help with the AFM system. Cassan Visser, I appreciate your support with the DekTak measurements. Robert Verhoeven, thank you for arranging the access to all the different rooms in DIMES. Emile van der Drift and Marc Zuiddam, thank you very much for letting me use the AFM system of the Kavli Lab.

During my PhD project I also had discussions with many scientists from other

research institutes and companies: Dr Melanie Schulte, Dr Carsten Bittkau, Dr Bart Pieters, and Markus Ermes from the Forschungszentrum Jülich: thank you for organising the project on scattering by TCO-silicon interfaces and making me part of it. Dr Janez Krč from the University of Ljubljana, thank you very much for all the discussions during your visits to Delft. Dr Corsin Battaglia from the EPFL in Switzerland (now UC Berkeley), thank you for debates on light trapping. Dr Franz-Josef Haug from the EPFL, you are gratefully acknowledged for several discussions on the scalar scattering theory. Dr Peter van Nijnatten, thank you very much for all the hours we spent on discussing the ARTA system. Dr Ivo Stemmler from Perkin Elmer Germany, thank you for organising the COSP workshop in Berlin. Professor Dr Arne Roos from Uppsala University, thank you for providing me with information on integrating sphere measurements.

I am very grateful to Nuon Helianthos for funding this PhD project. I want to express my special acknowledgement to Dr Gert Jan Jongerden and Dr Edward Hamers for initiating this project and for all the stimulating discussions we had during the progress meetings.

During this work I used several very helpful software packages licensed under open source: `gwyddion` for analysing AFM data, `FFTW` (Fastest Fourier Transform in the West) for performing the Fourier transforms in my scattering program, `gnuplot` for making scientific graphs, and – of course – LaTeX for typesetting. I want to express my gratitude to all the developers of these software packages.

Many excellent teachers helped me to get where I am now: OStR Mag Günther Lechner and Mag Elisabeth Tusch, who were physics teachers at the Bundesrealgymnasium (high school) Wörgl and gave me a profound background in physics – especially during the physics olympiad; Dr Wojciech Lipinski and Dr Helmut Katzgraber, who were the supervisors during my diploma (MSc) project.

Edwin, thank you for your help with designing the cover of this thesis.

Floris and Bart, you became good friends of mine during my stay in Delft. I am very happy and grateful that you agreed being the paranymphs at my PhD defence and that you will share this very special moment with me.

Katharina and Claudia , thank you very much for all the conversations we had and for all the advice you gave me during my visits to the Tyrol.

Alexander, without you mentioning TU Delft during a discussion in Zurich, I probably would not have come in contact with this excellent research group and my life would have looked very different.

Friedrich and Margareta, my dear parents, I cannot express in words how grateful I am for the upbringing, trust and love you gave me. Papa, thank you also very much for looking through my thesis from a linguistic point of view. Willem-Jan, thank you for standing firm as a rock in the stormy seas of my life.

Klaus JÄGER

Delft, the Netherlands
October 2012

Contents

Nomenclature

Abbreviations

ACF	autocorrelation function, m^2
AID	angular intensity distribution, a. u.
EQE	external quantum efficiency, –
FDTD	finite distance time domain method
FEM	finite elements method
FF	fill factor, –
HHCF	height-height correlation function, m^2
MST	modulated surface texture
ppm	parts per million
RCWA	rigorous coupled wave approach
TCO	transparent conductive oxide
TFSSC	thin-film silicon solar cell

Latin Letters

$\mathbf{B}$	magnetic induction, Vsm^{-2}
$\mathbf{D}$	electric displacement, Cm^{-2}
D	AFM scan size, m
d	layer thickness, m
$\mathbf{E}$	electric field, Vm^{-1}
E	energy, J
G	pupil function, m^{-1}

$\mathbf{H}$	magnetic field, Am^{-1}
H	haze, –
I	current, A
J	current density, Am^{-2}
$\tilde{k}$	refractive index (imaginary part), –
k, $\mathbf{k}$	wavenumber, wave vector, m^{-1}
K_x, K_y	coordinates in k-space, m^{-1}
ℓ	lateral feature size, m
ℓ_c	correlation length, m
m^*	effective mass, kg
n	refractive index (real part), –
P	power, W
p	power density, Wm^{-2}
R	reflectance, –
t	relaxation time, s
T	transmittance, –
U	complex scalar field, a. u.
V	voltage, V
z	height (function), m

German Letters

$\mathfrak{A}$	absorbance, –
$\mathfrak{N}$	particle density, m^{-3}
$\mathfrak{P}$	probability, –

Greek Letters

α	absorption coefficient, m^{-1}
β	phase, –
δ	datapoint distance, m

ϵ	electric permittivity, –
η	efficiency, –
θ	polar angle, scattering angle, –
κ	scaling constant, –
λ	wavelength, m
μ	magnetic permeability, –
ν	frequency, s^{-1}
Ξ	dummy variable (either T or R), –
σ_r	rms roughness, m
ς_{rel}	relative standard deviation
Φ	photon flux, –
ϕ	azimuth angle, –
χ	dielectric susceptibility, –
ψ	angle of incidence, transmittance, –
Ω	solid angle, –
ω	angular frequency ($\omega = 2\pi\nu$), s^{-1}

Subscripts

0	*in vacuo*
C	conduction band
dif	diffuse, scattered
f	final
g	bandgap
i	initial, incident
max	maximum
oc	open circuit
p	plasma
ph	photon

R	reflection
s	scattered
sc	short circuit
spec	specular
T	transmission
t	transmitted
tot	total
V	valence band

Constants

c_0	speed of light *in vacuo* (299 792 458 ms^{-1})
ϵ_0	vacuum permittivity ($8.854 \cdot 10^{-12}$ $\mathrm{AsV}^{-1}\mathrm{m}^{-1}$)
e	elementary charge ($1.602 \cdot 10^{-19}$ C)
h	Planck's constant ($6.626 \cdot 10^{-34}$ m^2 kg s^{-1})
μ_0	vacuum permeability ($4\pi \cdot 10^{-7}$ $\mathrm{VsA}^{-1}\mathrm{m}^{-1}$)

The beginning is a very delicate time.

Princess Irulan, Dune (film, 1984)

1 Introduction

Scattering* is everywhere. A billiard ball that hits the cushion is scattered. Bats orientate in space and locate prey with *echolocation*, *i.e.* by emitting ultra-sonic waves and analysing the scattered signals [1]. We can see objects when light that is scattered at them hits our eyes. The sky is blue because light is scattered at the molecules of air that are much smaller than the wavelength of the light. Since the strength of this so-called *Rayleigh scattering* is inversly proportional to the fourth power of the wavelength of the light, short wavelengths, *i.e.* the blue light, are scattered much stronger than long wavelengths [2, 3].

Clouds consist of trillions to quadrillions of little water droplets that are larger than the wavelength of light (radius between 2 and 10 µm). Therefore, the scattering (refraction) at such a droplet can be described with geometrical optics and is, in first order, independent of the wavelength. Light that traverses a cloud will be scattered many times. Due to this multiple scattering, the light field in the cloud is nearly independent of location and direction, it is called *homogeneous* and *isotropic*. Since all wavelengths are scattered at these droplets the cloud appears white. If the concentration of droplets is much smaller than in a cloud, such that the largest part of the light is scattered not more than once, a rainbow appears: The colors of the rainbow are due to the fact that the angles of refraction in a water droplet vary slightly with wavelength: the spectrum of the sunlight becomes visible. Sometimes, one also can see a second order rainbow. While the first order rainbow is blue inside and red outside, the second order rainbow is red inside and blue outside [3].

*In a very general definition, scattering is any deviation of a wave or a ray of particles from a straight trajectory due to an in-homogeneity of the medium through which they travel.

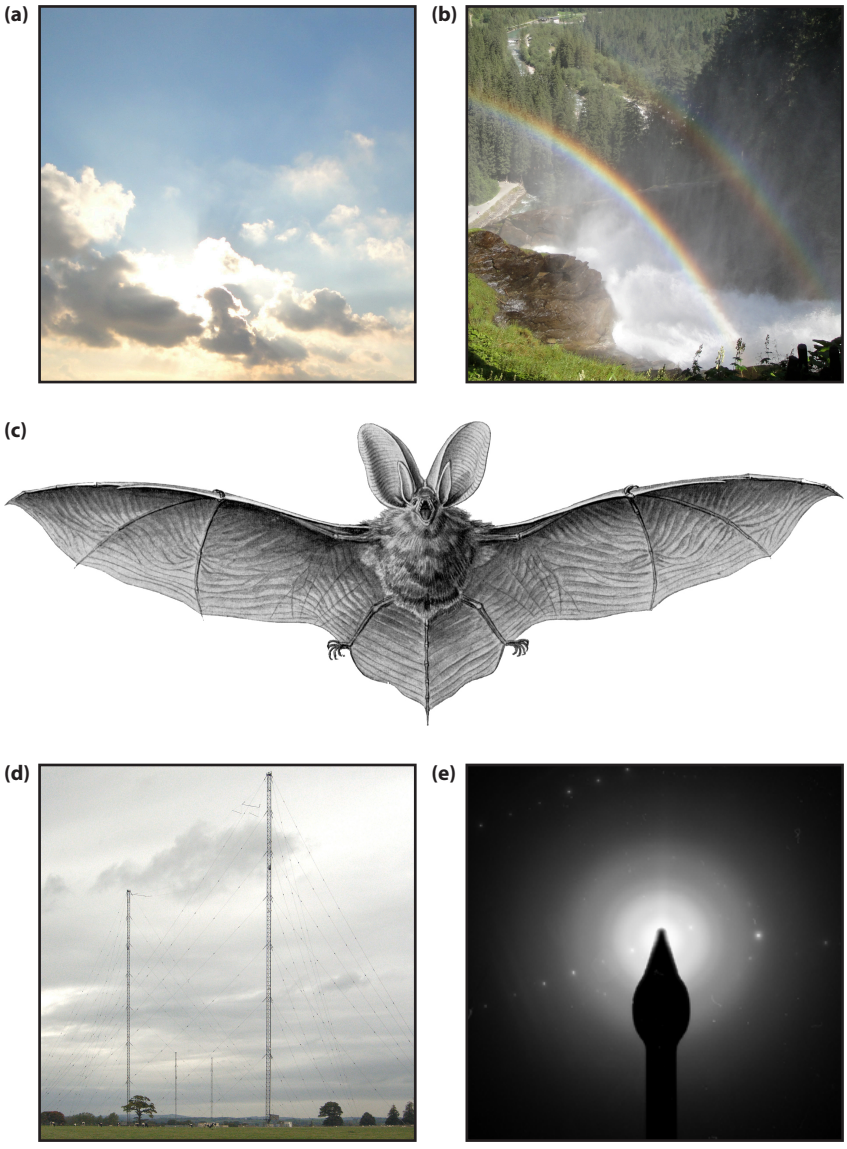

Figure 1.1.: Different appearances of scattering in nature and technology: (a) Multiple scattering of sunlight in a cloud and Rayleigh scattering in the blue sky. (b) First and second order rainbows due to refraction of sunlight at the spray of a waterfall. (c) Bats orientate with echolocation [4]. (d) The Droitwich Transmitting Station for longwave and mediumwave transmission in Droitwich, UK [5]. (e) An interference pattern of electrons scattered at amorphous silicon-carbide with crystalline silicon nanoparticles [6].

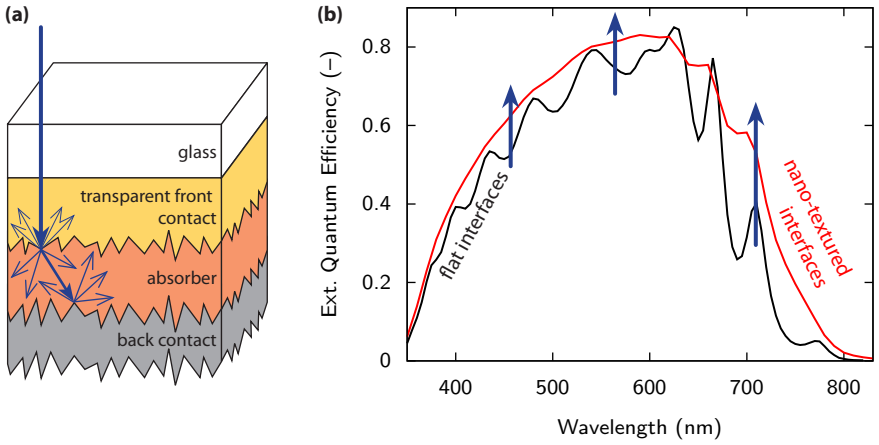

Figure 1.2.: (a) Illustrating light scattering inside a thin-film silicon solar cell (TFSSC). (b) The effect of nano-textured interfaces on the external quantum efficiency of a TFSSC.

Besides these occurrences of scattering in nature – we only named a few – scattering is widely applied in various branches of technology: Radar applications emit radio-waves and analyse the signal that is scattered back from objects. Concert halls are designed such that the sound waves, which are scattered from the walls back into the hall, do not disturb the listener but enhance his listening pleasure. In the early days of radio broadcasting long-wave radio signals were broadcast around the night-side of the globe by using the effect that they are scattered back from the ionosphere such that they stay within the lower layers of the atmosphere as in a waveguide. Geologists investigate the structure of the Earth's crust through studying how waves are scattered at boundaries between different materials or phases. Materials scientists use all kinds of particles, *e.g.* light, x-rays, electrons, positrons and neutrons, in scattering experiments to study the microstructure of matter [7]. Figure 1.1 illustrates several appearances of scattering in nature and technology.

Scattering also is used in thin-film silicon solar cells (TFSSC). These cells with an absorber thickness of only several hundreds of nanometers, contain nano-textured interfaces [8]. These interfaces scatter the incoming light and thus increase the average optical path length of the light traversing the absorber, as illustrated in Fig. 1.2 (a). Therefore the absorption in the absorber layer is increased and more of the sunlight can be converted into electricity.

Figure 1.2 (b) shows the measured *external quantum efficiency*[†] (EQE) of two TFSSCs: one with flat interfaces and one with nano-textured interfaces. The EQE of the flat cell shows consecutive maxima and minima. These so-called *interference*

[†]Roughly speaking, the external quantum efficiency is a measure of how efficiently light of a certain wavelength can be converted into electric energy. A more precise definition is given in Section 2.3.

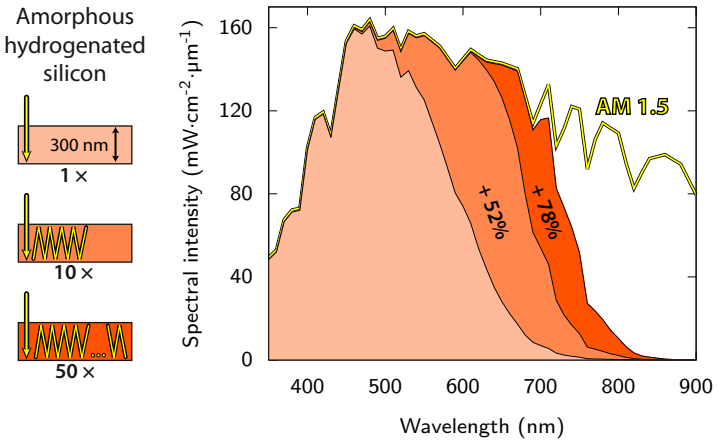

Figure 1.3.: The effect the optical path length in an 300 nm thick a-Si:H slab on the absorption of sunlight [10].

fringes are due to the interaction of two or more beams of light with each other. The EQE of the nano-textured cell shows none of these fringes. The nano-textured interfaces thus reduce or destroy the ability of beams of light to interfere with each other, the so-called *coherence*. The EQE of the nano-textured cell is higher than that of the flat cell. This is mainly due to the prolonged average path length of the light. Further, the nano-texture also has an antireflective effect, increasing the amount of light that initially enters the absorber.

By combining geometrical ray optics with statistical mechanics, Yablonovitch calculated the theoretical potential of using nano-textures in solar cells [9]. He showed that the absorption in a slab with nano-textured surfaces, which is placed in a piece of space filled with blackbody radiation and confined with a white reflector on one side, is increased up to a factor of $4n^2$, where n is the refractive index of the material. Figure 1.3 shows the results of a recent study by Zeman *et al.* [10]: They calculated that increasing the optical path length in a 300 nm thick slab of amorphous hydrogenated silicon (a-Si:H) by a factor 10 increases the absorption of sunlight by 52%. Increasing the optical path length by a factor 50 leads to an increase in absorption of 78%.

The results of Yablonovitch and Zeman *et al.* demonstrate the importance of nano-textures for the performance of thin-film silicon solar cells. Various nano-textured morphologies and materials that carry these nano-textures have been investigated in the last decades.[‡] It is a very important question, how these nano-textures must look like to maximise the absorption in the absorber layer.

Performing such an optimisation experimentally is a very cumbersome task. Further, the freedom of designing nano-textures is restricted by physical con-

[‡]We discuss several materials and morphologies in Subsections 2.5.1 and 3.2.3.

straints. Modelling is an elegant method to study how changes of the nano-textures affect the performance of thin-film silicon solar cells. Moreover they can be used to find optimised nano-textures.

In this thesis we investigate how scattering at nano-textured interfaces can be treated theoretically. Due to the quasi-random character of the nano-textured surfaces the mathematical treatment of the scattering problem is highly non-trivial. We, however, can show that the *scalar scattering theory* is already sufficient to approximate the scattering properties of such a surface. In the scalar scattering theory the light is not treated as an electromagnetic field, but approximated as a scalar field, *i.e.* the vector character of light is neglected. To formulate a model based on scalar scattering theory we revisit important work that was done in this field in the late nineteenth and early twentieth century, mainly by Fraunhofer, Fresnel, Kirchhoff, and Born. After the model is developed and thoroughly tested for various cases, we use it for two different applications. First we combine it with the `ASA` software that can perform opto-electric simulations of complete solar cells. This combination allows to study the effect of the nano-textures on the performance of TFSSC. Secondly, we use the scattering model together with `ASA` to investigate which factors determine whether one nano-texture scatters light more optimally than another.

In detail, this thesis is structured as follows: Before we start with the actual discussion of our topic, we give a brief overview on the photovoltaic effect, which is the physical basis for the operation of solar cells, in Chapter 2. In that chapter we also discuss the most important solar cell technologies that are available nowadays. In Chapter 3 we begin with the actual treatment of our topic by defining two far field scattering parameters and discussing how they can be measured. We also discuss how to measure the morphology of the nano-textures.

In Chapter 4 we lay the foundations of the scalar scattering theory. We then discuss how this theory was used by the thin-film silicon community in the last decade. Chapter 5 is the central chapter of this thesis. There we introduce a full scattering model that is able to calculate the scattering parameters for both transmission and reflection. We also evaluate the model for many different cases. In Chapter 6 we discuss how the model can be extended to obliqe incidence.

In the last two chapters we discuss two different applications of the scattering model: In Chapter 7 we combine our scattering model with the `ASA` device simulator. This combination allows us to predict the effect of nano-textures on the external parameters of the solar cells. Finally, in Chapter 8, we use the scattering model together with `ASA` to investigate how nano-textures can be optimised.

The sun also ariseth, and the sun goeth down, and hasteth to his place where he arose.

Ecclesiastes

2 The photovoltaic effect and solar cells

2.1. Introduction

According to Green, three generations of photovoltaics can be distinguished [11]. The first generation consists of wafer-based silicon solar cells. All the different types of thin-film solar cells form the second generation. The term "third generation" is used for solar cells that utilize novel concepts. However, also these novel concepts are to be incorporated in cells of the first or second generation. Figure 2.1 illustrates the (expected) price-efficiency performance-ratio of the three generations: First generation solar-cells have an efficiency around 20% or a little below. They were very expensive in the past but have become much cheaper recently. The second generation has lower efficiencies and is finally expected to be cheaper than the first generation. The third generation is expected to combine both high efficiency and low price. In the figure also two limits are illustrated: The *single bandgap limit* lies in between approximately 31 and 41%, depending on the semiconductor material [12]. The *thermodynamic limit* lies in between 67% for non-concentrated sunlight and 86% for fully concentrated sunlight [13]. The two limits are explained in more detail further below.

This chapter is organised as follows: After explaining the photovoltaic effect in Section 2.2 and introducing the most important solar cell characteristics in Section 2.3, we briefly discuss the three generations of solar cells in Sections 2.4–2.6.

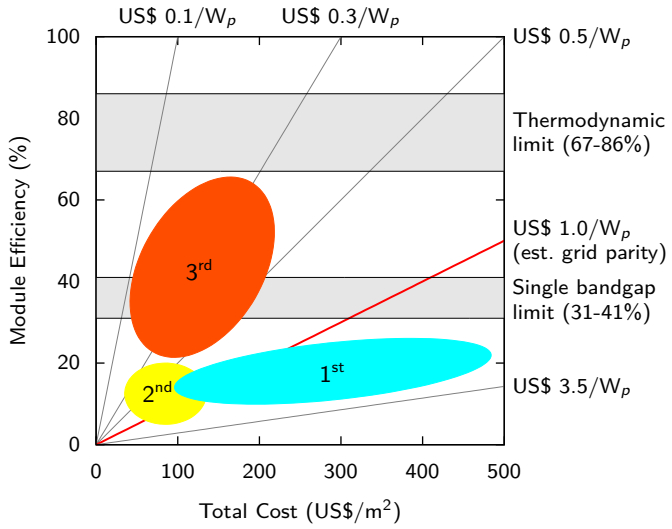

Figure 2.1.: Illustration of the (expected) total costs and module efficiencies of the three generations of photovoltaics. (Based on a figure from Conibeer [14].)

2.2. The photovoltaic effect

The working principle of solar cells is based on the *photovoltaic effect*, *i.e.* the generation of a potential difference at the junction of two different materials in response to electromagnetic radiation. The photovoltaic effect is closely related to the photoelectric effect, where electrons are emitted from a material that has absorbed light with a frequency above a material-dependent threshold frequency. In 1905, Albert Einstein understood that this effect can be explained by assuming that the light consists of well defined energy quanta, called photons. The energy of such a photon is given by $h\nu$, where h is Planck's constant and ν is the frequency of the light. For his explanation of the photoelectric effect Einstein received the Nobel Prize in Physics in 1921 [15]. The photovoltaic effect can be divided into three basic processes:

1. Generation of charge carriers due to the absorption of photons in the materials that form a junction.

Absorption of a photon in a material means that its energy is used to excite an electron from an initial energy level E_i to a higher energy level E_f. Photons can only be absorbed if electron energy levels E_i and E_f are present so that their difference equals to the photon energy, $h\nu = E_f - E_i$. The absorption of a photon in an ideal semiconductor is illustrated in Fig. 2.2. In an ideal semiconductor electrons can populate energy levels below the so-called *valence band* edge, E_V,

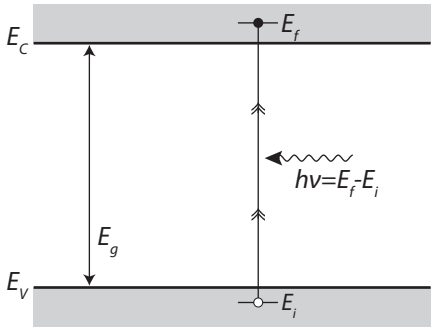

Figure 2.2.: Illustrating the absorption of a photon in a semiconductor with bandgap E_g. The photon with energy hv excites an electron from E_i to E_f. At E_i a hole is created.

and above the so called *conduction band* edge, E_C. Between those two bands no allowed energy states exist, which could be populated by electrons. Hence, this energy difference is called the *bandgap*, $E_g = E_C - E_V$. If a photon with an energy smaller than E_g reaches an ideal semiconductor, it will not be absorbed but will traverse the material without interaction.

In a real semiconductor, the valence and conduction bands are not flat, but vary depending on the so-called *k*-vector that describes the crystal momentum of the semiconductor. If the maximum of the valence band and the minimum of the conduction band occur at the same *k*-vector, an electron can be excited from the valence to the conduction band without a change in the crystal momentum. Such a semiconductor is called a *direct bandgap* material. If the electron cannot be excited without changing the crystal momentum, we speak of an *indirect bandgap* material. The absorption coefficient in an direct bandgap material is much higher than in an indirect bandgap material, thus the absorber can be much thinner [16].

If an electron is excited from E_i to E_f, a void is created at E_i. This void behaves like a particle with a positive elementary charge and is called a *hole*. The absorption of a photon therefore leads to the creation of an electron-hole pair. The *radiative energy* of the photon is *converted* to the *chemical energy* of the electron-hole pair. The maximal conversion efficiency from radiative energy to chemical energy is limited by thermodynamics. This *thermodynamic limit* lies in between 67% for non-concentrated sunlight and 86% for fully concentrated sunlight [13].

2. Subsequent separation of the photo-generated charge carriers in the junction.

Usually, the electron-hole pair will recombine, *i.e.* the electron will fall back to the initial energy level E_i. The energy will then be released either as photon (*radiative recombination*) or transferred to other electrons or holes or lattice vibrations (*non-radiative recombination*). If one wants to use the energy stored in the electron-hole

pair for performing work in an external circuit, semipermeable membranes must be present on both sides of the absorber, such that electrons only can flow out through one membrane and holes only can flow out through the other membrane [13]. In most solar cells, these membranes are formed by *n*- and *p*-type materials.

A solar cell has to be designed such that the electrons and holes can reach the membranes before they recombine, *i.e.* the time it requires the charge carriers to reach the membranes must be shorter than their lifetime. This requirement limits the thickness of the absorber.

3. Collection of the photo-generated charge carriers at the terminals of the junction.

Finally, the charge carriers are extracted from the solar cells with electrical contacts so that they can perform work in an external circuit. The *chemical energy* of the electron-hole pairs is finally converted to *electric energy*.

Loss mechanisms

The two most important *loss mechanisms* in single bandgap solar cells are the inability to convert photons with energies below the bandgap to electricity and thermalisation of photon energies exceeding the bandgap. These two mechanisms alone amount to the loss of about half the incident solar energy in the conversion process [14]. Thus, the maximal energy conversion efficiency of a single-junction solar cell is considerably below the thermodynamic limit. This *single bandgap limit* was first calculated by Shockley and Queisser in 1961 [12].

2.3. Solar cell characteristics

2.3.1. The current density – voltage characteristics

The external parameters of a solar cell can be extracted by illuminating the solar cell under standard test conditions* and determining the *J*-*V* characteristics, where J is the current density and V is the voltage.

A typical example of an illuminated *J*-*V* curve is shown in Fig. 2.3 (a). In the figure, the short-circuit current density J_{sc}, the open-circuit voltage V_{oc}, the current density at the maximum power point J_{MPP} and the voltage V_{MPP} at the maximum power point are indicated. The maximal power density p_{max} is indicated by the shaded rectangle. The fill factor FF of the solar cell is given by the ratio

$$\mathrm{FF} = \frac{p_{\mathrm{max}}}{J_{\mathrm{sc}} V_{\mathrm{oc}}} \tag{2.1}$$

*In the standard test conditions the solar cell is kept at 25°C and illuminated with the AM1.5 (air mass 1.5) spectrum, which is normalised to a total irradiation of 1000 Wm^{-2} and given in ASTM G 173-03 [17].

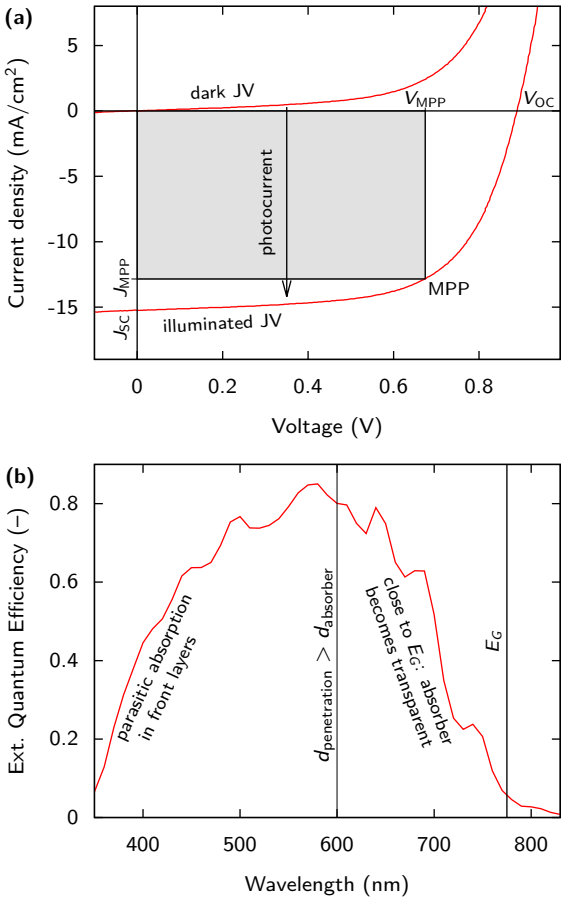

Figure 2.3.: (a) Typical *J-V* characteristics of a solar cell in dark and under illumination. Indicated are the short circuit current density J_{sc}, the open circuit voltage V_{oc}, the maximal power point MPP and the current density J_{MPP} and voltage V_{MPP} at the maximum power point. (b) The external quantum efficiency and the main optical loss mechanisms. Below approximately 600 nm the penetration depth is shorter than the absorber thickness. The fringes are due to interference in in TCO layer. Above 600 nm, where the pentration depth is longer than the absorber thickness, the interference fringes, which have a shorter distance between the maxima, are mainly due to interfence in the absorber.

and should be as high as possible; for commercial solar cells it should be higher than 0.7. The energy conversion efficiency is given by $\eta = p_{\max}/p_i$, where p_i is the power density of the incident radiation. Under AM 1.5 illumination this is 1000 Wm^{-2}.

In Fig. 2.3 (a) also a dark *J-V* curve is indicated. The difference between the dark and the illuminated *J-V* is the photocurrent.

2.3.2. External quantum efficiency

The external quantum efficiency $\mathrm{EQE}(\lambda_0)$ is the fraction of photons incident on the solar cell that create electron-hole pairs in the absorber, which are successfully collected. It is wavelength dependent and is usually measured by illuminating the solar cell with monochromatic light of wavelength λ_0 and measuring the photocurrent I_{ph} through the solar cell. The external quantum efficiency is then determined as

$$\mathrm{EQE}(\lambda_0) = \frac{I_{\mathrm{ph}}(\lambda_0)}{e\,\Phi_{\mathrm{ph}}(\lambda_0)}, \tag{2.2}$$

where e is the elementary charge and Φ_{ph} is the photon flux incident on the solar cell. Since I_{ph} is dependent on the bias voltage, the bias voltage must be fixed. The photon flux is usually determined by measuring the EQE of a calibrated photodiode under the same light source.

Figure 2.3 (b) illustrates a typical EQE for a hydrogenated amorphous silicon (a-Si:H) thin-film solar cell. We can identify the major optical loss mechanisms for such a solar cell: For short wavelengths only a small fraction of the light is converted into electron-hole pairs. Most photons are already absorbed in the layers that the light traverses prior to the absorber layer. For an a-Si:H cell these are the TCO and p-layers. For long wavelengths, the penetration depth[†] of the light exceeds the optical thickness of the absorber. Then the absorber itself becomes transparent so that most of the light leaves the solar cell before it can be absorbed. Light trapping techniques aim to reduce these losses, mainly in the red. Thermalisation losses are not visible in EQE. For example, the EQE depicted in Fig. 2.3 (b) is about 0.6 at both 440 and 670 nm. However, the fraction of the photon energy converted into electric energy is considerably lower at 440 nm.

When a bias voltage of 0 V is applied, the measured photocurrent density equals the short circuit current density. When applying a sufficiently large reversed bias voltage, it can be assured that nearly all photo-generated charge carriers in the intrinsic layer are collected. Thus, this measurement can be used to study the optical effectiveness of the design, *i.e.* light trapping and light absorption in inactive layers, such as the TCO layer, doped layers and the back reflector.

[†] According to Lambert-Beer's law, the intensity of light in an absorbing layer decays exponentially, $\mathcal{I}(z) \propto \exp(-\alpha z)$, where α is the absorption coefficient. The *penetration depth* is then defined as $d_{\mathrm{pen}}(\lambda_0) = 1/\alpha(\lambda_0)$. The absorption coefficient α is related to the imaginary part $\tilde{k}$ of the complex refractive index via $\alpha(\lambda_0) = 4\pi\tilde{k}/\lambda_0$.

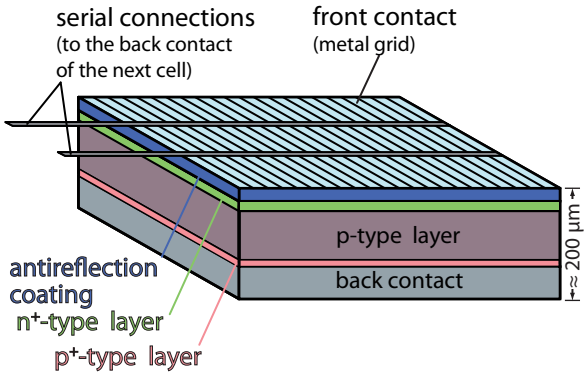

Figure 2.4.: Scheme of a modern crystalline silicon cell.

2.4. First generation: Wafer-based solar cells

Wafer-based solar cells made from crystalline silicon (c-Si) form the highest developed PV technology. With a market share of around 85% in 2010 they form by far the most important player in the solar cell market [18]. Silicon is the second most abundant material in the Earth's crust, with a mass percentage of 27. The most abundant material in the crust is oxygen with a mass percentage of 46.

The first c-Si solar cell was made by Chapin *et al.* in 1954 and showed an energy conversion efficiency of 6% [19]. The theoretical limit for a single junction solar cell made of a material with a bandgap of 1.1 eV was calculated by Shockley and Queisser in 1961 to be 33.7% [12]. The bandgap of silicon is 1.12 eV, the theoretical limit of a c-Si solar cell is therefore very close to 33.7%.

Figure 2.4 illustrates the design of a modern wafer based silicon solar cell. It consists of p-type mono-crystalline or poly-crystalline silicon wafers. The top of the wafer then is highly doped so that it becomes n^+-type. Similarly, the bottom of the wafer is made p^+-type. The central p-type region is the absorber, the n^+- and the p^+ region form the membranes that are needed to separate the electrons from the holes. The silicon wafers usually are between 200 µm and 300 µm thick. Their thickness is on the one hand influenced by the production process of the wafers. On the other hand, c-Si is an indirect semiconductor, *i.e.* a sufficient absorber thickness of at least several tens of micrometers is required to ensure the absorption of a sufficiently large fraction of the incident light. However, the industry is very interested in making the wafers thinner in order to reduce material consumption and therefore cost. State-of the art crystalline silicon solar cells also have an anti-reflective coating on top. They usually have efficiencies in between 15 and 20%, the current record single-junction mono-crystalline cell on laboratory scale has an efficiency of 25.0% [20].

2.5. Second generation: Thin-film solar cells

Solar cells based on thin films are called second-generation solar cells. The thin films are much thinner than the wafers that form the base for first generation PV. According to Chopra *et al.* [21], 'a *thin film* is a film that is created ab initio by the random nucleation process of individually condensing/reacting atomic/ionic/molecular species on a substrate. The structural, chemical, metallurgical and physical properties of such a material are strongly dependent on a large number of deposition parameters and may also be thickness dependent.'

Thin-film solar cells were expected to become cheaper than first generation solar cells. However, due to the current price decline in wafer based solar cells thin-film solar cells have not become interesting from an economic point of view yet.‡ In general these cells have a lower efficiency than wafer-based cells. GaAs is an exception to this rule of thumb [20]. In contrast to wafer based silicon solar cells that are self-supporting, thin-film solar cells require a carrier that gives them mechanical stability. Usual carrier materials are glass, stainless steel or polymer foils. It is thus possible to produce flexible thin-film solar cells.

In thin-film solar cells the active semiconductor layers are sandwiched between a transparent conductive oxide (TCO) layer and the electric back contact. Often a back reflector is introduced at the back of the cell in order to minimise transmissive solar cell losses.

Thin-film solar cells can be made of many different materials. After discussing TCOs we will introduce the most important types. The reader interested in more detailed information on thin-film solar cells may refer to the book by Poortmans and Arkhipov [23].

2.5.1. Transparent conductive oxides

Due to the paramount importance of the TCO layer for the solar cell performance we briefly discuss its main properties. The TCO layer acts as electric front contact of the solar cell. Furthermore, it guides the incident light to the active layers. It therefore should be both highly conductive and highly transparent in the active wavelength range. The first resistance measurements on thin-films of what we nowadays call TCOs were published by Bädeker in 1907 [24].

Figure 2.5 shows the transmission, reflection and absorption spectra of a flat ZnO:Al layer. Following Kluth, we divide this spectrum into three parts [25]: For short wavelength, the transmission is very low due to the high absorption of light with energies higher than the bandgap. For longer wavelength, with photon-energies below the bandgap, the transmission is very high. We here see interference fringes that can be used to determine the film thickness. After a broad highly transmissive wavelength band, the absorption increases again. This absorption is called free carrier absorption an can be explained with the Drude

‡According to the *PHOTON module price index*, the price for wafer-based modules has decreased around 40% within one year as of 25 May 2012 [22].

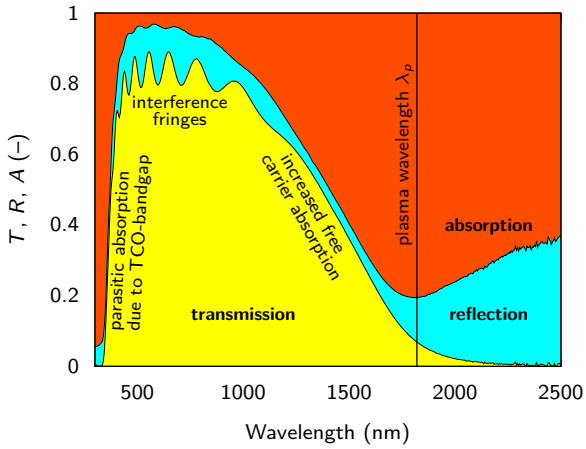

Figure 2.5.: Transmission, reflection and absorption of a ZnO:Al layer (d = 880 nm).

theory of metals that was developed in 1900 [26, 27]. In this model, the frequency-dependent electric permittivity is given by

$$\epsilon(\omega) = \left[n(\omega) - i\tilde{k}(\omega)\right]^2 = 1 + \chi(\omega) = 1 - \frac{\omega_p^2}{\omega^2 + i\frac{\omega}{t}}, \tag{2.3}$$

where $\chi(\omega)$ is the dielectric susceptibility, t is the relaxation time,[§] $n - i\tilde{k}$ is the complex refractive index and ω_p denotes the *plasma frequency* that is given by

$$\omega_p = \frac{\mathfrak{N}e^2}{\epsilon_0 m_e^{*2}}. \tag{2.4}$$

Here, $\mathfrak{N}$ is the density of free charge carriers, e is the elementary charge, ϵ_0 is the permittivity of vacuum and m_e^* is the effective electron mass in the TCO layer.

The real and imaginary part of the susceptibility are given by

$$(\Re\chi)(\omega) = -\omega_p^2 \frac{t^2}{\omega^2 t^2 + 1}, \tag{2.5a}$$

$$(\Im\chi)(\omega) = \omega_p^2 \frac{t/\omega}{\omega^2 t^2 + 1}. \tag{2.5b}$$

If $\omega t \gg 1$, ϵ can be simplified to

$$\epsilon(\omega) \approx 1 - \frac{\omega_p^2}{\omega^2}, \tag{2.6}$$

[§]The relaxation time denotes the average time between two collisions, *i.e.* two abrupt changes of velocity, of the electrons.

while the imaginary part is negligible.

If this approximation is valid around ω_p, the material is transparent for $\omega > \omega_p$ ($\epsilon > 0$). For $\omega < \omega_p$, ϵ becomes negative, *i.e.* the refractive index is purely imaginary and the material therefore has a reflectivity of 1. In this case, the material changes dramatically from transparent to reflective, as ω_p is crossed.

If the approximation $\omega t \gg 1$ is not valid, $\Im\chi$ cannot be neglected. The imaginary part will increase with decreasing frequency, *i.e.* with increasing wavelengths the absorption increases. For wavelengths longer than the plasma wavelength the material becomes more reflective, what we also see in Fig. 2.5. For application in solar cells, the TCO should be highly transparent in the active region of the absorber. Therefore the plasma-wavelength should at least be longer than the bandgap wavelength of the absorber. On the other hand the plasma frequency is proportional to the free carrier density $\mathfrak{N}$. A longer plasma wavelength therefore corresponds to a lower $\mathfrak{N}$. Finding an optimum between high transparency and high carrier densities is an important issue in designing TCOs for solar cell applications.

Even though the Drude model gives a good approximation of the free carrier related phenomena in TCOs, this model often is too simple. Therefore several authors used extended Drude models with more parameters [28–30].

Of all TCO materials currently available, the trade off between transparency and conductivity is best for indium tin oxide [31]. However, indium is a rare earth element with a very low abundance of 0.05 ppm in the Earth's crust, similar to the abundance of silver (0.07 ppm) and mercury (0.04 ppm) [32], which makes it less preferable for cheap large-scale PV applications. Therefore other TCO materials are thoroughly investigated and used in industry. Amongst them are aluminium doped zinc oxide, boron doped zinc oxide and fluorine doped tin oxide. The abundances of the used elements are: aluminium: 7.96%, zinc: 65 ppm, boron: 11 ppm, fluorine: 525 ppm, and tin: 2.3 ppm [32]. We discuss these TCOs in more detail in Section 3.2.

2.5.2. Thin-film silicon solar cells

Beside the crystalline phase that is utilised in first generation PV, also two other phases of silicon are used for solar cells: Amorphous silicon (a-Si) and nanocrystalline silicon (nc-Si). Amorphous silicon as such is of little use in photovoltaics because of the extremely high defect density ($> 10^{19}$ cm^{-3}) [23]. This results in fast recombination of photo-excited excess carriers. Alloying the a-Si with hydrogen leads to passivation of most defects, resulting in a defect density around 10^{16} cm^{-3} [33]. Hydrogenated amorphous silicon (a-Si:H) thus is usable as PV material. The bandgap of a-Si:H is about 1.7 eV, therefore only light with a wavelength shorter than approximately 730 nm can excite electron-hole pairs. In contrast to c-Si, a-Si:H has an direct bandgap. Thus already a thin film is sufficient to absorb most of the light with energies above the bandgap.

The first successful a-Si:H solar cell with an efficiency of 2.4% was reported by

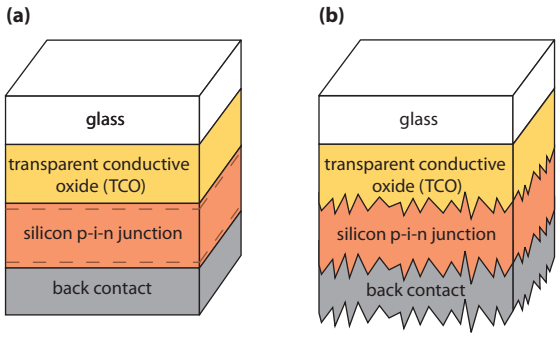

Figure 2.6.: Illustrating thin-film silicon solar cells with flat interfaces (a) and with nano-textured interfaces (b) in p-i-n configuration. (Layer thicknesses not in scale.)

Carlson and Wronski in 1976 [34]. Already one year later, Staebler and Wronski discovered that prolonged illumination leads to the creation of metastable defects in a-Si:H, reducing the initial efficiency of a-Si:H solar cells by typically 10-20% [35]. Despite the comparably low efficiency of thin-film silicon solar cells, much effort is invested to improve their performance, because of the potential cost reduction due to the energy and material saving production process [36].

Due to the short carrier lifetime and the low carrier mobility in a-Si:H, thin-film a-Si:H solar cells require a drift zone between the doped layers. Therefore, these cells contain an intrinsic i-layer that is sandwiched between thin n and p-layers. Two ways of depositing thin-film silicon cells are possible: So called "p-i-n" cells are deposited onto a *superstrate* with the front TCO first, followed by the p-i-n structure and the back layers. In difference, "n-i-p" cells are be deposited onto a *substrate* with the back layers first, followed by the n-i-p structure, and finally the front TCO. Figure 2.6 (a) illustrates the design of a *superstrate* thin-film *a*-Si:H solar cell on a glass carrier.

To increase the absorption of light in the absorber layer (i-layer), textured interfaces are introduced in state-of-the-art thin-film silicon solar cells, as illustrated in Fig. 2.6 (b). The incident light is scattered at the textured interfaces, leading to a longer photon path length in the absorber.

Nanocrystalline hydrogenated silicon (nc-Si:H) lies in the transition region between amorphous and crystalline silicon [37]. It consists of many small crystals with sizes of several nanometers that are surrounded by an amorphous silicon tissue. Its bandgap of about 1.1 eV is comparable to that of crystalline silicon. It thus can absorb light with wavelengths shorter than about 1100 nm. The Staebler-Wronski effect for nc-Si:H is less severe than for a-Si:H. Due to its lower bandgap, nc-Si:H is a very interesting material for tandem cells that we discuss in Section 2.6. The current record efficiency for both thin-film a-Si:H and nc-Si:H solar cells is 10.1% [20].

2.5.3. Gallium arsenide solar cells

Gallium arsenide (GaAs) is a III-V semiconductor with a bandgap of 1.424 eV [16]. In contrast to silicon, which is highly abundant, the abundance of gallium in the Earth's crust is only about 14 ppm [38]. GaAs therefore is a very expensive material. However, since GaAs is an direct bandgap material, the absorber can be made very thin. Thin-film GaAs solar cells are highly efficient with a current record energy conversion efficiency of 28.8% [20]. Due to their high efficiencies, GaAs cells are used for extraterrestrial applications, *e. g.* satellites. Also crystalline GaAs solar cells can be produced, but they are less efficient than thin-film GaAs cells [20]. Arsenic is highly toxic; it is strongly suggested that GaAs is carcinogenic for humans [39].

Since GaAs cells are high-cost high-efficiency cells, they are very interesting for *concentrated photovoltaic* (CPV) systems [40].[¶] In CPV systems, the light is focused onto a small area that is covered with a solar cell. Due to the concentration, much smaller areas of solar cells are needed, reducing the cost. High concentration photovoltaic systems concentrate sunlight to intensities of 500 suns or higher.

2.5.4. Chalcogenide solar cells

These cells are also called *thin-film polycrystalline (heterojunction) solar cells*. The term heterojunction denotes that the n and p layers consist of different materials.

The p-n junction in *copper indium gallium diselenide* (CIGS) solar cells is formed between a p-doped CIGS absorber layer and an n-doped cadmium sulphide (CdS) window layer [41, 42]. The certified record efficiency is 19.6% [20], however, efficiencies above 20% were reported [41]. CIGS is a I-III-VI_2 semiconductor compound material with the chemical formula $Cu(In_xGa_{1-x})Se_2$, where x varies between 0 and 1. The bandgap varies continuously with x from about 1.0 eV for pure CIS to about 1.7 eV for pure CGS [43]. CIGS contains indium that is, as already stated above, a rare earth material with a very low abundance [32].

Solar cells made from *Cadmium telluride* (CdTe), a II-VI semiconductor, have become very important in recent years, mainly due to the rapid growth of the company First Solar [44]. In these solar cells a p-doped CdTe absorber forms an p-n junction with an n-doped CdS window layer [45]. The record efficiency has been reported to be 17.3% [20]. Tellurium is one of the rarest stable solid elements in the Earth's crust with an abundance of about 1 µg/kg, which is comparable to that of platinum [46]. CdTe was shown to be far less toxic than elementary Cd, but further research is needed for final conclusions [47].

[¶] Of course, CPV systems can be used with any solar cell type. However, they are most interesting with highly efficient solar cells.

2.5.5. Organic solar cells

In organic solar cells, organic materials are used in the active layers. Full organic devices as well as hybrid devices are investigated. In the fully organic bulk donor-acceptor heterojunction concept, a blend of two organic compounds, one with donor and one with acceptor properties, is used as photoactive layer [48]. The current organic record cell has an efficiency of 10.0% [20].

A special type of organic solar cells are *dye solar cells*, also known as *Grätzel cells* [49]. They contain TiO_2 particles of several nanometers diameter that form a porous layer. A monolayer of an organic dye is absorbed on the pore walls of the TiO_2 particles. The space between the particles is filled with an electrolyte that fills all the pores. When lights enters it is absorbed by the dye. The electrolyte then forms a "membrane" for the holes, while the electrons can move into the TiO_2 without difficulty. The record dye cell shows an efficiency of 11.0% [20]. The most efficient cells use liquid electrolytes, which are very unstable [50]. Solid-state or quasi-solid-state electrolytes are stable but lead to low efficiencies [51].

2.6. Third generation photovoltaics

The term *third generation photovoltaics* refers to all novel approaches that try to overcome the Shockley-Queisser single bandgap limit at low cost. However, at the moment only multi-junction solar cells have realised this goal while all other third generation technologies are in an experimental phase.

2.6.1. Multi-junction solar cells

Depending on the author, multi-junction solar cells are seen as part of the second or the third generation. In these cells, several cell materials with different bandgaps are combined in order to maximise the amount of the sun light that can be converted into electricity. To realise this, two or more cells are stacked onto each other. The top cell has the highest bandgap, in order to absorb and convert the short wavelength (blue) light. Light with wavelengths longer than the bandgap-wavelength can traverse the top cell and be absorbed in the cells below with lower bandgaps. The bottom cell has the lowest bandgap to absorb the long wavelength (red and near infrared) light. In order to optimise the performance of multi-junction solar cells with two electrical terminals, matching the currents of all the subcells (current matching) is crucial. Multi-junction cells with more terminals do not have this restriction, but their production is more complicated.

In thin-film silicon tandem cells, an a-Si:H top cell is stacked onto a nc-Si:H bottom cell. In order to achieve current matching, the top cell is much thinner than the bottom cell. The cell can be further optimised by using an intermediate reflector between the top and the bottom cell in order to reflect the blue light back into the top cell while letting the red light pass to the bottom cell. The reported record efficiency of a-Si:H/nc-Si:H tandem cells is 12.3% [20].

Multi-junction cells containing III-V semiconductors are at present the most efficient solar cells. The current world record efficiency is 43.5% for a triple-junction GaInP/GaAs/GaInNAs cell that is used in a concentrated PV-system [20].

2.6.2. Other concepts

We mention the most important other concepts that have been studied:

Hot carriers are investigated to to collect electron-hole pairs of high energy photons before they have a chance to thermalise [14].

In *intermediate-level cells* energy levels are created artificially in the bandgap of the absorber material such that they can absorb low-energy photons in parallel with the normal single junction solar cell operation. The intermediate levels should be realised with impurities or quantum dots [52].

The incident spectrum can be modulated with an additional layer. Two or more low energy photons are *up-converted* to one high energy photon [53] or one high-energy photon is *down-converted* to two or more low energy photons [54]. Hence, a larger fraction of the solar spectrum can be utilised. Only small enhancements in efficiency due to up/down-converters have been reported [36].

Finally, with *multiple carrier excitation* more than one electron-hole pairs is generated from high energy photons. There are indications that multiple carrier excitation can be realised with quantum dots [55].

All these concepts are still in an experimental phase and it is not clear whether they will ever become a large scale PV technology [36].

2.7. Conclusion

Photovoltaics has become an important energy conversion technology in the last years. In this chapter we discussed the photovoltaic effect and the three generations of solar cells. It is now good to revisit Fig. 2.1. Crystalline silicon solar cells (first generation) have efficiencies below 25%. They were considered quite costly in the past but their price has dropped by 40% between May 2011 and May 2012 [22]. Therefore they now combine reasonably high efficiencies at a good price, which explains their current market dominance.

Thin-film solar cells form the second solar cell generation. Their efficiency is below 20%, except for cells based on gallium arsenide. Since they are based on thin films, much less material is needed than for first-generation solar cells. Many of the elements used in these cells, however, have a very low abundance making their applicability for large scale applications questionable. Thin-film silicon solar cells can be produced such that they only contain abundant elements. The name third generation spans many different concepts. The goal is to produce high-efficiency cells at a low cost. However, high efficiencies have only been reached with multi-junction solar cells, which at the moment are still expensive. The high cost of these cells is due to the high number of processing steps.

Misura ciò che è misurabile, e rendi misurabile ciò che non lo è.*

Galileo Galilei

3

Morphology and far-field scattering properties of nano-textured interfaces

3.1. Introduction

A monochromatic parallel beam of light of wavelength λ_0 that is impinging on an *optically flat* interface is transmitted and reflected according to the Fresnel equations. Optically flat means that the typical feature size d of the interface is much smaller than λ_0, $d \ll \lambda_0$.

If the feature size has the same order of magnitude as λ_0, only a fraction of the transmitted (reflected) light will act according to the Fresnel equations. This fraction is called the *specular* transmitted (reflected) light; we abbreviate it with the symbols T_{spec} and R_{spec}, respectively. All other light is deflected by the textured interface, as illustrated in Fig. 3.1. We call this fraction *scattered* or *diffuse* and abbreviate it with T_{dif} and R_{dif}. We call such a surface *nano-textured*. The total transmittance and reflectance are given by

$$T_{\text{tot}}(\lambda_0) = T_{\text{spec}}(\lambda_0) + T_{\text{dif}}(\lambda_0), \tag{3.1a}$$

$$R_{\text{tot}}(\lambda_0) = R_{\text{spec}}(\lambda_0) + R_{\text{dif}}(\lambda_0). \tag{3.1b}$$

In general, T_{tot} and R_{tot} are not equal to T and R of a flat interface.

*Measure what is measurable, and make measurable what is not so.

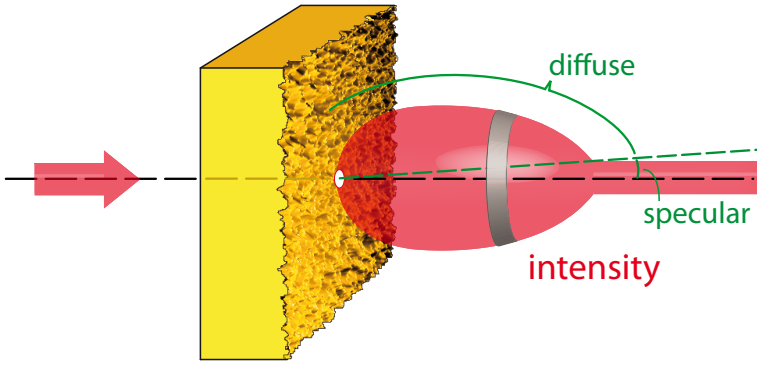

Figure 3.1.: Illustrating scattering of light at a nano-textured interface.

If the surface features are much larger than λ_0, $d \gg \lambda_0$, all light will be deflected and no specular fraction will be left. This *geometrical limit* can be described with geometrical optics; Snell's law and the Fresnel equations are sufficient to describe the propagation of the light after being scattered at such an interface.

From a mathematical point of view the second case, where both specular and scattered fractions are present, is the most interesting one. Nano-textured interfaces that are used in a-Si:H solar cells are in this category. In this thesis we solely will focus on nano-textured surfaces. Patterned interfaces that are used in wafer-based c-Si solar cells can be treated within the geometrical limit.

Scattering of nano-textured surfaces can be investigated in the far field, *i.e.* when $k_0 r \to \infty$, or in the near field, when $k_0 r < 2\pi$. Here, $k_0 = 2\pi/\lambda_0$ denotes the wavenumber and r denotes the distance between the sample and the detector. In recent years, many efforts in near-field scanning optical microscopy (NSOM) have been made that allow to analyse the electromagnetic fields very close to the surface [56, 57]. Investigations of the scattered far field are, however, the standard method to judge scattering by surface-textured layers [58–61]. Usually two parameters are utilised:

First, the haze is a wavelength-dependent parameter that quantifies the amount of light that is scattered away from the specular direction. The haze in reflection H_R and transmission H_T are defined as

$$H_R(\lambda_0) = \frac{R_{\text{dif}}(\lambda_0)}{R_{\text{tot}}(\lambda_0)} \qquad \text{and} \qquad H_T(\lambda_0) = \frac{T_{\text{dif}}(\lambda_0)}{T_{\text{tot}}(\lambda_0)}. \tag{3.2}$$

Secondly, the angular intensity distribution (AID) indicates how strong a structure scatters into different angles. The AID is, up to a constant, defined as the power ΔP_s scattered into a small solid angle $\Delta\Omega_s$ normalised to that solid angle

and the incident power P_i [62],

$$\mathrm{AID}(\lambda_0;\theta_t,\phi_t) = \kappa \frac{\Delta P_s(\lambda_0;\theta_t,\phi_t)}{\Delta\Omega_s P_i}. \tag{3.3}$$

The direction of the light is indicated by the spherical coordinates (θ_t, ϕ_t); the constant κ is dependent on the measurement setup. The AID is related to the bidirectional spectral-transmittance distribution function (BTDF) [63], $f_t(\lambda_0;\theta_i,\phi_i;\theta_t,\phi_t)$,

$$\mathrm{AID}(\lambda_0;\theta_t,\phi_t) = \kappa f_t(\lambda_0;0,0;\theta_t,\phi_t)\cos\theta_t, \tag{3.4}$$

where (θ_i, ϕ_i) indicates the direction of the incident light. For the AID different names are used in literature. Some authors call both the measurement technique and the measurement result "angular resolved scattering" (ARS) [64–67]. Others use the name "angular distribution function" (ADF) [58, 59]. We, however, prefer the name "angular intensity distribution".

The objective of this chapter is to discuss all experimental techniques that are needed to evaluate the scattering models that we discuss in this thesis. Since the scattering models relate the morphology of nano-textured interfaces to the scattering properties, we need techniques to determine the interface morphology and techniques to determine the far-field scattering parameters. In Section 3.2 we discuss atomic force microscopy (AFM) measurements with which we determine the morphology and the statistical parameters of the used nano-textured samples. In that section we also introduce samples with different nano-textures that we will use throughout the thesis. In Section 3.3 we discuss the haze measurements. In Section 3.4 we describe how to measure the AID. Since we use a novel technique for the AID measurements, we need to validate them, which is done in Section 3.5. Finally, in Section 3.6 we discuss the determination of the AID at a TCO-Si interface.

The results presented in Sections 3.4 and 3.5 can also be found in Ref. [68, 69]; the results in Section 3.6 are discussed in Refs. [70, 71].

3.2. Morphology and optical properties

3.2.1. Atomic force microscopy (AFM)

AFM is a powerful technique with which the morphology of nano-textured surfaces can be determined [72]. During an AFM measurement a tiny probe with a tip radius of several nanometers is brought so close to the surface that atomic forces between the surface and the probe become important. Due to these forces the surface morphology can be determined. Under *amplitude modulation* the amplitude and the phase of the tip will change during the scan depending on the Van der Waals forces, *i.e.* the distance between the tip and the sample. Several modes can be used. We used the so called *tapping mode* in which the probe is

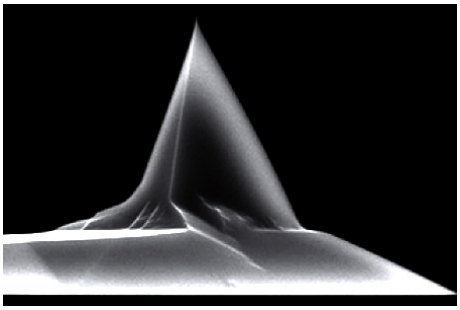

Figure 3.2.: The NSG 10 gold-coated single-crystal silicon tip used throughout this project [73].

oscillating at its resonance frequency. From the obtained amplitude and phase pictures the height profile of the investigated sample can be obtained.

The height profile is not the *real* height profile of the sample but a convolution of the height profile and the shape of the tip. A blunt tip therefore will lead to a blurry picture. If the tip is broken and therefore consists of two or more peaks, the features on the scan will be doubled. Further, scanning the surface too fast will lead to contact loss between the tip and the sample at steep features. Therefore the AFM measurements have to be performed very carefully.

We performed the AFM measurements with instruments from NT-MDT and Veeco (only in Chapter 7). Figure 3.2 shows a picture of the tip of the AFM probes we used in our project. This so-called NSG 10 tip is made from antimony doped single-crystal silicon and coated with gold. Its tip radius is typically 6 nm, with a guaranteed radius of maximal 10 nm [73].

3.2.2. Statistical parameters

The AFM scan reveals three dimensional data of the nano-textured surface via the height function $z(x, y)$, which can be used to extract statistical properties of the samples. To compare the different samples we use two different parameters, the *root-mean-squared (rms) roughness* σ_r and the *correlation length* ℓ_c.

The rms roughness in principle is the standard deviation of the height profile. It is defined as

$$\sigma_r = \sqrt{\frac{1}{N-1}\sum_{i=1}^{N}(z_i - \bar{z})^2}, \tag{3.5}$$

where N is the number of data points, z_i is the height of the i^{th} datapoint and $\bar{z}$ is the average height. It becomes clear from the definition that σ_r is insensitive to the lateral feature sizes. Samples with very small or large lateral features both can have the same rms roughness.

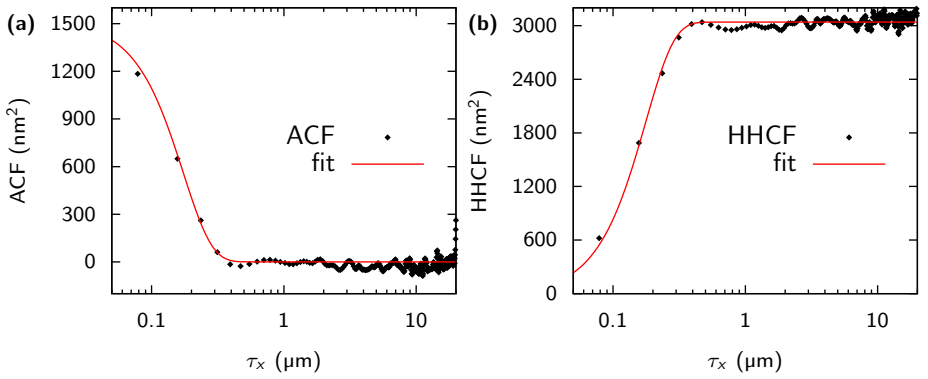

Figure 3.3.: The ACF and HHCF and fitted Gaussian functions for SnO_2:F.

The correlation length gives an indication of the lateral feature sizes. Its derivation is less straightforward then that of σ_r: it has to be extracted from autocorrelation function (ACF) and/or the height-height correlation function (HHCF) [74]. For a discrete set of data, the two-dimensional ACF is given by

$$\mathrm{ACF}(\tau_x, \tau_y) = \frac{1}{(N-n)(M-m)} \sum_{l=1}^{N-n} \sum_{k=1}^{M-m} z(k\delta + \tau_x,\, l\delta + \tau_y)\, z(k\delta,\, l\delta), \qquad (3.6)$$

where δ is the distance between two data points, $m = \tau_x/\delta$ and $n = \tau_y/\delta$. For AFM scans usually the one-dimensional ACF along the fast scanning axis (x) is used:

$$\mathrm{ACF}_x(\tau_x) = \mathrm{ACF}(\tau_x, 0) = \frac{1}{N(M-m)} \sum_{l=1}^{N} \sum_{k=1}^{M-m} z(k\delta + \tau_x,\, l\delta)\, z(k\delta,\, l\delta). \qquad (3.7)$$

The one-dimensional HHCF is given by

$$\mathrm{HHCF}_x(\tau_x) = \frac{1}{N(M-m)} \sum_{l=1}^{N} \sum_{k=1}^{M-m} \left[z(k\delta + \tau_x,\, l\delta) - z(k\delta, l\delta)\right]^2. \qquad (3.8)$$

To determine ℓ_c, Gaussian functions can be fitted to the ACF and the HHCF. They are given by

$$\mathrm{ACF}_x^{\mathrm{fit}}(\tau_x) = \sigma_r^2 \exp\left(-\frac{\tau_x^2}{\ell_c^2}\right), \qquad (3.9)$$

$$\mathrm{HHCF}_x^{\mathrm{fit}}(\tau_x) = 2\sigma_r^2 \left[1 - \exp\left(-\frac{\tau_x^2}{\ell_c^2}\right)\right], \qquad (3.10)$$

respectively. The correlation length then is the length at which the (fitted) ACF has decayed to $1/e$ of its highest value. Instead of applying Eq. (3.5) directly,

the rms roughness also can be obtained by fitting Gaussian functions to the ACF and/or the HHCF.

Figure 3.3 shows the ACF and the HHCF and fitted Gaussian functions for a SnO_2:F sample. Its statistical parameters are given in the next section. Instead of fitting to Gaussian functions, some authors also use exponential functions for fitting. For our samples Gaussians lead to better fits.

3.2.3. The morphology of selected samples

Figure 3.4 shows the morphology, rms roughness and correlation length of the nano-textured TCO samples that we used in this project. In the project discussed in this thesis we used nano-textures on three different TCO materials. Fluorine-doped AP-CVD tin oxide (SnO_2:F) of Asahi U-type [75] and boron-doped LP-CVD zinc-oxide (ZnO:B) of so-called 'B-type' from PV-LAB of the École polytechnique fédérale de Lausanne (EPFL), Switzerland [60], obtain their nano-structure already during the deposition process. The nano-structure is due to the crystal growth of the TCO layers and has a *pyramid-like* shape.

In contrast, RF-sputtered, aluminium-doped zinc oxide (ZnO:Al) is flat after deposition ($\sigma_r \approx 3$ nm, depending on the deposition condition up to about 20 nm). To obtain a nano-texture, ZnO:Al is etched in a 0.5% HCl solution [61, 76]. This etching process leads to *crater-like* features. The lateral size of these craters is influenced by the grain size of the zinc oxide crystals. Fig. 3.4 (c) and (d) shows etched ZnO:Al with broad craters. Fig. 3.4 (e) and (f) shows etched ZnO:Al with narrow craters.

To determine σ_r and ℓ_c, we used AFM scans of 256×256 points over an area of 20×20 µm^2. Because of the small lateral feature size of SnO_2:F we also determined the statistical parameters for 5×5 µm^2 scans. We obtained $\sigma_r = 37$ nm and $\ell_c = 160$ nm. These values are very close to those presented in Fig. 3.4 (a).

3.2.4. Optical constants

For SnO_2:F and ZnO:Al we determined the $n, \tilde{k}$ data by the method described by Sap *et al*. [30]. The $n, \tilde{k}$ data of ZnO:B was provided by the PV-LAB of the EPFL [77]. The real parts n of the refractive indices are shown in Fig. 3.5

3.3. The haze

3.3.1. Integrating sphere

To determine the haze in transmission (reflection), we need to measure T_{tot} and T_{dif} (R_{tot} and R_{dif}), as we have seen in Eq. (3.2). For scattering samples, they are usually measured with an integrating sphere (IS) as illustrated in Fig. 3.6. We used an integrating sphere from PerkinElmer®of 150 mm diameter. Due to

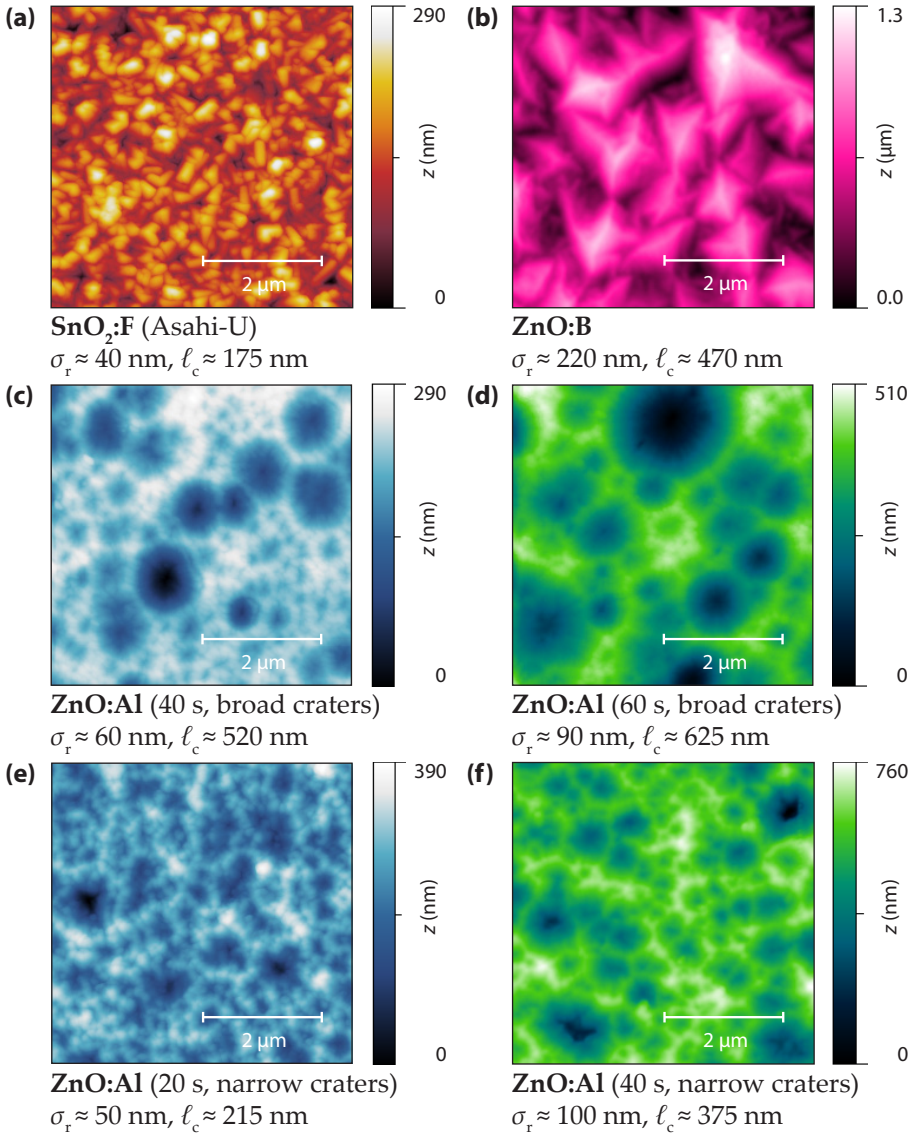

SnO_2:F (Asahi-U)
$\sigma_r \approx 40$ nm, $\ell_c \approx 175$ nm

ZnO:B
$\sigma_r \approx 220$ nm, $\ell_c \approx 470$ nm

ZnO:Al (40 s, broad craters)
$\sigma_r \approx 60$ nm, $\ell_c \approx 520$ nm

ZnO:Al (60 s, broad craters)
$\sigma_r \approx 90$ nm, $\ell_c \approx 625$ nm

ZnO:Al (20 s, narrow craters)
$\sigma_r \approx 50$ nm, $\ell_c \approx 215$ nm

ZnO:Al (40 s, narrow craters)
$\sigma_r \approx 100$ nm, $\ell_c \approx 375$ nm

Figure 3.4.: The morphology, rms roughness and correlation length of selected TCO samples.

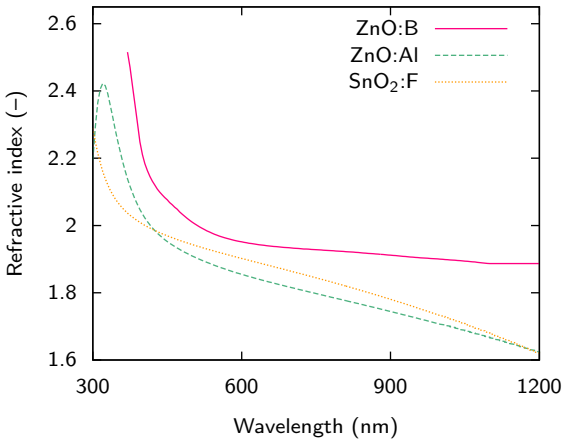

Figure 3.5.: The real parts of the refractive indices of three TCO materials.

multiple reflections, the electromagnetic field in the integrating sphere becomes homogeneous, which allows measuring T_{tot} (R_{tot}). By removing the cap on the transmission (reflection) port, the specular transmitted (reflected) light can leave the integrating sphere so that T_{dif} (R_{dif}) is measured.

For optimal results the sphere has to be coated with a material that is both highly scattering and highly reflective over a very broad wavelength range. Spectralon®, a polytetraflouroethylene-based material from Labsphere, fulfils these requirements and therefore is the state-of-the art coating material for ISs [78]. Since the field in the sphere is homogenous it is sufficient to measure the intensity at one point of the sphere. In our sphere, two detectors are mounted at the bottom of the sphere: A photomultiplier tube that works in the ultraviolet and visible regions of the spectrum and a PbS detector that copes with the near infrared range. Switching between the two detectors is done at 860.60 nm.

The first IS was built by Richard Ulbricht in 1900 [79]. While the theory for a perfect IS with openings of negligible size is rather simple, a rigorous treatment that takes the size of the openings into account is highly involved [80]. For a rigorous treatment also the splitting in diffuse and specular parts as it is done usually needs to be corrected [81]. Recently it was found that an additional diffusor is required to accurately measure the transmittance of patterned glass as it is used for wafer-based silicon solar cells [82]. For our use, however, it is sufficient to stick to the traditional method of relating the measured values to the total/diffuse transmittance (reflectance). Our IS uses unpolarized light.

To calibrate the IS for transmission, a measurement without sample and with the transmission port closed is done with the sample beam on to obtain the 100% reference signal, and with the sample beam off for the 0% reference signal. To calibrate for reflection, a measurement with a highly reflective material with known

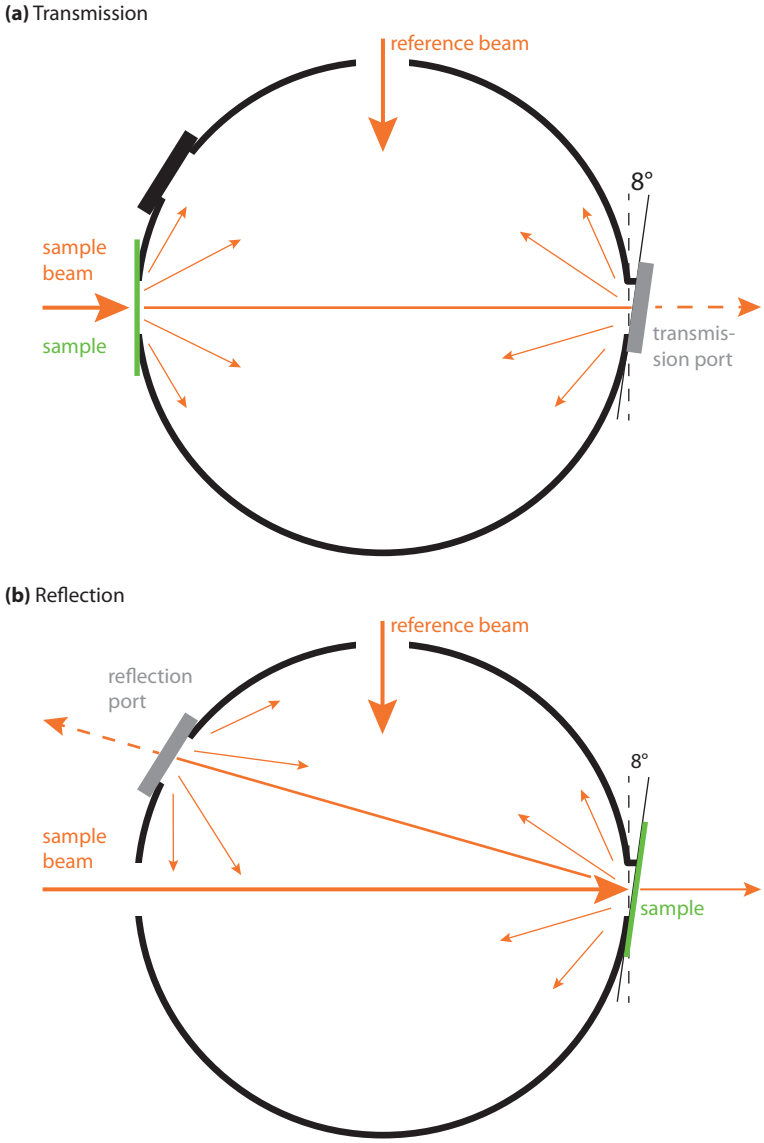

Figure 3.6.: Illustrating a horizontal section through an integrating sphere as it is used for measuring transmission (a) and reflection (b). To measure T_{tot} (R_{tot}), the transmission (reflection) port is closed. For measuring T_{dif} (R_{dif}), the transmission (reflection) port is open. The detectors are located at the bottom of the sphere (not shown in this figure).

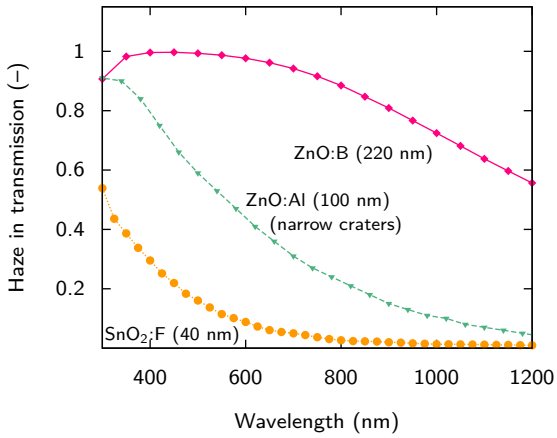

Figure 3.7.: The haze in transmission of different nano-textured TCO samples.

reflectance is performed. We use Spectralon as material. The measurement with the light beam on does therefore not correspond to 100% reflection but to the reflection of the material of Spectralon. The reflectance then is calculated with

$$R = \frac{(R_{\text{meas}} - R_{\text{dark}}) \cdot R_{100}}{R_{100} - R_{\text{dark}}}, \tag{3.11}$$

with the measured value R_{meas} and the values of the calibration run with the lamp on (R_{100}) and off (R_{dark}).

3.3.2. Spectrophotometer

The IS is an accessory of a PerkinElmer® Lambda™ 950 spectrophotometer. The spectrophotometer is equipped with a deuterium arc lamp for ultraviolet light and a tungsten-halogen lamp for visible and infrared light. With these two lamps a wavelength spectrum between 175 nm and 3300 nm is covered.

3.3.3. The haze of selected samples

Figure 3.7 shows the haze in transmission of three different nano-textured TCO samples. As we can see, the haze in general increases with increasing rms roughness. Further, the haze decreases with increasing wavelength. Both trends can be made plausible by stating that the haze is related to the ratio σ_r/λ_0. We discuss the relation between σ_r and λ_0 in Chapter 4.

3.4. The angular intensity distribution (AID)

3.4.1. A little history of AID measurements

Many setups have been developed to measure the AID, the BTDF or the directional spectral-reflectance distribution (BRDF). We mention some of them as examples: Many setups use lasers as light sources, so that the AID only can be measured for several distinct wavelengths. Among those we mention the angular resolved scattering setups used by Schade and Smith [83], Krč *et al.* [58, 59] and Fraunhofer IOF, Germany [64, 84]. The latter was also used to determine surface parameters of the investigated surfaces. Some setups were developed that are able to measure in broader wavelength bands by combining different tuneable and non-tuneable lasers. Amra *et al.* could determine the AID for a broad band in the visible and also in the near- and mid-infrared [85]. Serrot *et al.* developed a device to measure the BRDF in order to analyse signals reflected by Earth in the solar spectrum [86]. Zhang *et al.* used a halogen light source together with a spectrometer in order to determine the BRDF [87].

In 2003, Nijnatten introduced the Automated Reflectance/Transmittance Analyzer (ARTA) [88]. This setup is connected to a spectrophotometer that in our case provides light of wavelengths between 175 nm and 3300 nm. The ARTA originally was designed as variable angle spectrometry setup, *i.e.* it is mainly used to determine specular transmission and reflection spectra of flat layer stacks at different incident angles. If the ARTA, however, is used as angular resolved scattering setup it is possible to measure the AID in a broad spectrum.

3.4.2. Automated Reflectance/Transmittance Analyser

A schematic of the Automated Reflectance/Transmittance Analyser (ARTA) that we used to measure the AID in a broad wavelength range is shown in Fig. 3.8.

The ARTA setup can utilise the wavelength range provided by the spectrophotometer, which was characterised in Section 3.3.2. The ARTA is equipped with a polariser that allows measuring the optical properties for arbitrary polarisation. Measuring unpolarised light is not possible. For light detection the ARTA uses a photomultiplier tube for wavelengths shorter than 860.60 nm and a PbS detector for wavelengths longer than 860.60 nm. The detectors are situated in a little integrating sphere with a radius of 60 mm. Its angle with respect to the direction of the incident light can vary between $\theta = -170°$ and 170°. The angle formed by the sample normal and the direction of the incident light can be set between 0° (normal incidence of the light beam on the sample surface) and 90° (parallel incidence). While for normal incidence transmitted light in all directions can be measured, this is not possible for reflected light due to the design of the setup. All measurements presented in this thesis except the ones discussed in Chapter 6 were obtained for 0°.

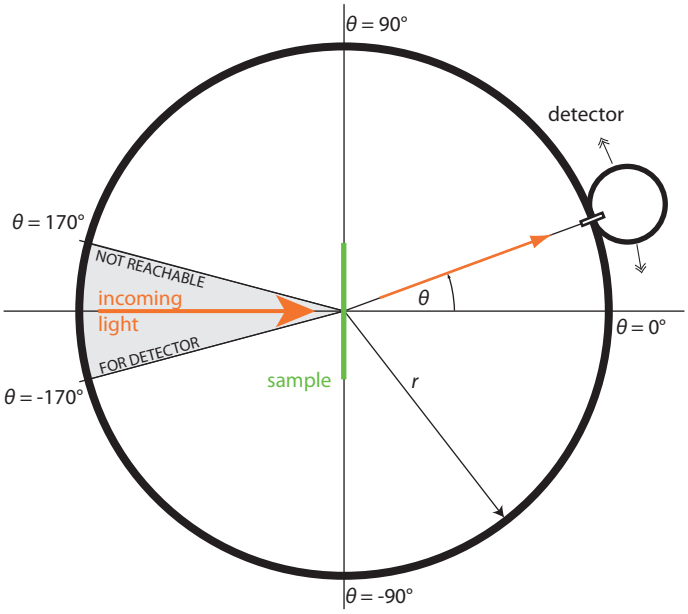

Figure 3.8.: Schematic cross section through the ARTA along the measurement plane. This plane is defined by the direction of the incoming light and the possible detector positions.

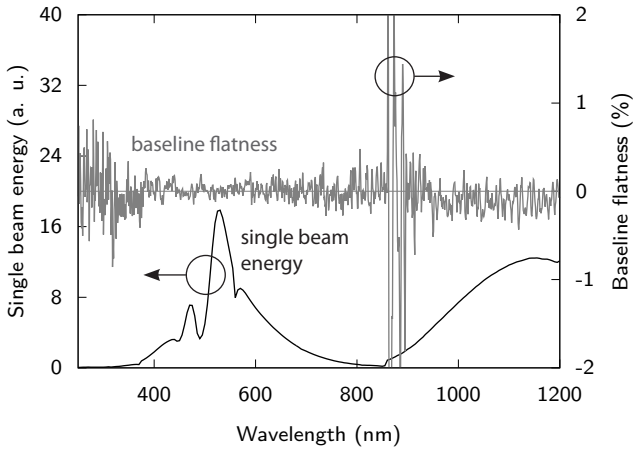

Figure 3.9.: Single beam energy and baseline flatness of the ARTA. Around the detector change region (860.60 nm), the single beam energy is lowest and the baseline flatness is worst, which is due to the bad performance of both detectors in this region. The definitions of these quantities are given in the text.

The ARTA measures the absorbance* $\mathfrak{A}(\lambda_0;\theta,\phi)$ that is related to the AID via

$$\mathrm{AID}(\lambda_0;\theta,\phi) = 10^{-\mathfrak{A}(\lambda_0;\theta,\phi)}. \tag{3.12}$$

By measuring $\mathfrak{A}$ and applying Eq. (3.12) the AID can be obtained over several orders of magnitude. In general, the AID will depend on both the polar angle θ and the azimuth ϕ. In that case it might be necessary to repeat the measurements for different azimuths of the sample. For isotropic samples this is not necessary and we can write

$$\mathrm{AID}(\lambda_0;\theta,\phi) \equiv \mathrm{AID}(\lambda_0,\theta). \tag{3.13}$$

However, due to the geometry of the detector slit, the measured intensity around the specular direction might differ considerably from the real value. We come back to this problem in Section 3.5.

Before a measurement starts, the ARTA is calibrated such that $\mathfrak{A}(\lambda_0, 0) \equiv 0$ when no sample is present. Figure 3.9 shows the single beam energy and the baseline flatness of the ARTA. The single beam energy is directly related to the detector signal and shows the combined effects of the lamp output and the spectral response of the optical system and the detector. The baseline flatness is obtained by remeasuring the 100% transmission baseline after calibration. Around the detector change region (860.60 nm), the single beam energy is lowest and the baseline flatness is worst, which is due to the poor performance of both detectors in this region.

3.4.3. The AID of selected samples

In this section we discuss the AID between 350 nm and 850 nm of the following samples: A SnO_2:F sample, a ZnO:Al sample with narrow craters, and a ZnO:B sample. The statistical parameters of these samples are shown in Fig. 3.4 (a), (f) and (b), respectively. Further we show results on a 1-D grating. From several 1-D rectangular periodic gratings with a period between 300 nm and 1000 nm and heights between 30 nm and 300 nm, we chose a 1-D grating with a period of 1000 nm and a height of 300 nm for the AID measurements. The gratings were formed on transparent glass substrates by a patterning technique developed by OM&T B.V. for Blu-ray Disc™ technology [89].

The measurements presented in this section were performed with a detector slit width of approximately 1.6 mm, which corresponds, for a sample-detector distance of 9 cm, to an opening angle of $\Delta\theta \approx 1°$. The spectral width of the incident light was set to 5 nm by the monochromator slit of the spectrophotometer. The integration time was 1 s. For the measurements the glass surface faced the incident light beam, *i.e.* the light entered the glass first and then propagated through the surface-textured layer.

*In spectroscopy, the term "absorbance", $\mathfrak{A}$, is defined as the logarithmic ratio of the intensity of light that traversed an absorber to the incident intensity. It is not to be confused with the absorptance A, which is the *fraction* of light that is absorbed.

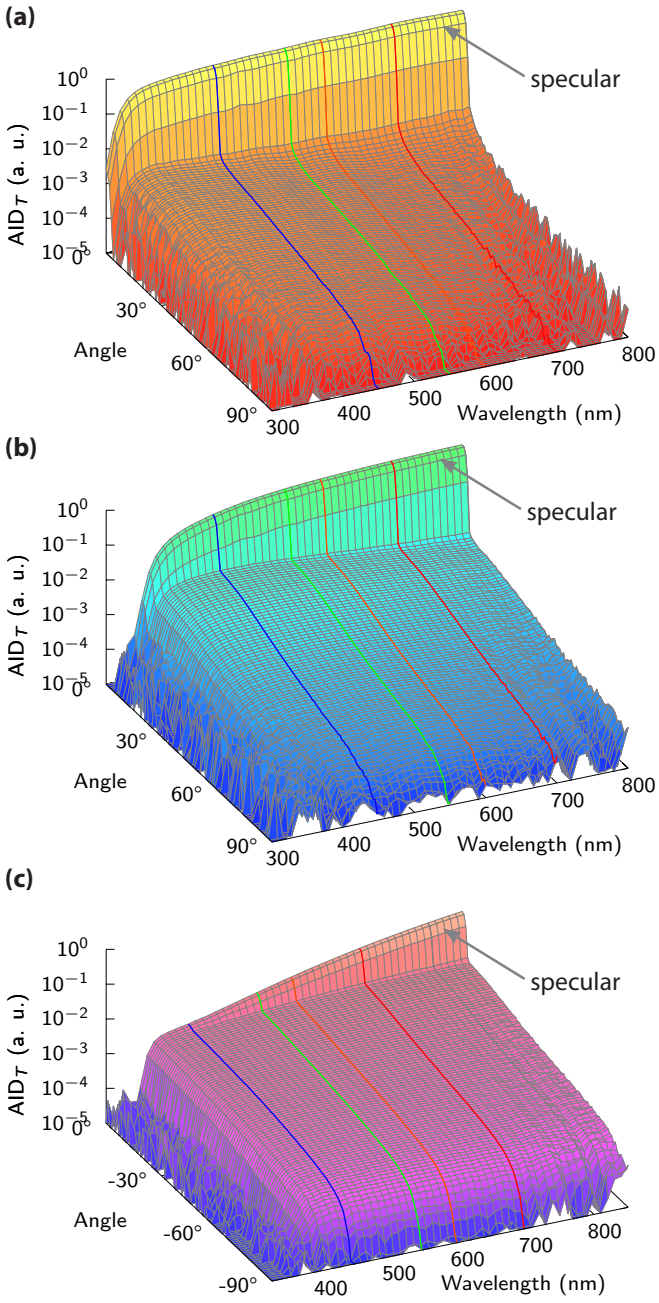

Figure 3.10.: Angular intensity distribution (AID) of *p*-polarized light that is scattered when transmitting a surface-textured layer of (a) SnO_2:F, (b) ZnO:Al and (c) ZnO:B. The AID is shown as function of the scattering angle θ, as depicted in Fig. 3.8 (a), and the wavelength. Specifications of the three materials are given in Fig. 3.4 (a), (f) and (b).

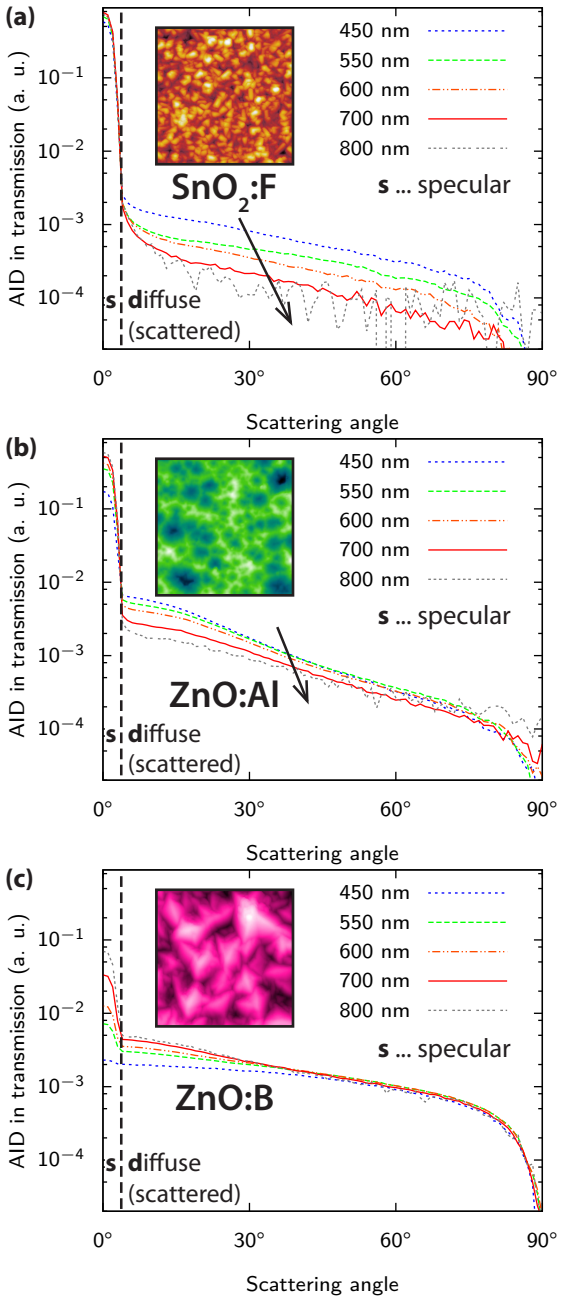

Figure 3.11.: AID of *p*-polarized light that is scattered when transmitting a surface-textured layer of ((a) SnO_2:F, (b) ZnO:Al and (c) ZnO:B. The AID is shown at several wavelengths in the visible. Specifications of the three materials are given in Fig. 3.4 (a), (f) and (b).

Figures 3.10 and 3.11 show the AID that was measured for the three different TCO materials. The measurements were performed in the visible range of the electromagnetic spectrum with a wavelength step of 10 nm. This allows to study wavelength dependent variations of the AID. In Fig. 3.11 sections for several wavelength in the visible are shown.

For SnO_2:F and ZnO:Al shown in Figs. 3.10 (a, b) and 3.11 (a, b) we observe only slight wavelength-dependent changes in the shape of the scattered light. The intensity of the scattered light declines as the angle becomes larger. Further the total amount of scattered light decreases while the specular intensity increases with increasing wavelengths. The increasing trend of the specular light intensity with wavelength is accompanied by a decreasing trend of the diffused light intensity, leading to a decline of H_T with increasing wavelength. These observations match with the results shown in Fig. 3.7.

The behaviour of ZnO:B, shown in Figs. 3.10 (c) and 3.11 (c), is very different. The specular part also increases with increasing wavelength, but the variation is much stronger. Further, in the diffuse region the AID of the very rough ZnO:B sample behaves differently compared to that of SnO_2:F and ZnO:Al. While the intensity increases slightly with increasing wavelengths at angles smaller than 45°, it stays constant for larger angles. The haze of ZnO:B peaks at 1 around 450 nm and decreases only slowly to 0.88 at 800 nm, which indicates that the increase of the specular intensity weighs slightly stronger than the increase of the diffuse intensity.

For all three materials, the noise level increases for larger wavelength, especially for SnO_2:F, where the intensity of the scattered light is lowest. For ZnO:B the intensity of the scattered light is higher than for the other two samples, which keeps the signal-to-noise ratio high, but also here a slight increase in the noise level is observed. This increase of the noise is connected to the performance of the photomultiplier tube that is used as detector below $\lambda_0 = 860.60$ nm. The performance of this detector decreases when approaching the switching wavelength, as can be seen in Fig. 3.9.

Figure 3.12 shows the AID at p- and s-polarisation at 600 nm of the SnO_2:F and ZnO:B samples introduced in Fig. 3.4 (a) and (b), respectively. We see that for the SnO_2:F sample the difference between the two polarisations is negligible. For ZnO:B it is slighlty larger, however, it still lies within the error margin. It is therefore sufficient to compare the AID calculated with the scattering model developed in Chapters 4 and 5 to the AID measured in p-polarisation only. In Section 5.7, where the light passes several interfaces at oblique directions before it is measured, and Chapter 6 where we investigate light at oblique incidence, we compare the simulated AID to the average of the two measured polarisations.

The AID of the 1-D grating in p-polarisation is shown in Fig. 3.13. In contrast to the nano-textured surfaces, where the AID decays monotonically, the AID of the 1-D grating shows maxima and minima. In the figure, the zeroth, first, second and third orders of diffraction are visible. The total amount of scattered light depends on the period, the height and the shape of the grating [89].

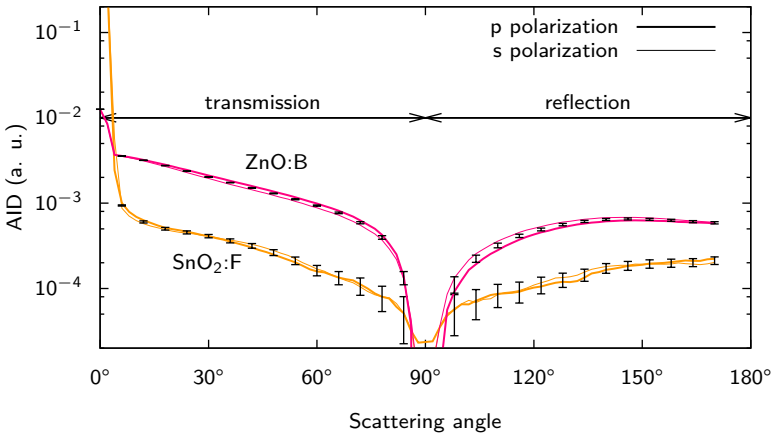

Figure 3.12.: The AID of two nano-texured surfaces at *p*- and *s*-polarisation at 600 nm.

3.5. Verification of the ARTA measurements

In this section we discuss several tests performed to determine the performance of the ARTA. We report on the reproducibility of the ARTA results and compare them to results obtained with an old single-wavelength (SW) ARS setup. Further we calculated the haze with the AID in order to compare this calculated haze with conventionally measured haze.

3.5.1. Reproducibility

To test the reproducibility of the measurements, we repeated five ARTA measurements at 633 nm. Again, the detector slit width was approximately 1.6 mm and the spectral width of the incident light was set to 5 nm by the monochromator slit of the spectrophotometer. The integration time was 1 s. During the measurements, the samples stayed in the ARTA, therefore the same spot of the samples was illuminated during all five measurements. For every angle, we calculated the average angular intensity distribution $\overline{\mathrm{AID}}$ and the relative standard deviation ς_{rel}. We performed this procedure for the strongly scattering ZnO:B and the weakly scattering SnO_2:F. Figure 3.14 (a) shows the obtained $(\overline{\mathrm{AID}}, \varsigma_{\mathrm{rel}})$ pairs for both materials. We see that the standard deviation increases polynomically with decreasing intensity. While $\varsigma_{\mathrm{rel}} \approx 1\%$ for the ZnO:B measurements, relative standard deviations exceeding 10% are common for SnO_2:F measurements, especially at low intensities, *i.e.* at large scattering angles. In order to reduce the standard deviation for low-intensity measurements, several measures can be taken:

One can increase the monochromator slit width and thus allow more light to traverse the slit. Further, one can increase the detector slit width such that more light can reach the detector. While opening the monochromator slit reduces the

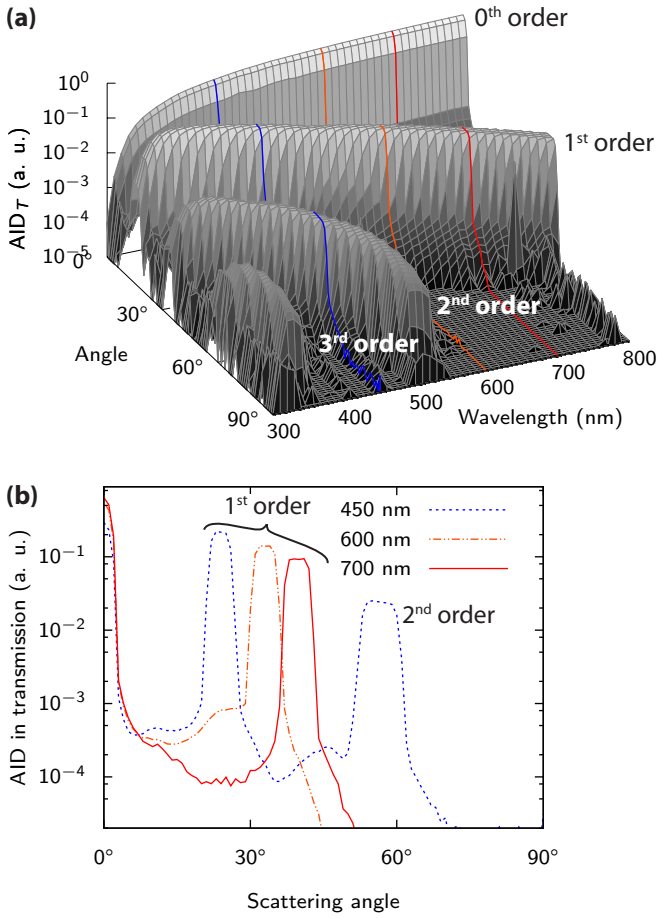

Figure 3.13.: AID of *p*-polarized light that is scattered when transmitting a 1D-grating. In (a) the AID is shown as function of the scattering angle θ, as depicted in Fig. 3.8 (a), and the wavelength. In (b) the AID at several wavelengths in the visible is shown. The grating has a period of 1 µm and a height of 300 nm. Its duty cycle is 50%.

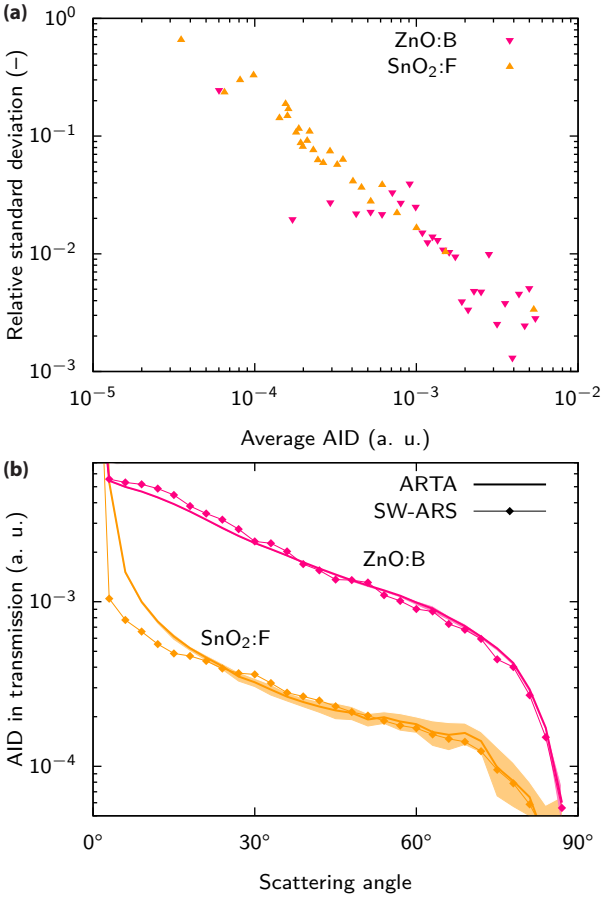

Figure 3.14.: (a) AID versus relative standard deviation for ARTA measurements of ZnO:B and SnO_2:F. (b) AID for ZnO:B and SnO_2:F measured with the SW-ARS and the ARTA at $\lambda_0 = 633$ nm. The thick lines represent the ARTA measurements while the thin dotted lines denote the ARS measurements. The standard deviation of the ARTA measurements is also shown.

spectral resolution, opening the detector slit reduces the angular resolution. A third measure is to increase the integration time.

At very low intensities, also stray light might become an issue. In this case the stray light intensity would have to be determined separately from the intensity in order to obtain the AID.

We also compared the AID at five different spots on the $2 \times 10\,\mathrm{cm}^2$ large SnO_2:F sample by taking five ARTA measurements at every spot. The average of these five measurements was then determined for each spot. Subsequently, we calculated the relative standard deviation for every scattering angle. The relative standard deviation varies between 3% around $\theta = 10°$ and 15% around $\theta = 70°$, where we omit larger scattering angles due to the large ς_{rel}. These variations are due to local variations of the surface morphology of the sample.

3.5.2. Comparison with single wavelength angular resolved scattering (SW-ARS)

We further compared the results obtained with the ARTA to results obtained with the SW-ARS setup. The SW-ARS consists of a photodetector that moves around the sample automatically and is connected to a lock-in amplifier. As light source a laser with $\lambda_0 = 633$ nm wavelength is used. Due to this laser, the reproducibility of the measurements is better, even for low intensities. For SnO_2:F, the relative standard deviation stays below 5% except close to $\theta = \pm 90°$. When measuring the AID with SW-ARS for different spots of the sample, the relative standard deviation varies between 5 and 15%. In contrast to the ARTA measurements, a deviation of 15% is also observed around 10°. This difference is due to the laser spot ($\approx 1\,\mathrm{mm}^2$) that is much smaller than the light spot in the ARTA ($\approx 28\,\mathrm{mm}^2$) and to the speckle noise that is inherent to the coherent laser light. One could increase the spot size of the laser in order to study the influence on the spot size in more detail. However, this is out of the focus of this work.

Figure 3.14 (b) shows the AID in transmission of ZnO:B and SnO_2:F, measured with the ARTA and SW-ARS. To be able to compare the ARTA and SW-ARS measurements, we scaled the SW-ARS data with a factor so that the least square difference of the two curves for scattering angles larger than 5°, *i.e.* away from the specular peak, was minimised. For ZnO:B, the results obtained with the two setups resemble each other very well. The small deviations are most likely due to local variations in the sample. For SnO_2:F, the differences between the ARTA and the SW-ARS measurements are larger. The specular peak is much narrower and higher for the SW-ARS measurements. The reason for this is the areal difference of the light spots. For larger angles small deviations are observed, which are within ς_{rel} of the ARTA measurements.

We summarise this discussion by stating that measuring low intensities with the ARTA is more elaborate than with SW-ARS. The very small size of the laser spot and the speckle noise of the coherent laser light make the SW-ARS setup more sensitive to local variations in the surface morphology. Compared to lo-

cal variations in surface morphology, the large standard deviations of the ARTA measurements at low intensities are tolerable. Finally, the incoherent light source in the ARTA mimics sunlight so that interference effects observed in the samples will be comparable to interference effects under real sunlight. This is an advantage in solar-cell research.

3.5.3. Determination of the haze from the ARTA results

A more involved method to verify the performance of the ARTA is calculating the haze in transmission using the AID data, and subsequently comparing this calculated haze to the haze measured with an integrating sphere.

The haze in reflection cannot be obtained since the specular reflected peak for normal incidence cannot be measured with the ARTA, as illustrated in Fig. 3.8.

Model

As defined in Eq. (3.2), the haze in transmission H_T is defined as the ratio of the diffuse transmittance T_{dif} to the total transmittance T_{tot},

$$H_T(\lambda_0) = \frac{T_{\text{dif}}(\lambda_0)}{T_{\text{tot}}(\lambda_0)}. \tag{3.14}$$

To enhance the readability, we omit the argument λ_0 in the further proceeding. We use spherical coordinates.

If, ideally, the AID were known at every point of the hemisphere into which light is transmitted, H_T could be calculated with

$$H_T = \frac{\int_{\theta_1}^{\frac{\pi}{2}} \int_0^{2\pi} \text{AID}(\theta', \phi') \sin\theta' \, \mathrm{d}\phi' \, \mathrm{d}\theta'}{\int_0^{\frac{\pi}{2}} \int_0^{2\pi} \text{AID}(\theta', \phi') \sin\theta' \, \mathrm{d}\phi' \, \mathrm{d}\theta'}, \tag{3.15}$$

where θ_1 denotes the border angle between the specular and diffuse directions. If the light is scattered by an isotropic sample the AID will not be dependent on the azimuth ϕ and Eq. (3.15) can be simplified to

$$H_T = \frac{2\pi \int_{\theta_1}^{\frac{\pi}{2}} \text{AID}(\theta') \sin\theta' \, \mathrm{d}\theta'}{2\pi \int_0^{\frac{\pi}{2}} \text{AID}(\theta') \sin\theta' \, \mathrm{d}\theta'}. \tag{3.16}$$

The AID of randomly surface-textured TCO layers is in a good approximation isotropic and therefore Eq. (3.16) can be applied. However, the AID is not measured at every scattering angle θ. We now assume that the angular distance between two points of the AID is $\Delta\theta$. It is then convenient to set the opening angle of the ARTA detector also to $\Delta\theta$ in order to assure that no angular portion of the scattered light hits the detector twice or not at all. At a position θ, the detector receives then light that is scattered into scattering angles in the interval

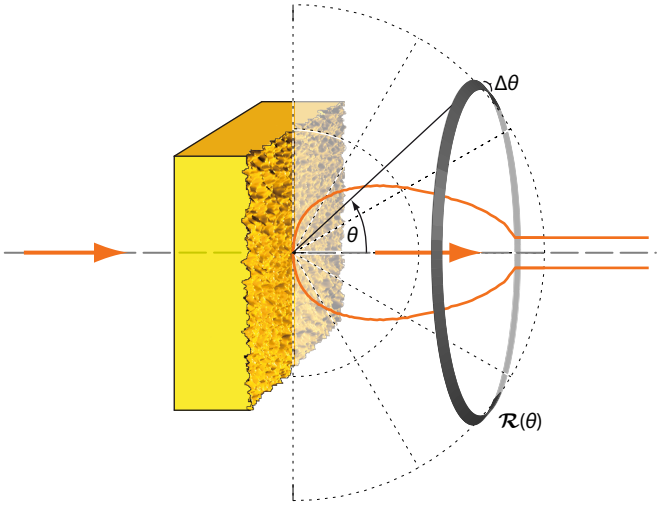

Figure 3.15.: Illustrating the ring $\mathcal{R}(\theta)$ of width $\Delta\theta$ that is used to calculate the haze in transmission.

$[\theta - \Delta\theta/2, \theta + \Delta\theta/2]$. As illustrated in Fig. 3.15, this interval corresponds to a ring $\mathcal{R}(\theta)$ on the hemisphere that in spherical coordinates is given by the set

$$\mathcal{R}(\theta) = [\theta - \Delta\theta/2, \theta + \Delta\theta/2] \times [0, 2\pi). \tag{3.17}$$

The solid angle covered by this ring is

$$\begin{aligned} \Omega_{\mathcal{R}(\theta)} &= \int_{\theta-\Delta\theta/2}^{\theta+\Delta\theta/2} \int_0^{2\pi} \sin\theta' \mathrm{d}\phi' \, \mathrm{d}\theta' \\ &= 4\pi \sin\theta \sin\frac{\Delta\theta}{2} \approx 2\pi\Delta\theta \sin\theta. \end{aligned} \tag{3.18}$$

The detector position $\theta = 0$ does not correspond to a ring but to a curved disc $\mathcal{R}(0)$ with 'radius' $\Delta\theta/2$. It covers the solid angle

$$\begin{aligned} \Omega_{\mathcal{R}(0)} &= \int_0^{\Delta\theta/2} \int_0^{2\pi} \sin\theta' \mathrm{d}\phi' \, \mathrm{d}\theta' \\ &= 2\pi \left[1 - \cos\frac{\Delta\theta}{2}\right] \approx \pi\frac{(\Delta\theta)^2}{4}. \end{aligned} \tag{3.19}$$

The approximation corresponds to neglecting the curvature of the hemisphere.

We further may assume that the intensity remains constant between $\theta - \Delta\theta/2$ and $\theta + \Delta\theta/2$ and therefore in the whole ring $\mathcal{R}(\theta)$. We obtain for the haze in transmission

$$H_T = \frac{\sum_{\theta_1<\theta\le\pi/2} \mathrm{AID}(\theta)\, \Omega_{\mathcal{R}(\theta)}}{\sum_{0\le\theta\le\pi/2} \mathrm{AID}(\theta)\, \Omega_{\mathcal{R}(\theta)}}, \tag{3.20}$$

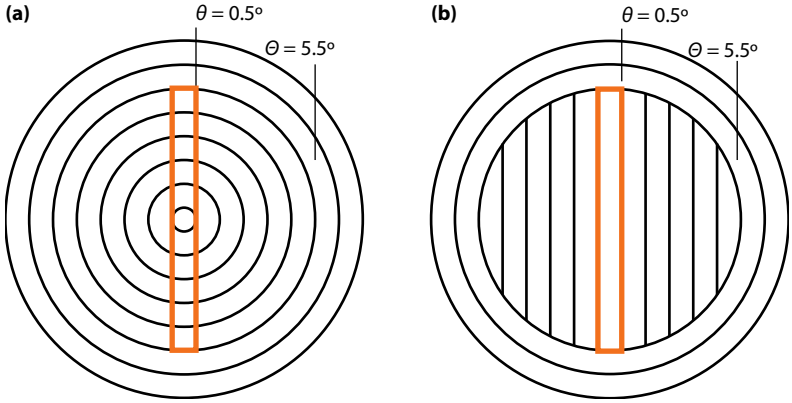

Figure 3.16.: (a) The detector slit (thick rectangle) is shown with respect to the rings. (b) The rings are replaced by stripes for angles smaller than $\Theta = 5.5°$.

where the sum is taken over the angles at which the AID is measured.

Calibration of the model

Before we can calculate the haze with Eq. (3.20), we have to take a closer look at the shape of the detector slit: The detector slit width in the measurements was approximately 1.6 mm, corresponding to $\Delta\theta \approx 1°$, which is also the angular distance between two subsequent measurements, as mentioned in Section 3.4.2. However, the slit height is 17 mm, which corresponds to an opening angle of approximately 10°. The detector will measure all the light that hits the slit. Figure 3.16 (a) shows the rings $\mathcal{R}(\theta)$, as defined in Eq. (3.17), superimposed with the slit. It is obvious that $\mathrm{AID}(\theta)$, *i.e.* the mean AID of the light that hits the detector slit, at $\theta = 0$ is much smaller than the real intensity in the specular direction, *i.e.* in the disc $\mathcal{R}(0)$. The power transmitted in the specular direction therefore is underestimated in this approach.

To overcome this problem, the rings $\mathcal{R}(\theta)$ have to be replaced by stripes $\mathcal{S}(\theta)$ for angles smaller than an angle Θ, as depicted in Fig. 3.16 (b). For angles larger than Θ, the ring approximation still holds. For the areas of the stripes for $\theta < \Theta$ we obtain

$$\Omega_{\mathcal{S}(\theta)} = 2\left[\theta'\sqrt{\Theta^2 - \theta'^2} + \theta'^2 \arcsin\frac{\theta'}{\Theta}\right]_{\theta'=\theta+\Delta\theta/2}^{\theta'=\theta-\Delta\theta/2}. \tag{3.21}$$

For the stripe at 0° we get

$$\Omega_{\mathcal{S}(0)} = \Delta\theta\sqrt{\Theta^2 - \left(\frac{\Delta\theta}{2}\right)^2} + \frac{\Delta\theta^2}{2}\arcsin\left(\frac{\Delta\theta}{2\Theta}\right). \tag{3.22}$$

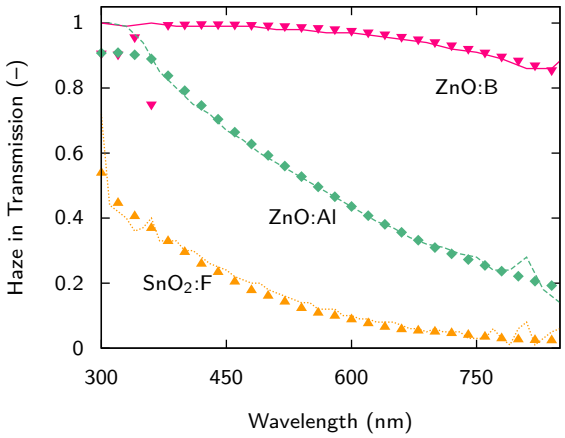

Figure 3.17.: Haze in transmission calculated from the AID obtained with the ARTA (lines) and directly measured with the IS (symbols) for the three randomly surface-textured TCO materials introduced in Section 3.2.3. Haze calculated according to Eq. (3.20) with $\Omega_{\mathcal{R}(\theta)}$ from Eq. (3.18) for $\theta > \Theta$ and $\Omega_{\mathcal{S}(\theta)}$ from Eqs. (3.21) and (3.22) for $\theta < \Theta$.

Figure 3.17 shows the haze calculated from the AID by using Eq. (3.20) with $\Omega_{\mathcal{R}(\theta)}$ from Eq. (3.18) for $\theta > \Theta$ and $\Omega_{\mathcal{S}(\theta)}$ from Eqs. (3.21) and (3.22) for $\theta < \Theta$, with $\Theta = 5.5°$. The border angle was taken as $\theta_1 = 5°$, which corresponds to the opening angle of the hole through which the specular light leaves the integrating sphere. In order to compare the haze obtained via the ARTA with reliable data, H_T also was measured with the integrating sphere. The measurements were performed for the three randomly surface-textured TCO materials, since their AID in good approximation is isotropic, *i.e.* independent of the azimuth. Since this is not true for the 1-D grating, the haze cannot be determined with the ARTA. The haze data obtained with the integrating sphere and the ARTA are in good agreement despite the large standard deviations of the ARTA measurements for low intensities.

Comment

We conclude this discussion by stating that Eq. (3.20) can be used for determining the haze with generic VAS setups, if the surface morphology of the investigated samples is isotropic. The area of the hemispherical elements $\Omega_{\mathcal{R}(\theta)}$ might deviate from the theoretical values given in Eqs. (3.18) and (3.19), according to the architecture of the used setup. We, for example, had to correct for small scattering angles.

3.6. The AID of a textured TCO-silicon interface

While the AID† of TCO-air interfaces can be measured as described in the previous sections, a few additional issues have to been taken into account when we want to measure the AID of TCO-silicon interfaces:

1. The silicon layer absorbs the light traversing it. Therefore we have to use detectors that are able to detect low intensities or a light source that is strong enough to provide the detectors with a sufficient intensity. However, light trapping is most important in the infrared, where the silicon has a low absorptance. Due to the low absorptance, measuring in the near infrared is possible.

2. When a silicon layer is deposited onto a rough TCO layer, the silicon-air interface also will exhibit a certain roughness. When depositing microcrystalline silicon, the material itself will be rough due to its microstructure. Therefore light traversing the layer stack will not only be scattered by the TCO-silicon interface, but also by the silicon-air interface. This makes it impossible to extract the AID of the TCO-silicon interface from the AID measured for the whole layer stack. To solve this problem, one can polish the rough silicon surface so that the light is only scattered by the TCO-silicon interface.

3. Even if the silicon-air interface is polished, light interacts with this interface: It is partially reflected back into the silicon and it is refracted at the silicon-air interface. Considering these three effects, we then can relate the AID at the TCO-silicon interface (*i.e.* inside the silicon) to the AID in the air via

$$\mathrm{AID}_{\mathrm{Si}}(\theta_{\mathrm{Si}}) \cdot \Omega_{\mathrm{Si}} = \mathrm{AID}_{\mathrm{air}}(\theta_{\mathrm{air}}) \cdot \frac{1}{T} \cdot \exp\left(\alpha_{\mathrm{Si}} \frac{d}{\cos\theta_{\mathrm{Si}}}\right) \cdot \Omega_{\mathrm{air}}, \tag{3.23}$$

   where T is the transmittance of the silicon-air interface as obtained from the Fresnel equations, d is the average thickness of the silicon layer and α_{Si} is the absorption coefficient of the silicon. The scattering angles θ_{Si} and θ_{air} are related to each other via Snell's law. Due to the conservation of the étendue, the solid angle Ω_{Si} of the detector differs from the solid angle Ω_{air} into which the light that reaches the detector is emitted [90]. These two solid angles are related to each other via

$$\frac{\Omega_{\mathrm{Si}}}{\Omega_{\mathrm{air}}} = \frac{n_{\mathrm{Si}}^2}{n_{\mathrm{air}}^2} \cdot \frac{\cos\theta_{\mathrm{Si}} \cdot \cos\psi_{\mathrm{Si}}}{\cos\theta_{\mathrm{air}} \cdot \cos\psi_{\mathrm{air}}} = n_{\mathrm{Si}}^2 \cdot \frac{\cos\theta_{\mathrm{Si}}}{\cos\theta_{\mathrm{air}}}. \tag{3.24}$$

   In Eq. (3.24) we took into account that the detector moves around the $x-z$ plane and that the azimuth ψ therefore is zero.

†By "AID" we mean the "AID in transmission" throughout this section.

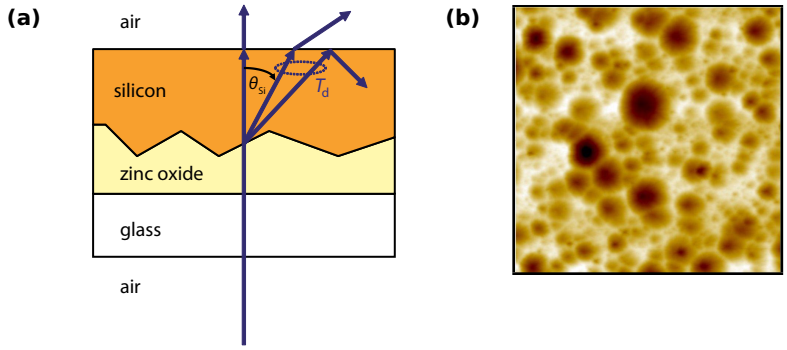

Figure 3.18.: (a) Sample geometry and (b) a 10×10 µm^2 AFM scans of the rough, crater-like ZnO interface with a height range of 610 nm.

We further approximated the refractive index of the air n_{air} to be 1. We thus find that the AID inside the silicon can be retrieved from the measured AID in air with the equation

$$\text{AID}_{\text{Si}}(\theta_{\text{Si}}) = \text{AID}_{\text{air}}(\theta_{\text{air}}) \cdot \frac{1}{T} \cdot \exp\left(\alpha_{\text{Si}} \frac{d}{\cos\theta_{\text{Si}}}\right) \cdot n_{\text{Si}}^2 \cdot \frac{\cos\theta_{\text{Si}}}{\cos\theta_{\text{air}}}. \tag{3.25}$$

In reality, light that leaves the layer stack via the silicon-air interface after multiple reflections also will contribute to the measured AID and therefore also will contribute to the AID_{Si} that is obtained with Eq. (3.25). The AID_{Si} therefore differs from the (hypothetical) AID_{Si} of light that is scattered into a half space filled with silicon. We also note that the AID_{Si} only can be obtained up to the critical angle $\theta_c = \arcsin(1/n_{\text{Si}})$.

Figure 3.18 (a) illustrates the geometry of the investigated sample. To prepare the sample we deposited sputtered ZnO:Al onto a Corning glass substrate. After deposition the ZnO:Al was etched in 0.5 weight percent diluted hydrochloric acid for 30 s. Due to the etching a crater-like texture with a root mean square roughness of 78 ± 2 nm was created, as can be seen in Fig. 3.18 (b), which shows an atomic force microscopy (AFM) scan of the ZnO:Al surface. Onto the ZnO:Al we deposited a 3 µm thick nc-Si:H layer by plasma-enhanced chemical vapour deposition and polished the silicon surface, resulting in a root mean square roughness of 9 ± 2 nm. The average thickness of the silicon layer after polishing is estimated to be approximately 2.3 µm. We extracted the refractive indices and absorption coefficients with ellipsometry: The refractive indices at 780 nm are $n_{\text{ZnO}} = 1.65$ and $n_{\text{Si}} = 3.70$. The absorption coefficients at 780 nm are $\alpha_{\text{ZnO}} = 369$ cm^{-1} and $\alpha_{\text{Si}} = 860$ cm^{-1}. The critical angle at the silicon-air interface is then $\theta_c = 15.68°$.

We measured the AID of the glass-ZnO-silicon‡ layer stack in at a wavelength of 780 nm. We used two setups: A Bruker IFS 66v Fourier transform infrared

‡For the sake of simplicity we denote "ZnO:Al-(µc-Si:H)" by "ZnO-silicon".

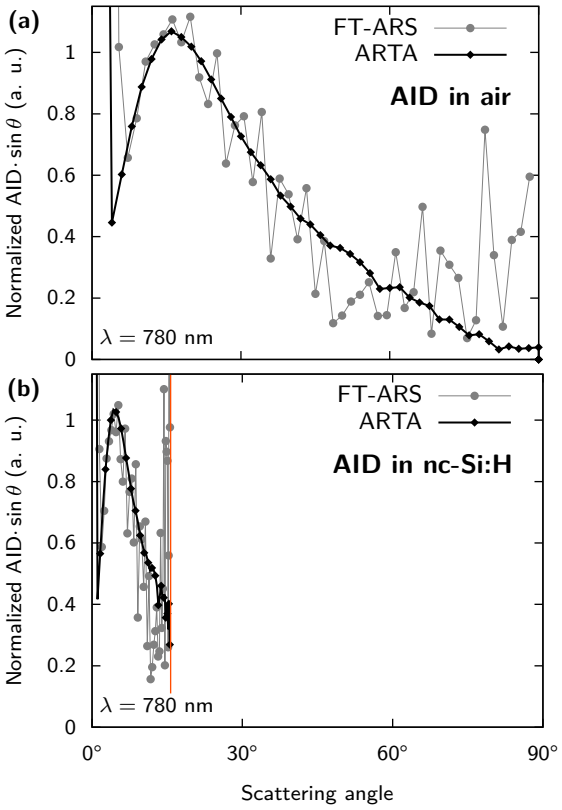

Figure 3.19.: (a) The AID· $\sin\theta$ in air measured with the Fourier transform angular resolved scattering setup (FT-ARS) and the Automated Reflectance / Transmittance Analyser (ARTA). (b) The AID· $\sin\theta$ inside the silicon layer obtained from the results in (a) with Eq. (3.25). The critical angle θ_c of the silicon-air interface is indicated by the vertical orange line.

spectrometer that was equipped with a self-assembled angular resolved scattering accessory (FT-ARS), and the ARTA, which was discussed in sections 3.4 and 3.5. Figure 3.19 (a) shows the AID in air that was measured with the two setups. Although the trends of the FT-ARS and the ARTA measurements resemble each other, the FT-ARS measurement is much noisier. While the ARTA results keep decreasing with increasing angles, the FT-ARS results suggest saturation of the AID for angles larger than 60°. The specular peak is broader for the FT-ARS. This is due to different detector opening angles and light beam sizes of the two setups. Figure 3.19 (b) shows the AID in silicon as it was obtained from the AID in air with Eq. (3.25). Due to the large refractive index of silicon, only the AID for angles smaller than 15.68° can be obtained. For further analysis we will proceed with the data obtained by the ARTA since it is much smoother. The AIDs shown in Fig. 3.19 are normalised. The normalisation procedure is discussed in Appendix A.

3.7. Conclusions

In this chapter we introduced the different measurement techniques needed to evaluate the scattering models that we develop in the next chapters. We discussed atomic force microscopy for determining the morphology of the nano textures. To obtain the total and diffuse transmittance and reflectance and hence the haze we discussed the principles of the integrating sphere.

We further discussed how the angular intensity distribution (AID) can be accurately obtained between the near ultraviolet and the near infrared. Due to the novelty of the approach we discussed this topic thoroughly: To measure the AID, we used the Angular Reflectance/Transmittance Analyzer (ARTA) as angular resolved scattering (ARS) setup for broad wavelength measurements. The ARTA was originally developed for variable angle spectrometry, *i.e.* measuring specular transmittance and reflectance spectra at different incident angles. Due to the ability to measure the multi-wavelength AID, the ARTA is superior to single wavelength ARS setups. To verify the ARTA measurements we compared the AIDs obtained with the ARTA with the AIDs obtained with a laser based SW-ARS setup. This comparison revealed that the reproducibility at low intensities is inferior for the ARTA. However, the incoherent light source in the ARTA resembles the sunlight better and prevents from measuring artefacts that could be present when measuring with fully coherent laser light. If the required spectral and/or angular resolution are not that high, the reproducibility of the ARTA can be increased by opening the monochromator slit and/or the detector slit. As another verification of the ARTA measurements we determined the haze in transmission from the AID data and compared the results to direct haze measurements.

I believe there is no philosophical high-road in science, with epistemological signposts. No, we are in a jungle and find our way by trial and error, building our road behind us as we proceed.

Max Born

4

A little history of the scalar scattering theory

4.1. Introduction

Due to increasing computer capacity, rigorous solvers of the Maxwell equations, like the Finite Difference Time Domain (FDTD) method [91, 92] or the Finite Elements Method (FEM) [93], have become very popular in recent years. Nonetheless the scalar scattering theory still is a very powerful instrument for estimating the scattering properties of nano-textured interfaces. The main tool of the scalar scattering theory are diffraction integrals, such as the *Fresnel-Kirchhoff diffraction formula*, from which the *Fraunhofer* and *Fresnel diffraction integrals* can be deduced as first order and second order approximations, respectively, and the *Rayleigh-Sommerfeld diffraction integrals* [94].

In this chapter we review how the scalar scattering theory was utilised by the thin-film silicon solar cell community in the last years. After discussing the fundamentals of the scalar scattering theory in Section 4.2, we present a semi-empirical model to calculate the haze parameters of nano-textured TCO materials and discuss the drawbacks of that approach in Section 4.3. In Sections 4.4 and 4.5 we describe first attempts to calculate the AID with the scalar scattering theory and discuss the limitations of this approach.

4.2. The scalar scattering theory

The electromagnetic theory is based on the four Maxwell equations.* These equations are a set of partial differential equations that combine the electric field **E** and the magnetic induction **B** with each other. If the equations are applied to a macroscopic system, also the electric displacement **D** and the magnetic field **H** are used. In the differential formulation the Maxwell equations in the absence of charge or current sources are given by

$$\begin{aligned} \nabla \cdot \mathbf{D}(\mathbf{r},t) &= 0, & \nabla \times \mathbf{E}(\mathbf{r},t) &= -\frac{\partial \mathbf{B}(\mathbf{r},t)}{\partial t}, \\ \nabla \cdot \mathbf{B}(\mathbf{r},t) &= 0, & \nabla \times \mathbf{H}(\mathbf{r},t) &= +\frac{\partial \mathbf{D}(\mathbf{r},t)}{\partial t}. \end{aligned} \tag{4.1}$$

If we assume that the solutions to the Maxwell equations have an harmonic time dependence $\exp(-i\omega t)$ from which arbitrary solutions can be built by Fourier superpositions, we can use frequency dependent amplitudes $\mathbf{E}(\mathbf{r},\omega)$, $\mathbf{B}(\mathbf{r},\omega)$ *etc.*, instead of the time dependent fields used in Eq. (4.1) [95]. In this so-called *frequency domain* the Maxwell equations read as

$$\begin{aligned} \nabla \cdot \mathbf{D}(\mathbf{r},\omega) &= 0, & \nabla \times \mathbf{E}(\mathbf{r},\omega) &= +i\omega \mathbf{B}(\mathbf{r},\omega), \\ \nabla \cdot \mathbf{B}(\mathbf{r},\omega) &= 0, & \nabla \times \mathbf{H}(\mathbf{r},\omega) &= -i\omega \mathbf{D}(\mathbf{r},\omega). \end{aligned} \tag{4.2}$$

Let us now look at a macroscopic system that is isotropic and responses linearly to an applied field. Then, the fields **E** and **D**, and **B** and **H**, respectively, are connected via

$$\mathbf{D}(\mathbf{r},\omega) = \varepsilon_0 \varepsilon(\mathbf{r},\omega)\mathbf{E}(\mathbf{r},\omega) \qquad \text{and} \qquad \mathbf{H}(\mathbf{r},\omega) = \frac{1}{\mu_0 \mu(\mathbf{r},\omega)}\mathbf{B}(\mathbf{r},\omega). \tag{4.3}$$

ε is the relative permittivity, μ is the relative permeability, and ε_0 and μ_0 are the permittivity and the permeability of free space, respectively. In free space, $\varepsilon \equiv \mu \equiv 1$.

From the Maxwell equations, the wave equations of the electromagnetic field can be derived.† They are given by‡

$$\nabla^2 \mathbf{E} + \varepsilon\mu k_0^2 \mathbf{E} + (\nabla \ln \mu) \times (\nabla \times \mathbf{E}) + \nabla(\mathbf{E} \cdot \nabla \ln \varepsilon) \quad = 0, \tag{4.4a}$$

$$\nabla^2 \mathbf{H} + \varepsilon\mu k_0^2 \mathbf{H} + (\nabla \ln \varepsilon) \times (\nabla \times \mathbf{H}) + \nabla(\mathbf{H} \cdot \nabla \ln \mu) = 0, \tag{4.4b}$$

with the wavenumber *in vacuo*

$$k_0 = \omega / c_0, \tag{4.5}$$

*See *e.g.* Ref. [95], Chapter 6. The Maxwell equations also are presented in Ref. [94], Section 1.1. There, however, they are formulated in the Gaussian unit-system instead of the SI system.

†See *e.g.* Ref. [94], Section 1.2.

‡In Eqs. (4.4a) and (4.4b), we omitted the arguments $(\mathbf{r},\omega)$ for **E**, **B**, ε and μ for better readability.

where $c_0 = 1/\sqrt{\varepsilon_0 \mu_0}$ is the speed of light *in vacuo*.

Let us now consider that the electromagnetic field is incident on a linear, isotropic and nonmagnetic medium. Then, Eq. (4.4a) can be simplified to:[§]

$$\begin{aligned} \nabla^2 \mathbf{E}(\mathbf{r}, \omega) + k_0^2 \varepsilon(\mathbf{r}, \omega) \mathbf{E}(\mathbf{r}, \omega) \\ + \nabla [\mathbf{E}(\mathbf{r}, \omega) \cdot \nabla \ln \varepsilon(\mathbf{r}, \omega)] = 0. \end{aligned} \tag{4.6}$$

Since the last term of Eq. (4.6) couples the Cartesian components of the electric field, the solution of this equation is rather difficult. But the equation can be simplified if we assume that the dielectric function $\varepsilon(\mathbf{r})$ varies so slowly with position that it is effectively constant over distances of the order of the wavelength $\lambda_0 = 2\pi/k_0$. In this case the last term of the left-hand side of Eq. (4.6) can be neglected and we obtain

$$\nabla^2 \mathbf{E}(\mathbf{r}, \omega) + k_0^2 n^2(\mathbf{r}, \omega) \mathbf{E}(\mathbf{r}, \omega) = 0. \tag{4.7}$$

Here we used the relation $\varepsilon(\mathbf{r}, \omega) = n^2(\mathbf{r}, \omega)$, where $n(\mathbf{r})$ is the refractive index. Unlike in Eq. (4.6), the Cartesian components in Eq. (4.7) are not coupled to each other, which allows to solve this equation for each component separately. In fact, the solution of one component gives a good insight into the general behaviour of the solution of Eq. (4.7). Denoting this component by $U(\mathbf{r}, \omega)$, we obtain the scalar equation

$$\nabla^2 U(\mathbf{r}, \omega) + k_0^2 n^2(\mathbf{r}, \omega) U(\mathbf{r}, \omega) = 0. \tag{4.8}$$

This equation is the fundamental equation of the scalar scattering theory and will be used in the following sections to calculate the haze parameters and the angular intensity distribution. We define U such that the normalised intensity $\mathcal{I}(\mathbf{r}) = I(\mathbf{r})/I_0$ at a position $\mathbf{r}$, where I_0 is the intensity of the incident light, is given by

$$\mathcal{I}(\mathbf{r}, \omega) = U^*(\mathbf{r}, \omega) U(\mathbf{r}, \omega) = |U(\mathbf{r}, \omega)|^2, \tag{4.9}$$

where * denotes the complex conjugate. However, we always have to keep the approximations in mind that were used in the derivation of Eq. (4.8):

1. The medium that scatters the light is linear, isotropic and nonmagnetic.
2. The variations of the refractive index $n(\mathbf{r})$ are so small in the order of the wavelength λ_0 that they can be neglected.

4.3. A semi-empirical haze model

According to Eq. (3.2), expressions for the total and diffuse transmittance and reflectance have to be found to calculate H_T and H_R.

[§] See *e.g.* Ref. [94], Section 13.1.

In 1954, Davies presented a model on the reflection of electromagnetic waves from a rough surface [96]. This model was based on the scalar scattering theory and on statistics and was developed under the following assumptions:

1. The surface is not so precipitous that some parts of the surface are shielded from incident radiation, *i.e.* there is no shadowing.

2. The surface is perfectly conducting and the surface currents are of the same magnitude as those set up in a plane reflector, but with the phase of the current at a point varying in a random manner connected with the height of the surface.

3. The surface is only slightly rough, *i.e.* $z/\lambda_0 \ll 1$ and $\sigma_r/\lambda_0 \ll 1$.

4. The height distribution $z(x,y)$ is Gaussian, *i.e.* the probability to find a height z is given by

$$p(z) = \frac{1}{\sigma_r\sqrt{2\pi}} \exp\left(-\frac{z^2}{2\sigma_r^2}\right). \tag{4.10}$$

   This assumption is reasonable if the surface roughness is caused by a large number of contributing factors. Note that the standard deviation of this distribution is σ_r, the rms roughness of the surface.

5. The autocorrelation function of the surface irregularities is also Gaussian, with the standard deviation ℓ_c:

$$\left\langle z\left(x,y\right) z\left(x',y'\right)\right\rangle = \sigma_r^2 \left\{-\frac{1}{\ell_c^2}\left[\left(x-x'\right)^2 + \left(y-y'\right)^2\right]\right\}. \tag{4.11}$$

Under these assumptions the reflected radiation can be written as[¶]

$$\left\langle |U|^2 \right\rangle = \langle U\rangle^2 + \left\langle |U - \langle U\rangle|^2 \right\rangle, \tag{4.12}$$

i.e. as a sum of a coherent (specular) and incoherent (diffuse) component. If a monochromatic wave with incident angle ψ is reflected at a very large, slightly rough surface the specular reflected wave will contain a fraction

$$\exp\left[-\left(\frac{4\pi\sigma_r}{\lambda_0}\right)^2 \cos^2\psi\right] \tag{4.13}$$

of the incident intensity.

[¶] Instead of the field U, Davies works with the electric field strength $\mathcal{E}$.

By modifying Eq. (4.13), Bennett and Porteus found an expression for the specular reflectance R_{spec} at normal incidence ($\psi = 0$), when the surface is not perfectly conducting [97]:

$$R_{\text{spec}}(\lambda_0) = R_0 \cdot \exp\left[-\frac{(4\pi\sigma_r)^2}{\lambda_0^2}\right]. \tag{4.14}$$

R_0 is the reflectance of a perfectly smooth surface of the same material. From Davies' theory, they further derived an expression for the diffuse part of the reflected light,

$$\int_0^{\Delta\theta} r_d(\lambda_0, \theta)\,\mathrm{d}\theta = R_0 \frac{2^5\pi^4}{m^2}\left(\frac{\sigma_r}{\lambda_0}\right)^4 (\Delta\theta)^2, \tag{4.15}$$

where $\Delta\theta$ is the acceptance angle of the instrument that measures the reflectance. The square slope m of the profile of the surface is related to the rms roughness σ_r and the correlation length ℓ_c via $\ell_c = \sqrt{2}\sigma_r/m$. Note that the amount of diffuse light decreases very fast with wavelength. The complete measured reflectance R_{tot} can then be written as

$$R_{\text{tot}}(\lambda_0) = R_0 \cdot \exp\left[-\frac{(4\pi\sigma_r)^2}{\lambda_0^2}\right] + R_0 \frac{2^5\pi^4}{m^2}\left(\frac{\sigma_r}{\lambda_0}\right)^4 (\Delta\theta)^2. \tag{4.16}$$

Equation (4.16) contains two statistical surface parameters, namely σ_r and m.

In a similar way, Carniglia derived an expression for the specular transmittance of light that traverses a slightly rough interface with a Gaussian interface roughness [98]:

$$T_{\text{spec}}(\lambda_0) = T_0 \cdot \exp\left[-\frac{(2\pi\sigma_r)^2}{\lambda_0^2}(n_1\cos\psi_1 - n_2\cos\psi_2)^2\right]. \tag{4.17}$$

T_0 is the transmittance of a perfectly flat interface surrounded by the same two media, n_1 and n_2 are the refractive indices of these media, and ψ_1 and ψ_2 are the angles of incidence and refraction, respectively.

Zeman *et al*. assumed that the total reflectance and transmittance of a rough surface are equivalent to the reflectance and transmittance of a perfectly flat surface of the same material [99],

$$T_{\text{tot}}(\lambda_0) \equiv T_0(\lambda_0) \qquad \text{and} \qquad R_{\text{tot}}(\lambda_0) \equiv R_0(\lambda_0). \tag{4.18}$$

Therefore they could calculate the diffuse reflectance and transmittance with

$$T_{\text{dif}}(\lambda_0) = T_0(\lambda_0) - T_{\text{spec}}(\lambda_0), \tag{4.19a}$$

$$R_{\text{dif}}(\lambda_0) = R_0(\lambda_0) - R_{\text{spec}}(\lambda_0) \tag{4.19b}$$

and did not need to use Eq. (4.15). Their model thus contains only one statistical parameter, σ_r. Applying Eq. (4.17) to Eq. (4.19a) and Eq. (4.14) to Eq. (4.19b) and

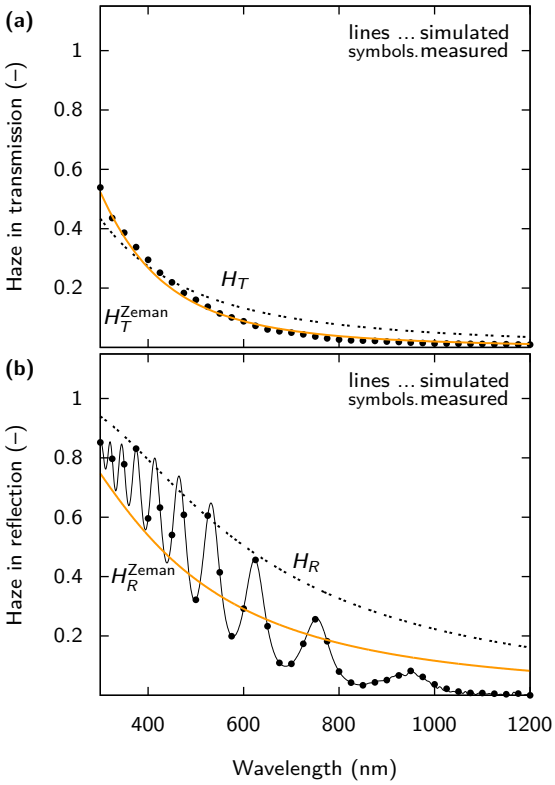

Figure 4.1.: Haze in (a) transmission and (b) reflection of SnO_2:F ($\sigma_r \approx 40$ nm). The black dashed lines were calculated with Eqs. (4.20a) and (4.20b), respectively. The full orange lines were calculated with Eqs. (4.21a) and (4.21b), respectively, with the correction factor $C_T = 0.6$ and $C_R = 0.7$. The points show measured values.

dividing by T_0 and R_0, respectively, leads to expressions for the haze parameters in transmission and reflection:

$$H_T(\lambda_0) = 1 - \exp\left[-\frac{(2\pi\sigma_r)^2}{\lambda_0^2}(n_1\cos\psi_1 - n_2\cos\psi_2)^2\right]. \tag{4.20a}$$

$$H_R(\lambda_0) = 1 - \exp\left[-\frac{(4\pi\sigma_r)^2}{\lambda_0^2}\right], \tag{4.20b}$$

With Eqs. (4.20a) and (4.20b), Zeman *et al.* did not obtain good agreement between measured and calculated data. The main reason for this might be that the surface roughness of the investigated surfaces was not Gaussian. However, they could obtain good agreement between measured and calculated haze values at normal incidence with

$$H_T^{\text{Zeman}}(\lambda_0) = 1 - \exp\left[-\frac{(4\pi C_T\sigma_r|n_1 - n_2|)^3}{\lambda_0^3}\right], \tag{4.21a}$$

$$H_R^{\text{Zeman}}(\lambda_0) = 1 - \exp\left[-\frac{(4\pi C_R\sigma_r n_1)^2}{\lambda_0^2}\right]. \tag{4.21b}$$

C_T and C_R are empirical constants that depend on the two media. We note that Zeman *et al.* introduced the refractive index n_1 in Eq. (4.21b), which makes it applicable also in media different from vacuum.

Figure 4.1 (a) shows H_T calculated with Eq. (4.20a) and Eq. (4.21a). In (b) H_R calculated with Eq. (4.20b) and Eq. (4.21b) is plotted. The used correction factors are $C_T = 0.6$ and $C_R = 0.7$. The calculated haze in reflection does not show the interference fringes, since the model only covers the physics at the interface but does not contain thin-film optics, which is not within the scope of this model.

Krč *et al*. extended Eqs. (4.21a) and (4.21b) to make them applicable at oblique incidence. Therefore they used the expressions that already were present in Eqs. (4.13) and (4.20a). They obtained

$$H_T^{\text{Krč}}(\lambda_0) = 1 - \exp\left\{-\frac{[2\pi\sigma_r\cdot c_T(\lambda_0)\cdot|n_1\cos\psi_1 - n_2\cos\psi_2|]^3}{\lambda_0^3}\right\}, \tag{4.22a}$$

$$H_R^{\text{Krč}}(\lambda_0) = 1 - \exp\left\{-\frac{[4\pi\sigma_r\cdot c_R(\lambda_0)\cdot n_1(\lambda_0)\cos\psi_1]^2}{\lambda_0^2}\right\}. \tag{4.22b}$$

While Eqs. (4.21a) and (4.21b) contain the empirical constants C_T and C_R, Eqs. (4.22a) and (4.22b) contain empirical, wavelength dependent *correction functions* $c_T(\lambda_0)$ and $c_R(\lambda_0)$. These functions are determined by fitting the model to measured haze values.

Equations (4.22a) and (4.22b) do not allow to calculate the haze parameters of arbitrary surface morphologies without knowing the correction functions $c_R(\lambda_0)$

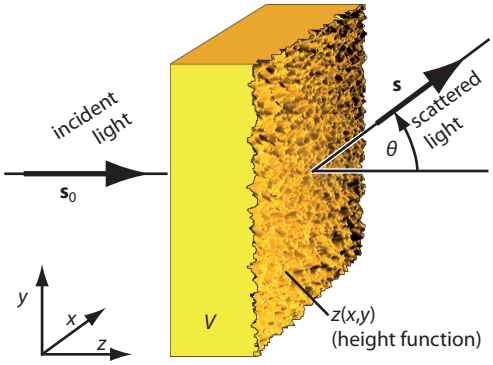

Figure 4.2.: Illustrating light that is scattered at a nano-textured interface.

and $c_T(\lambda_0)$. This is the biggest drawback of this model and makes the development of improved models desirable. We present such an improved model in the next section.

4.4. Calculating the AID with the first order Born approximation

In this section we present a model that predicts the diffuse part of the AID in transmission and uses the height function $z(x, y)$ as input. This model is based on the first order Born approximation and on the Fraunhofer scattering theory.[||] In difference to the haze model discussed in Section 4.3, this model also takes the lateral features of the rough surfaces into account. This can be achieved by using the height distribution $z(x, y)$ of the surface as input, instead of σ_r. We published the model presented in this section in late 2009 [100].

4.4.1. Theory

Let us assume a monochromatic incident plane wave $U^{\text{inc}} = \exp(ik_0\mathbf{s}_0\mathbf{r})$, propagating along the direction $\mathbf{s}_0$ and with the wavenumber $k_0 = 2\pi/\lambda_0$, as illustrated in Fig. 4.2. If U^{inc} is scattered by a rough surface of a thin film that covers the volume V, the scattered field U^{sca} far away from the film, *i.e.* if $k_0 r \to \infty$, can be written as

$$U^{\text{sca}}(r\mathbf{s}, \omega) = f(\mathbf{s}, \mathbf{s}_0; \omega)\tfrac{1}{r}e^{ik_0 r}, \tag{4.23}$$

[||] Both the first order Born approximation and the Fraunhofer scattering theory are derived in Ref. [94], Sections 13.2 and 8.3.3, respectively.

where the position is given by $r\mathbf{s} = \mathbf{r}$ and the unit vector $\mathbf{s}$ denotes the direction. The function f is called *scattering amplitude*. It is given by

$$f(\mathbf{s}, \mathbf{s}_0; \omega) = \iiint_V F(\mathbf{r}', \omega) U(\mathbf{r}', \omega) e^{-ik_0 \mathbf{s}\mathbf{r}'} \, \mathrm{d}^3 r', \tag{4.24}$$

where U is the field inside the volume. F is the *scattering potential* that is defined as

$$F(\mathbf{r}, \omega) = \tfrac{1}{4\pi} k_0^2 [n^2(\mathbf{r}, \omega) - 1]. \tag{4.25}$$

If we assume that light is only scattered once at the rough surface, we may write $U(\mathbf{r}, \omega) \approx U^{\mathrm{inc}}(\mathbf{r}, \omega) = \exp(ik_0 \mathbf{s}_0 \mathbf{r})$ if $\mathbf{r} \in V$. This assumption applied to Eq. (4.24) leads to the *first order Born approximation*,

$$f_1(\mathbf{s}, \mathbf{s}_0) = \iiint_V F(\mathbf{r}') e^{-i\mathbf{K}\mathbf{r}'} \, \mathrm{d}^3 r', \tag{4.26}$$

where $\mathbf{K} = k_0(\mathbf{s} - \mathbf{s}_0)$. The scattering amplitude f_1 therefore is given as the three-dimensional Fourier transform of the scattering potential F.

We assume n, and thus F, to be constant over the volume of the thin film, *i.e.* $F(\mathbf{r}, \omega) \equiv F(\omega)$. After integrating Eq. (4.26) over z, we find

$$f_1 = F \iint_A \mathcal{Z}(x, y) \exp[-i(K_x x + K_y y)] \mathrm{d}x \, \mathrm{d}y, \tag{4.27}$$

where A is along the rough surface of the thin film and

$$\mathcal{Z}(x, y) = \tfrac{1}{iK_z} \left\{ 1 - \exp[-iK_z z(x, y)] \right\}. \tag{4.28}$$

We note that $\mathcal{Z}$ contains the height function $z(x, y)$ that is the input parameter for our model.

To calculate K_z we recall that the light hits the obstacle along the z-axis and $\mathbf{s}_0$ thus only has a z-component of $s_{0,z} = 1$. Due to the unity of $\mathbf{s}$ we therefore obtain

$$K_z = k_0 \left(\sqrt{1 - s_x^2 - s_y^2} - 1 \right). \tag{4.29}$$

If we assumed $\mathcal{Z} \equiv 1/ik_0$ in Eq. (4.27), we would obtain, up to a constant, the Fraunhofer equation for scattering at an opening A.

The scattering angles θ, as in Fig. 4.2, are given by

$$\sin\theta = \tfrac{1}{k_0} \sqrt{K_x^2 + K_y^2}. \tag{4.30}$$

$\theta = 0^\circ$ corresponds to the direction of the incoming light. The Fourier components with $K_x^2 + K_y^2 > k_0^2$ correspond to the evanescent field of the scattered light that is not observed in the far field region.

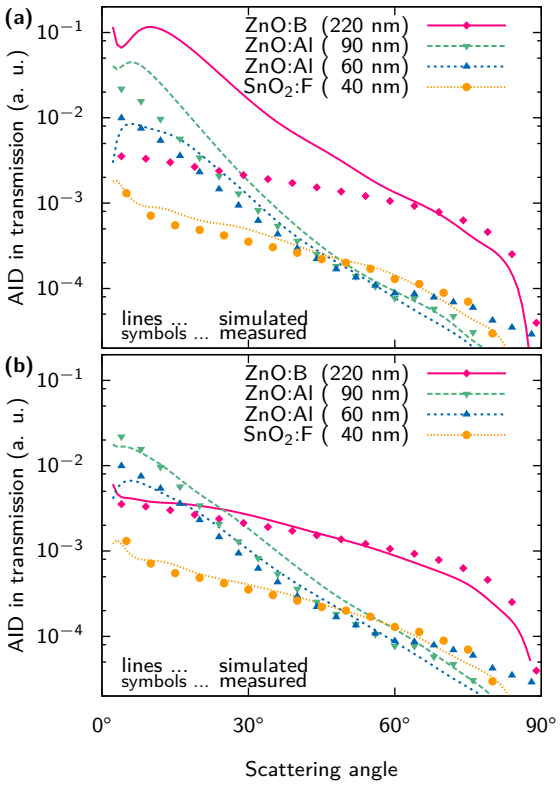

Figure 4.3.: The angular intensity distribution $\mathrm{AID}_T(\theta, \lambda_0)$ at $\lambda_0 = 600$ nm for four different TCO materials. The lines show the values that were calculated according to Eq. (4.31), where (a) $\mathcal{Z}$ from Eq. (4.28) was applied and (b) $\mathcal{Z}^{(\mathrm{II})}$ from Eq. (4.32) was used.

Since we are interested in the normalised intensity of the scattered light, the phase $\exp(ik_0 r)$ in Eq. (4.23) may be neglected. To match the calculated with the measured normalised values, we introduce the factor A_{opt}/A, where the area A_{opt} is dependent on the optical measurement system. By taking Lambert's cosine law into account we thus obtain for the angular intensity distribution of the scattered light

$$\mathrm{AID}(\lambda_0, \theta) = \frac{A_{\mathrm{opt}}}{A} \cos\theta \left| \frac{F}{r} \iint_A \mathcal{Z}(x,y) e^{-i(K_x x + K_y y)} \mathrm{d}x\, \mathrm{d}y \right|^2 . \tag{4.31}$$

4.4.2. Experimental evaluation

We evaluated the model on the SnO_2:F sample, the ZnO:B sample and the two ZnO:Al samples with broad craters presented in Fig. 3.4 (a)–(d). Figure 4.3 (a) shows measured and simulated AID_T of four TCO samples at $\lambda_0 = 600$ nm. The calculated curves were smoothened as explained in Appendix B. In this first approximation we assumed the refractive index of the TCO to be $n \equiv 2$. Good agreement is achieved for SnO_2:F ($\sigma_r \approx 40$ nm) and for ZnO:Al ($\sigma_r \approx 60$ nm). However, for ZnO:Al ($\sigma_r \approx 90$ nm) and ZnO:B ($\sigma_r \approx 220$ nm) large deviations between the measured and calculated intensities are observed. This is because the first order Born approximation only works for samples with a moderate rms roughness [101]. If σ_r is small compared to the wavelength, *i.e.* if the condition $k_0\sigma_r \ll 1$ is fulfilled, we can approximate $\mathcal{Z}$ from Eq. (4.28) with $\mathcal{Z}^{(\mathrm{I})} = z(x,y)$, which allows us to evaluate Eq. (4.31) with fast Fourier transform algorithms [102, 103]. The application of $\mathcal{Z}^{(\mathrm{I})}$ led to results similar to those already shown in Fig. 4.3 (a).

We found that we obtain better matching between measured and calculated intensities for large values of σ_r, when we modify Eq. (4.31) by replacing $\mathcal{Z}$ from Eq. (4.28) with

$$\mathcal{Z}^{(\mathrm{II})}(x,y) = \tfrac{1}{ik_0}\left\{1 - \exp[-ik_0 z(x,y)]\right\}. \tag{4.32}$$

This equation can be interpreted as *modified Fraunhofer diffraction*.** The phase shift $\exp[-ik_0 z(x,y)]$ in Eq. (4.32) contains the surface data. Since in Eq. (4.32) K_z is replaced by k_0, fast Fourier transform algorithms can be used to evaluate (4.31). Results are shown in Fig. 4.3 (b). While for SnO_2:F and ZnO:Al (60 nm) we hardly observe any difference between Fig. 4.3 (a) and (b), the measured and calculated intensities for ZnO:Al (90 nm) and ZnO match much better using the modified Fraunhofer scattering approach.

Figure 4.4 shows how the model extended with the modified Fraunhofer approach predicts wavelength-dependent changes of the AID. In general, the trend that the AID decreases with increasing wavelength is predicted correctly. We, however, observe some differences, mainly for large scattering angles. The changes in the shape of the AID are mainly due to the changing k in Eq. (4.30), while the changes in the absolute intensity are due to the changes in the scattering potential defined in Eq. (4.25).

4.5. Attempts on extending the AID model to reflection

In order to determine the AID in reflection, we have to modify Eq. (4.31), especially the phase term $\mathcal{Z}$. Two different approaches are possible:

**Fraunhofer diffraction is explained in detail in Section 5.2.

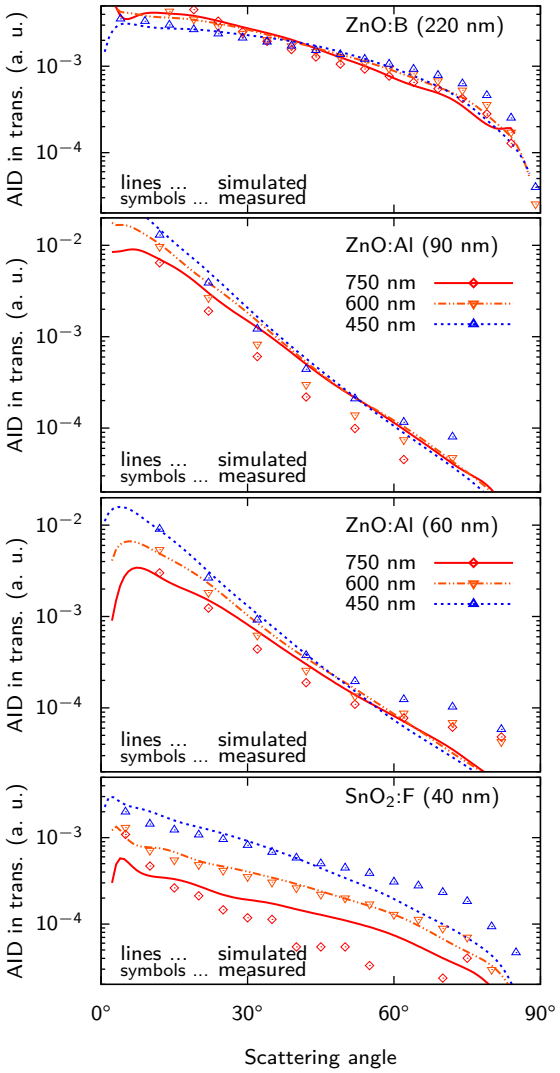

Figure 4.4.: The $\mathrm{AID}(\theta, \lambda_0)$ at three different wavelengths, shown for the four samples. The lines show the values, calculated according to (4.31), where $\mathcal{Z}^{(\mathrm{II})}$ from (4.32) was applied.

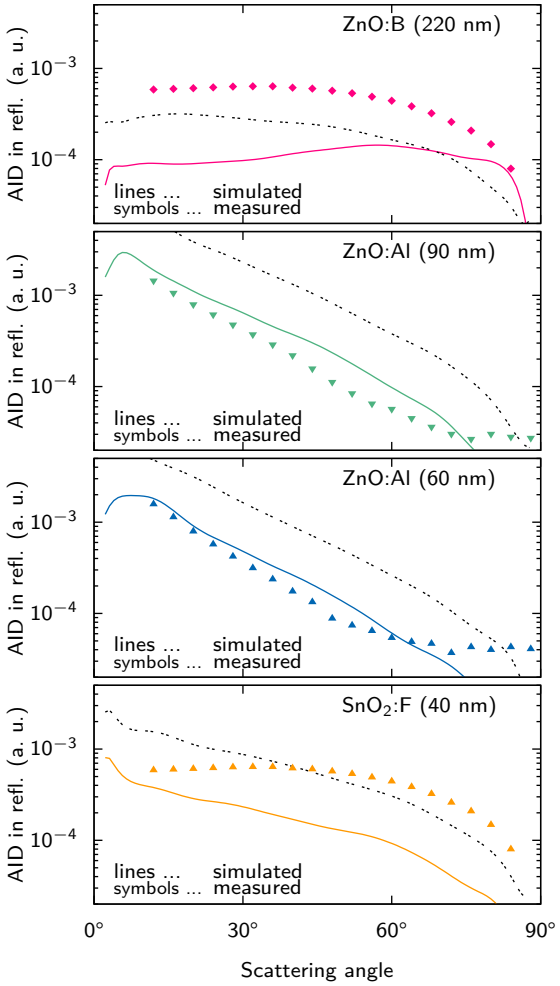

Figure 4.5.: The AID in reflection, calculated with the two approaches discussed in Section 4.5. The full coloured lines show calculations with $K_z = k_0 \left(-\sqrt{1 - s_x^2 - s_y^2} - 1\right)$. The dashed black lines show the calculations with $\mathcal{Z}^{\mathrm{III}}$ [Eq. (4.35)].

From the *pure* first order Born approximation and the relation $\mathbf{K} = k_0(\mathbf{s} - \mathbf{s_0})$ we derive for K_z

$$K_z = k_0 \left(\pm \sqrt{1 - s_x^2 - s_y^2} - 1 \right), \tag{4.33}$$

where $+$ denotes that the light is scattered forward ($s_z > 0$) and $-$ denotes that light is scattered backward ($s_z < 0$).

For the second approach we reconsider Eq. (4.32) again,

$$\mathcal{Z}^{(\mathrm{II})}(x,y) = \tfrac{1}{ik_0} \left\{ 1 - \exp[-ikz(x,y)] \right\}, \tag{4.34}$$

which, as already mentioned, can be interpreted as modified Fraunhofer scattering. In a somewhat simplistic view, $\exp[-ik_0 z(x,y)]$ can be interpreted as the phase corresponding to the profile height $z(x,y)$. For reflection the phase difference has to be taken twice. We therefore obtain

$$\mathcal{Z}^{(\mathrm{III})}(x,y) = \tfrac{1}{ik_0} \left\{ 1 - \exp[-2ik_0 z(x,y)] \right\}. \tag{4.35}$$

Figure 4.5 shows the calculated and measured AID_R. We measured the AID_R from the rough TCO such that the light can travel to the detector directly after it is scattered at the interface. We observe that the shapes of the simulated curves are similar, except for the very rough ZnO:B. However, there is is a constant offset between the two. Further, the absolute agreement between the simulations and the measurements is very bad. The reason for this offset is that the model in its current formulation does not ensure energy conservation; this problem is solved in Chapter 5.

4.6. Conclusion

In this chapter we reviewed the foundations of the scalar scattering theory. We further discussed a semi-empirical model that was developed in the first decade of this century to determine the haze of nano-textured interfaces. After that we showed that the first order Born approximation can be used to calculate the AID_T of nano-textured TCO-air interfaces. With this approach we obtained very good agreement between the measured and calculated AID_T at TCO-air interfaces for roughnesses up to about 60 nm. However, we needed a somewhat empirical modification based on the Fraunhofer theory to obtain also good agreement for samples with larger roughness. Attempts to extend the model to reflection lead to reasonable predictions for the shape of the AID_R, but failed in predicting the absolute strength of the AID_R. Further it is unclear how the model for AID_T can be extended to interfaces between other materials than TCOs and air. A major reformulation of the model is therefore needed to make it applicable for both transmission *and* reflection. In the next chapter we discuss what such a reformulation can look like.

Numquam ponenda est pluralitas sine necessitate.*

William of Ockham

5 A full scattering model for nano-textured interfaces

5.1. Introduction

In the last chapter we discussed how the scalar scattering theory, especially the first order Born approximation, can be used to calculate the AID. This approach led to good predictions for the AID_T, however, extending the model to reflection was problematic. Further, it was not clear how that model can be extended to interfaces different from TCO-air interfaces. Shortly after the publication of the model in late 2009 [100] two other models were presented that also calculated the AID_T [65–67]. All three models have in common that they facilitate Fourier transforms to relate the scattering object to the scattered field. They all perform well in predicting the AID_T of TCO-air interfaces. To evaluate the different approaches at TCO-silicon interfaces, we collaborated with Schulte *et al.* [104].

In this chapter we present a scattering model that allows estimating far-field scattering properties in both transmission and reflection for nano-textured interfaces between TCOs and different materials. To develop this model we condensed the findings from the three other models. This model is based on the Fraunhofer diffraction integral. After discussing the theoretical background of this integral in Section 5.2, we formulate the model in Sections 5.3 and 5.4. We then evaluate the model for TCO-air interfaces in Section 5.5. In Section 5.6 we investigate how the different approaches predict the AID_T at TCO-silicon interfaces. Finally, in Section 5.7 we evaluate how the model can predict the AID_R

*Plurality must never be posited without necessity.

at interfaces between TCOs and different materials. The content of this chapter except Sections 5.2 and 5.6 was published in Ref. [105]. The content of Section 5.6 was published in Refs. [70, 71]. In Section 5.2 we follow Ref. [94], Chapter 8.

5.2. The Fraunhofer diffraction integral

In the seventeenth century, Christaan Huygens postulated that every point of a wave-front may be considered as a centre of a secondary disturbance which gives rise to spherical wavelets. The wave-front at any later instant may then be regarded as envelope of these wavelets. In the early nineteenth century Augustin-Jean Fresnel supplemented this principle by postulating that the secondary spherical wavelets interfere mutually. This supplement allowed Fresnel to explain diffraction phenomena. The combination of the principles above is called the *Huygens-Fresnel principle*. In the late nineteenth century, Gustav Kirchhoff managed to put the Huygens-Fresnel principle on a sound mathematical base [106].

Let $V(x,y,z;t)$ be a scalar wave *in vacuo*. If V is strictly monochromatic, it can be separated in a factor only dependent on the space coordinates (x,y,z) and a factor $\exp(-i\omega t)$,

$$V(x,y,z;t) = U(x,y,z)e^{-i\omega t}. \tag{5.1}$$

The factor $U(x,y,z)$ satisfies the time-independent wave equation

$$(\nabla^2 + k_0^2)U = 0, \tag{5.2}$$

where $k_0 = \omega/c_0$. Kirchhoff showed that the field $U(P)$ at a point P inside a closed surface S is only determined by the value of the field U on the surface and its derivative along the inward normal $\partial U/\partial n$ at the surface,

$$U(P) = \frac{1}{4\pi} \oiint_S \left[U \frac{\partial}{\partial n} \left(\frac{e^{ik_0 s}}{s} \right) - \frac{e^{ik_0 s}}{s} \frac{\partial U}{\partial n} \right] \mathrm{d}S, \tag{5.3}$$

where S denotes the distance from the point P^*. This integral is one form of the *integral theorem of Helmholtz and Kirchhoff*.

To handle the diffraction of light at an aperture $\mathcal{A}$, we have to rewrite Eq. (5.3),

$$U(P) = \frac{1}{4\pi} \left[\iint_{\mathcal{A}} + \iint_{\mathcal{B}} + \iint_{\mathcal{C}} \right] \left\{ U \frac{\partial}{\partial n} \left(\frac{e^{ik_0 s}}{s} \right) - \frac{e^{ik_0 s}}{s} \frac{\partial U}{\partial n} \right\} \mathrm{d}S, \tag{5.4}$$

with the surfaces $\mathcal{A}$, $\mathcal{B}$ and $\mathcal{C}$ as depicted in Fig. 5.1. Kirchhoff now assumed that the field and its derivative at $\mathcal{A}$ are not disturbed by the screen and that both the

*In this section, P denotes a point and must not be confused with the power as used in Section 3.1.

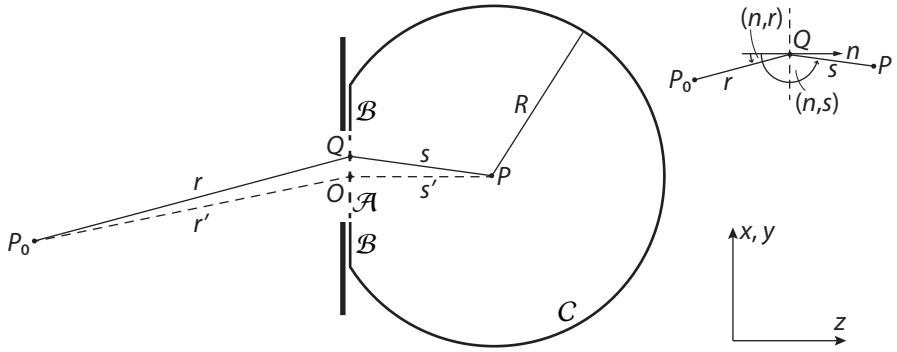

Figure 5.1.: Illustrating the derivation of the Fraunhofer diffraction formula. The coordinates of the point Q in the scattering aperture are denoted with (ξ, η).

field and its derivative vanish at $\mathcal{B}$, *i.e.* at the non-illuminated side of the screen. The field and its derivative at $\mathcal{A}$ then are given by

$$U^{(i)} = \frac{Ae^{ik_0 r}}{r}, \qquad \text{and} \qquad \frac{\partial U^{(i)}}{\partial n} = \frac{Ae^{ik_0 r}}{r}\left[ik_0 - \frac{1}{r}\right]\cos(n,r). \tag{5.5}$$

When further assuming that the integral along $\mathcal{C}$ vanishes if the radius R is taken large enough, the *Fresnel-Kirchhoff diffraction equation* is obtained,

$$U(P) = -\frac{iA}{2\lambda}\iint_{\mathcal{A}} \frac{e^{ik_0(r+s)}}{rs}[\cos(n,r) - \cos(n,s)]\mathrm{d}S. \tag{5.6}$$

To derive the Fraunhofer diffraction integral, several assumptions are made: First it is assumed that the distances of P_0 and P from the screen are large compared to the dimensions of the screen such that the factor $[\cos(n,r) - \cos(n,s)]$ does not vary much over the aperture. Further, if O is any point in the aperture, the angles which the lines P_0O and PO make with the line P_0P are small. Then this factor can be replaced by $2\cos\delta$, where δ is the angle between P_0P and the normal to the screen. Finally, the factor $1/rs$ may be replaced by $1/r's'$. Then, Eq. (5.6) reduces to

$$U(P) \approx -\frac{iA}{\lambda}\frac{\cos\delta}{r's'}\iint_{\mathcal{A}} e^{ik_0(r+s)}\mathrm{d}S. \tag{5.7}$$

Now Cartesian coordinates are used. When (x_0, y_0, z_0) and (x, y, z) are the coordinates of P_0 and P, respectively, and (ξ, η) are the coordinates of a point Q inside the aperture,

$$r^2 = r'^2 - 2(x_0\xi + y_0\eta) + \xi^2 + \eta^2, \tag{5.8a}$$

$$s^2 = s'^2 - 2(x\xi + y\eta) + \xi^2 + \eta^2. \tag{5.8b}$$

Due to the assumption that the linear dimensions of the aperture are small compared to the distance of P_0 and P from the aperture, r and s can be expanded as power series in ξ/r', η/r', ξ/r, and η/r. Then, Eq. (5.7) can be written as

$$U(P) = -\frac{iA}{\lambda}\frac{\cos\delta}{r's'}\iint_{\mathcal{A}} e^{ik_0 f(\xi,\eta)}\mathrm{d}\xi\,\mathrm{d}\eta, \tag{5.9}$$

with

$$\begin{aligned} f(\xi,\eta) &= (l_0 - l)\xi + (m_0 - m)\eta \\ &\quad + \frac{1}{2}\left[\left(\frac{1}{r'} + \frac{1}{s'}\right)(\xi^2+\eta^2) - \frac{(l_0\xi + m_0\eta)^2}{r'} - \frac{(l\xi + m\eta)^2}{s'}\right] + \cdots, \end{aligned} \tag{5.10}$$

where the direction cosines $l_0 = -x_0/r'$, $l = x/s'$, $m_0 = -y_0/r'$, and $m = y/r'$ were used. If only the linear term is used, one speaks of *Fraunhofer diffraction*. When also the quadratic term is needed, one speaks of *Fresnel diffraction*. We will work with Fraunhofer diffraction for the remainder of this work. By combining the direction cosines into the quantities

$$p = l - l_0 \qquad \text{and} \qquad q = m - m_0, \tag{5.11}$$

the *Fraunhofer diffraction integral* is obtained,

$$U(p,q) = \iint G(\xi,\eta)e^{-ik_0(p\xi+q\eta)}\mathrm{d}\xi\,\mathrm{d}\eta. \tag{5.12}$$

The pupil function $G(\xi,\eta)$ takes a constant value inside the aperture $\mathcal{A}$ and vanishes elsewhere.

Let us now assume a screen parallel to the aperture that is defined by the plane $z = z_S$. Its coordinates are then given as (x_1, y_1, z_S). Let this screen be far away from the aperture. If the light reaches the aperture at normal incidence, *i.e.* $l_0 = m_0 = 0$, the coordinates (p,q) then are related to coordinates on the screen via $p = \tan(x_1/z_S)$ and $q = \tan(y_1/z_S)$. For small angles this can be approximated by $p = x_1/z_S$ and $q = y_1/z_S$. This approximation is called the *paraxial approximation*.

5.3. The model

We formulate the equations such that energy conservation is intrinsically ensured. We determine the scattering properties in a two-step process. First we determine the scattered field in a two-dimensional k-space. Secondly we relate this field to the angular intensity distribution and the haze. Our approach is strongly related to the Fraunhofer diffraction integral. However, there are important differences:

1. In the classical treatment of Fraunhofer integral a *paraxial* approximation is used making it less accurate for larger scattering angles. In the second

step of our model we circumvent the need for a paraxial approximation by relating the field in k-space to the AID rigorously. This is similar to the approach presented by Harvey *et al.* [107].

2. In classical diffraction theory light is diffracted at an aperture. Mathematically this is done by defining pupil functions G that take a constant value inside the aperture and vanish outside. In our model, we consider the area in which the interface morphology is known, as *aperture*. In difference to the classical case, our pupil functions are not constant inside the aperture, but contain a phase shift that depends on the height profile of the interface.

In detail, the field in k-space is given by the two-dimensional Fourier transform of the *pupil functions* G_T^B, G_T and G_R,

$$U_T(K_x, K_y) = \frac{1}{2\pi} \iint_{\mathbb{R}^2} G_T^{(B)}(x,y) e^{-i(K_x x + K_y y)} \mathrm{d}x\, \mathrm{d}y, \tag{5.13a}$$

$$U_R(K_x, K_y) = \frac{1}{2\pi} \iint_{\mathbb{R}^2} G_R(x,y) e^{-i(K_x x + K_y y)} \mathrm{d}x\, \mathrm{d}y. \tag{5.13b}$$

The subscripts T and R denote transmittance and reflectance, respectively. The superscript B denotes "Born-Fraunhofer" and refers to the *Born-Fraunhofer* approach discussed in Section 4.4. The k-space coordinates are related to the quantities in Eq. (5.12) via $K_x = k_0 p$ and $K_y = k_0 q$. Further we use the coordinates (x, y) instead of (ξ, η). The pupil functions are given by

$$G_T^B(x,y) = \sqrt{\frac{T}{A}} \exp[ik_0 z(x,y) n_2], \tag{5.14a}$$

$$G_T(x,y) = \sqrt{\frac{T}{A}} \exp[ik_0 z(x,y)(n_1 - n_2)], \tag{5.14b}$$

$$G_R(x,y) = \sqrt{\frac{R}{A}} \exp[ik_0 z(x,y) 2n_1], \tag{5.14c}$$

inside the aperture while outside the aperture $G_{T,R} \equiv 0$. The interface is formed between two materials with the refractive indices n_1 and n_2. The light is incident on the rough interface from the material with n_1. The morphology of the interface is contained in the height function $z(x, y)$. The constants $\sqrt{T/A}$ and $\sqrt{R/A}$ are chosen such that the total amount of light flowing through the aperture of area A is equal to the total transmittance T or the total reflectance R of the interface, respectively. Hence, T and R are input parameters of the scattering model. We note that G_R only contains n_1. This indicates that the shape of the AID_R is independent of n_2, while its strength is controlled by R. We will show below that this assumption is supported by measurements. The *Plancherel theorem*, a fundamen-

tal property of Fourier transforms, ensures energy conservation [108]:

$$\iint_{\mathbb{R}^2} |G_T|^2 \mathrm{d}x\,\mathrm{d}y = \iint_{\mathbb{R}^2} |U_T|^2 \mathrm{d}K_x\,\mathrm{d}K_y = T, \tag{5.15a}$$

$$\iint_{\mathbb{R}^2} |G_R|^2 \mathrm{d}x\,\mathrm{d}y = \iint_{\mathbb{R}^2} |U_R|^2 \mathrm{d}K_x\,\mathrm{d}K_y = R. \tag{5.15b}$$

Only the k-vectors inside a circle with radius $k_0 n_{2,1}$,

$$K_x^2 + K_y^2 < k_0^2 n_{2,1}^2, \tag{5.16}$$

correspond to transmitted (reflected) light, while k-vectors outside this circle correspond to evanescent waves. The subscripts 2 and 1 are used for transmission and reflection, respectively. Under the assumption that no energy transport takes place via the evanescent waves, Harvey *et al.* introduced a heuristic normalisation to ensure that the power transmitted (reflected) from inside this circle is equal to the incident power. In our model we follow this renormalization method. However, we point out that it would be desirable to formulate the model in a rigorous manner such that no heuristic normalisation is needed.

We perform the normalisation by multiplying the field $U_{T,R}$ inside the circle with the factor [107]

$$\kappa_{T,R} = \sqrt{\frac{\iint_{\mathbb{R}^2} |U_{T,R}|^2 \mathrm{d}K_x\,\mathrm{d}K_y}{\iint_{\bigcirc} |U_{T,R}|^2 \mathrm{d}K_x\,\mathrm{d}K_y}}, \tag{5.17}$$

while

$$U_{T,R}(K_x, K_y) \stackrel{!}{=} 0 \qquad \text{if} \qquad K_x^2 + K_y^2 > k_0^2 n_{2,1}^2, \tag{5.18}$$

i.e. the evanescent waves are suppressed. The symbol $\bigcirc$ denotes the set defined by $K_x^2 + K_y^2 \leq k_0^2 n_{2,1}^2$.

The intensity and hence the AID is related to $|U|^2$. As illustrated in Fig. 5.2, the AID is defined on a unit hemisphere with coordinates (θ, ϕ), while U lives on the flat k-space with coordinates (K_x, K_y). Instead of using the paraxial approximation we use the accurate coordinate transformation, in which the coordinates are related to each other via

$$K_x = k_0 n_{2,1} \sin\theta \cos\phi \qquad \text{and} \qquad K_y = k_0 n_{2,1} \sin\theta \sin\phi. \tag{5.19}$$

The AID then is given by

$$\mathrm{AID}_{T,R}(\theta, \phi) = k_0 n_{2,1} |U_{T,R}[K_x(\theta, \phi), K_y(\theta, \phi)]|^2 \cdot \cos\theta. \tag{5.20}$$

If the morphology of the nano-textured interface is *isotropic*, U is isotropic as well. This implies that, up to noise due to limited sampling size of the interface,

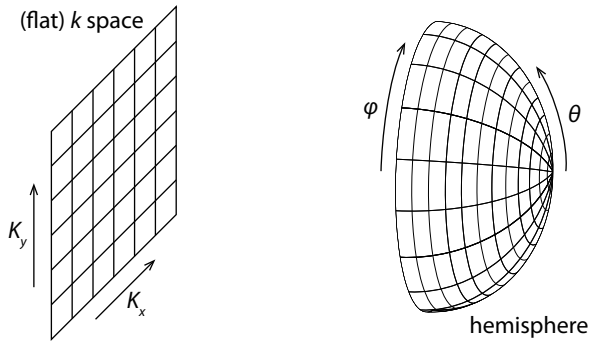

Figure 5.2.: Illustrating the flat k-space on which $U(K_x, K_y)$ lives and the hemisphere, on which the AID is defined.

the AID is independent of ϕ. We can therefore reduce the noise by averaging the AID over circles with constant θ,

$$\mathrm{AID}_{T,R}(\theta) = \frac{k_0 n_{2,1}}{2\pi \sin\theta} \oint_C |U_{T,R}|^2 \mathrm{d}s \cdot \cos\theta, \tag{5.21}$$

where $U_{T,R}$ takes the same arguments as in Eq. (5.20). The line integral is taken along the circle C that is defined by the condition $K_x^2 + K_y^2 = k_0^2 n_{2,1}^2 \sin^2\theta$. The cosine arises from the coordinate transformation between the flat k-space and the curved hemisphere on which the AID is defined.

In experiment the height function $z(x, y)$ is not available *everywhere* in the aperture, but only at a finite number of points where it is obtained for example with atomic force microscopy (AFM). Hence, we use discrete (fast) Fourier transforms instead of continuous Fourier transforms [102, 103]. The constants in the pupil functions from Eqs. (5.14a-5.14c) are then $\sqrt{T/N}$ and $\sqrt{R/N}$ instead of $\sqrt{T/A}$ and $\sqrt{R/A}$, where N is the number of data points. Further, the integrals have to be replaced by sums.

The haze in transmission (reflection) is defined as the ratio of the diffuse transmittance (reflectance) to the total transmittance (reflectance), $H_{T,R} = \Xi_{\mathrm{dif}}/\Xi_{\mathrm{tot}}$, where Ξ denotes either T or R. In the discrete case, where $z(x, y)$ is given as a discrete set of points, the haze can be estimated in a straightforward manner by

$$\begin{aligned} H_{T,R}(\lambda_0) &= \frac{\Xi_{\mathrm{dif}}(\lambda_0)}{\Xi_{\mathrm{tot}}(\lambda_0)} = \frac{\Xi_{\mathrm{tot}}(\lambda_0) - \Xi_{\mathrm{spec}}(\lambda_0)}{\Xi_{\mathrm{tot}}(\lambda_0)} \\ &= \frac{\sum\limits_{K_x^2+K_y^2 \le k_0^2 n_{2,1}^2} |U_{T,R}(K_x, K_y)|^2 - |U_{T,R}(0,0)|^2}{\sum\limits_{K_x^2+K_y^2 \le k_0^2 n_{2,1}^2} |U_{T,R}(K_x, K_y)|^2}, \end{aligned} \tag{5.22}$$

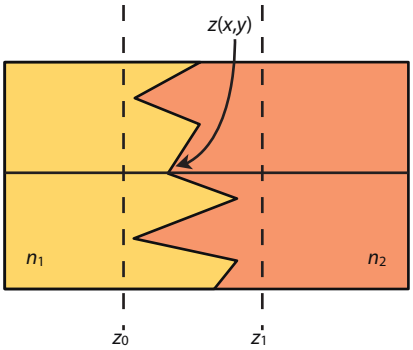

Figure 5.3.: Illustrating the phase light obtains at the nano-textured interphase.

as Dominé *et al.* demonstrated [65]. In difference to the AID, the haze is affected by neither the Harvey normalisation nor R or T. The wavelength dependent changes of the haze are mainly due to the changing wavenumber $k_0 = 2\pi/\lambda_0$. Thus, in this model the haze in general will decrease with increasing wavelength, given that the refractive index does not change too fast with the wavelength.

The technical realisation if the scattering model is discussed in Appendices C and D. How to choose AFM scans with size and resolution suitable as input for the model is discussed in Appendix E.

5.4. Discussion on the pupil functions

Before we proceed with the experimental evaluation of the model, we discuss briefly the different pupil functions that we introduced in Eqs. (5.14a-5.14c) as

$$G_T^B(x,y) = \sqrt{\frac{T}{A}}\exp[ik_0 z(x,y)n_2],$$
$$G_T(x,y) = \sqrt{\frac{T}{A}}\exp[ik_0 z(x,y)(n_1-n_2)],$$
$$G_R(x,y) = \sqrt{\frac{R}{A}}\exp[ik_0 z(x,y)2n_1].$$

The pupil function G_T^B is derived from the first order Born approximation that we discussed in Section 4.4. At first only scattering of objects *in vacuo* can be handled in that model. To calculate scattering parameters between arbitrary materials the surrounding vacuum has to be replaced with a material of refractive index n_2. This can be done by performing the transformations

$$n_1 \to n_1^{\text{eff}} = n_1/n_2 \qquad \text{and} \qquad k_0 \to k_{\text{eff}} = k_0 n_2. \tag{5.23}$$

Then the shape of the scattered field is determined by the pupil function

$$G_T^B(x,y) \propto \exp[ik_{\text{eff}}\, z(x,y)] = \exp[ik_0\, z(x,y) n_2]. \tag{5.24}$$

The strength of the scattered field is controlled by the so-called scattering potential, which vanishes if $n_1 \to n_2$. In G_T^B the (implicit) assumption is made that the phase obtained in the second medium is sufficient to predict the scattered field.

The pupil functions G_T and G_R are related to the phase β the light obtains when interacting with the nano-textured surface,

$$G(x,y) \propto \exp[i\beta(x,y)]. \tag{5.25}$$

For transmission, the phase the light obtains when travelling from z_0 to z_1, as illustrated in Fig. 5.3, is given by

$$\begin{aligned} \beta_T(x,y) &= k_0[n_1(z-z_0) + n_2(z_1-z)] \\ &= k_0[n_1-n_2]z(x,y) - k_0 n_1 z_0 + k_0 n_2 z_1. \end{aligned} \tag{5.26}$$

The second and the third terms are independent of the position (x,y) and will not contribute to the shape of the AID. Therefore we can neglect them. This pupil function was introduced by Dominé *et al.*, who developed a scattering model based on the Rayleigh-Sommerfeld diffraction integral [65].

For reflection, we assume that the light travels from z_0 to the interface and back. Hence,

$$\beta_R(x,y) = 2k_0 n_1 (z - z_0). \tag{5.27}$$

Again, we can neglect the position-independent term, here given by $2kn_1z_0$. Very recently, this pupil function also was used in a study by Bittkau *et al.* [109].

If the light is scattered at a TCO-air interface, and the refractive index of the TCO is $n_1 \equiv 2$, the pupil functions G_T and G_T^B are equivalent:

$$G_T^B(x,y) \propto \exp[ik_0 z(x,y)\cdot 1] \quad = \exp[ik_0 z(x,y)], \tag{5.28a}$$

$$G_T(x,y) \propto \exp[ik_0 z(x,y)(2-1)] = \exp[ik_0 z(x,y)]. \tag{5.28b}$$

However, they are very different when applied to TCO-silicon interfaces, which we will discuss in more detail in Section 5.6, where we look at transmission in a TCO-Si interface. But first, we evaluate the model for TCO-air interfaces in the next section.

5.5. Evaluating the models at TCO-air interfaces

We evaluated the model on the SnO_2:F sample, the ZnO:B sample and the two ZnO:Al samples with broad craters presented in Fig. 3.4 (a–d). Their statistical properties are summarised in Table 5.1. We approximated R and T by using the Fresnel equations for flat interfaces at normal incidence. While for transmission

Table 5.1.: The morphology, rms roughness σ_r and correlation length ℓ_c of the used TCO samples as obtained from AFM scans of 256×256 points over 20×20 µm^2. The values in brackets show values obtained from 5×5 µm^2 scans.

Material		**Morphology**	σ_r **(nm)**	ℓ_c **(nm)**
SnO_2:F	[75]	pyramidal	40 (37)	175 (160)
ZnO:Al	[61, 76]	crater-like	60	520
ZnO:Al		crater-like	90	625
ZnO:B	[60]	pyramidal	220	470

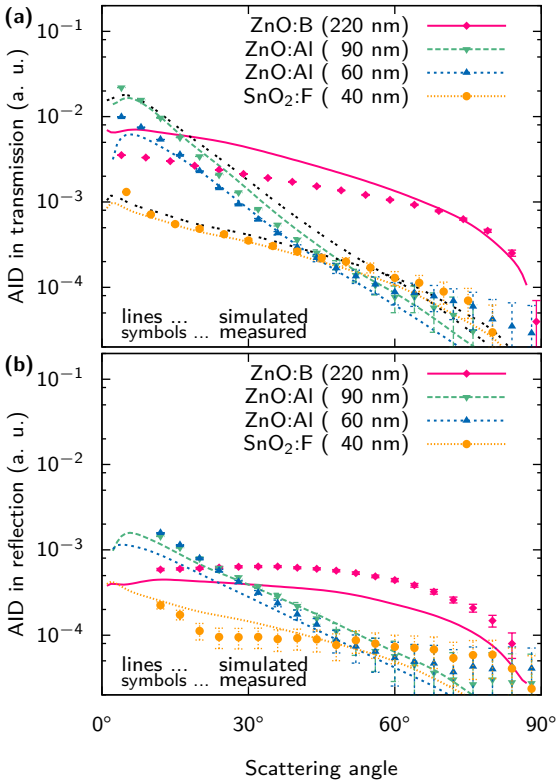

Figure 5.4.: Simulated and measured angular intensity distribution (AID) in (a) transmission and (b) reflection for four TCO-air interfaces at 600 nm. The coloured lines in (a) were calculated with G_T [Eq. (5.14b)], while the black lines were calculated with G_T^B [Eq. (5.14a)]. The measurement errors are determined according to Ref. [69].

the light was incident on the glass side, for reflection it was incident on the coated side. This was done to ensure that light reached the detector without traversing any other interfaces after being scattered.

Figure 5.4 shows the simulated and measured AID in transmission (a) and reflection (b). The simulated AIDs were smoothened, as explained in Appendix B. The coloured lines in (a) were calculated with G_T [Eq. (5.14b)], while the black lines were calculated with G_T^B [Eq. (5.14a)]. As discussed in Section 5.4, the two pupil functions are very similar for TCO-air interfaces. For better visibility, we showed the results for G_T^B for two samples only. Up the 60° we observe good agreement for SnO_2:F and ZnO:Al. For the AID for angles higher than 60°, the deviations become larger. However, also the measurement uncertainty becomes larger for these low intensities [69]. For ZnO:B the simulated AID_T overestimates the measured data, while the simulated AID_R underestimates the measured data. These deviations are due to the high roughness of the ZnO:B sample, letting R and T deviate significantly from the values expected from the Fresnel equations. While rough interfaces usually have an anti-reflective effect that for example can be modelled with effective medium approaches, the investigated ZnO:B sample behaves contrarily: As measurements with an integrating sphere show, it transmits less and reflects more than a ZnO:B sample with a flat surface. Despite this inaccuracy in the determination of R and T the shape of the AID is predicted well also for the very rough ZnO:B sample.

Figure 5.5 shows the simulated and measured AID_T for the four samples at three different wavelengths. In general the agreement between simulated and measured values is satisfying. For all four samples the wavelength-dependent changes are predicted well. In difference to Fig. 4.4, where the wavelength dependent changes were controlled by the scattering potential, as given in Eq. (4.25), here these changes are controlled by the the factor $\sqrt{T/A}$ in G_T and by Harvey's normalisation as in Eq. (5.17). In Fig. 5.5 the wavelength dependent changes for the two ZnO:Al samples are predicted better than in Fig. 4.4.

Figure 5.6 shows the simulated and measured haze in transmission (a) and reflection (b). Again, the coloured lines in (a) were calculated with G_T [Eq. (5.14b)], while the black lines were calculated with G_T^B [Eq. (5.14a)]. For the calculations with G_T, we observe good agreement between measurements and simulations. The calculations done with G_T^B deviate more from the measured values. The calculated haze in reflection does not show the interference fringes, since the model only covers the physics at the interface but does not contain thin-film optics, which is not within the scope of this model.

In Fig. 5.7 we study the effect of the input AFM file on the calculated AID. The AFM files were obtained at different spots of the sample. For a better comparison, we did not smooth AID_T here. We see that there are indeed differences. However, the trend is not influenced by the concrete input file, so one AFM measurement in prinicple is sufficient to analyse the scattering peroperties. For higher accuracy, one can calculate the AID for more AFM scans and then take the average.

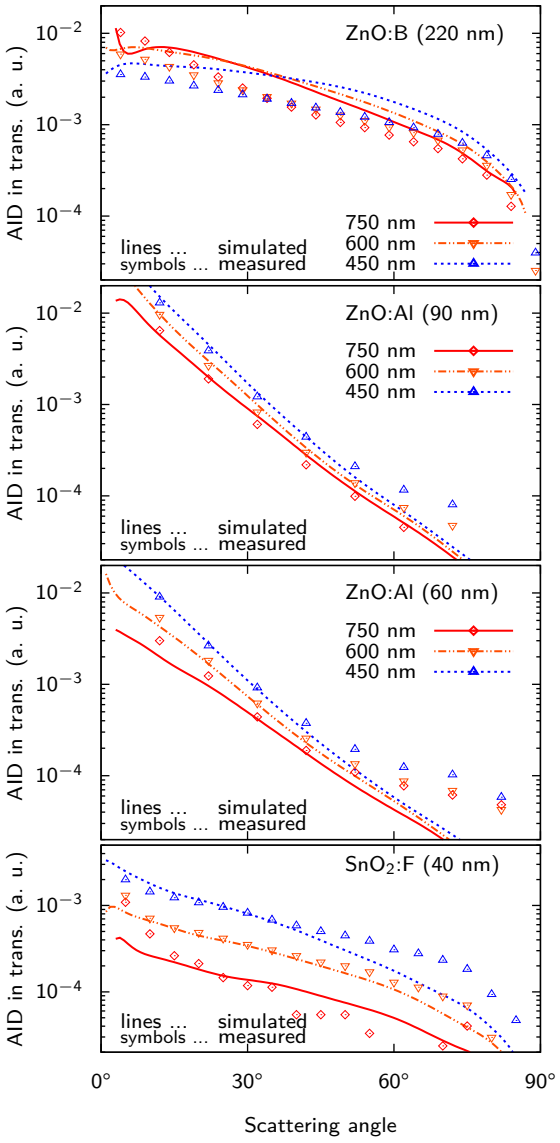

Figure 5.5.: Simulated and measured AID_T for four TCO-air interfaces at 450, 600 and 750 nm. The calculations were performed with the pupil function G_T as in Eq. (5.14b).

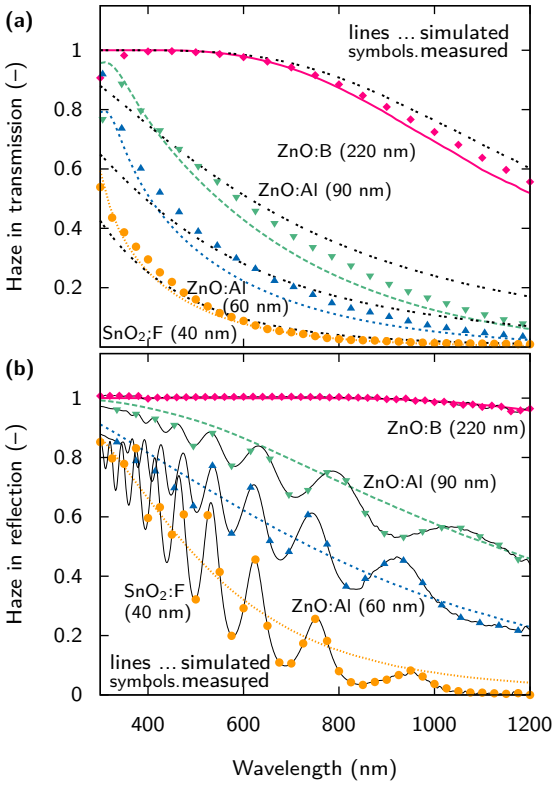

Figure 5.6.: Simulated and measured haze in (a) transmission and (b) reflection for four TCO-air interfaces with different morphologies. The coloured lines in (a) were calculated with G_T [Eq. (5.14b)], while the black lines were calculated with G_T^B [Eq. (5.14a)].

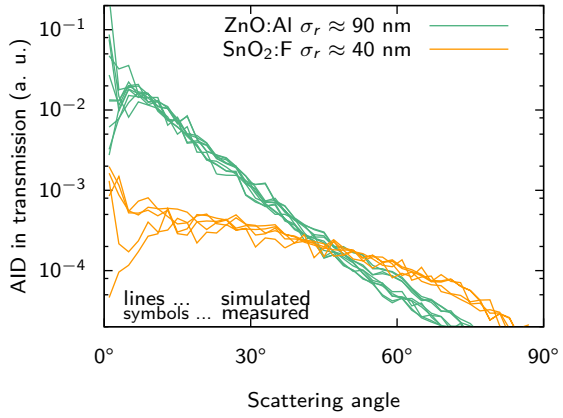

Figure 5.7.: AID_T of two nano-textures calculated for several different input AFM files.

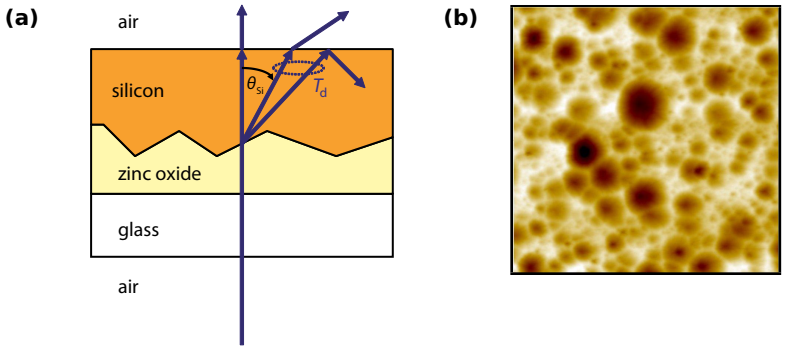

Figure 5.8.: (a) Sample geometry and (b) a 10×10 µm^2 AFM scans of the rough, crater-like ZnO interface with a height range of 610 nm.

5.6. Evaluating the models at TCO-silicon interfaces

We now evaluate how different scattering models predict the AID$_T$ at a TCO-Si interface. We already discussed measurements of the AID$_T$ at such interfaces in Section 3.6. The content of this section was published in Refs. [70, 104].

We cannot compare the calculated AID to the measured one directly: The scattering models predict the AID in an halfspace filled with an non-absorbing material with the (real part of the) refractive index of silicon, while the measurements reveal the AID inside the silicon layer. The measured AID therefore will be altered due to multiple reflections inside this layer. Therefore, we compare the modelled AID to the AID obtained with FDTD simulations. All the AIDs discussed in this section are normalised to allow a better comparison. The normalisation procedure is discussed in Appendix A.

5.6.1. Rigorous calculations with FDTD

We performed the rigorous calculations with the open source software Meep [110], an implementation of the FDTD method [91, 92]. The three-dimensional calculations take the refractive indices and extinction coefficients of the materials into account and were done on the layer stack shown in Fig. 5.8[†] (a). We implemented the textured interfaces using two different AFM scans, one of them is shown in Fig. 5.8 (b). The spatial resolution was 20 nm. We used metallic boundary conditions on the side, which might introduce reflections. Since these reflections do not change the scattering angle of the AID, they are not expected to disturb the result [111]. On the top and bottom we used perfectly matched layers. From the calculated light intensities slightly beneath the flat silicon-air interface,

[†]This figure is already shown as Fig. 3.18 and discussed here again to enhance readability.

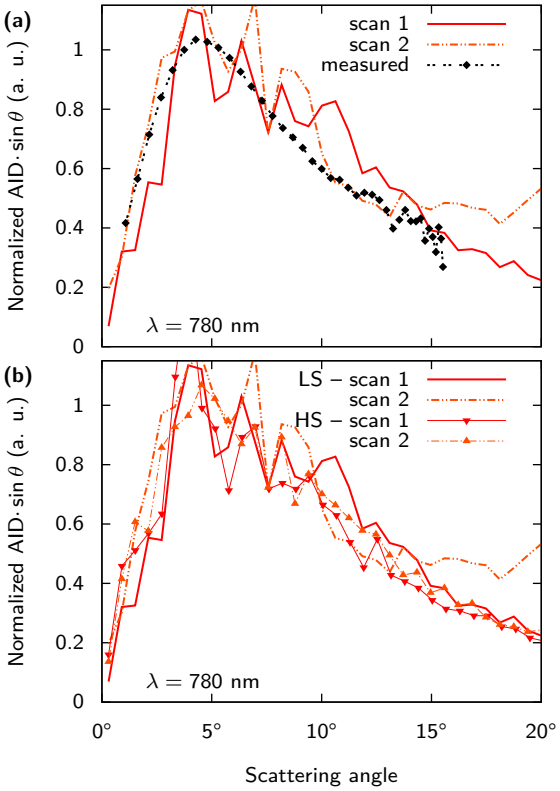

Figure 5.9.: (a) The AID· $\sin\theta$ inside the silicon layer obtained from FDTD calculations and measurements. (b) The AID· $\sin\theta$ inside the silicon layer stack (SL, thick lines) and in a half space filled with a silicon-like non-absorbing material (HS, thin dotted lines) as obtained from FDTD.

the AID in silicon is obtained by a fast Fourier transform. The FDTD results for both AFM topographies together with the measured AID are plotted in Fig. 5.9 (a). Even though the FDTD results show zigzag-like features due to the finite size of the calculation domain, a good agreement between calculations and measurements can be observed. As mentioned above, we have to calculate the AID in the half-space for evaluating the predictions of the approximate models. Figure 5.9 (b) shows FDTD calculations for the silicon layer and the half space filled with a non-absorbing material with the (real part of the) refractive index of silicon.

5.6.2. Overview of the evaluated models

In addition to the two models we evaluated already in Section 5.5 we tested also two other models at TCO-silicon interfaces. They also show good agreement for TCO-air interfaces:

In the *grating model*, formulated by Bittkau *et al.*, the scattering interface is decomposed into a superposition of gratings [66, 67]. The scattering angles of these gratings are determined by their reciprocal lattice constants. Like the other two models, the grating model is based on the scalar scattering theory.

In the *ray tracing* approach, developed by Schulte *et al.*, the scattering interface is decomposed into a collection of small facets [104]. Each of these facets refracts the incident light according to Snell's law. A ray is sent through each facet. The (unnormalised) AID at a scattering angle θ is then given by the number of rays that are scattered into a small interval around θ .

5.6.3. Evaluation of the results

Figures 5.10 (a) and (b) show the AID of the ZnO-silicon interface as obtained with the four approximate models for two different AFM scans. As mentioned before, the AID shown in the figure is obtained for a non-absorbing material with the refractive index of silicon. While the AID obtained from ray tracing is smooth, all the other approaches lead to zigzag-like results. One can observe some trends anyway. While the results obtained with G_T, the grating model and the FDTD calculation resemble each other, the results from the ray tracing approach and from G_T^B clearly deviate from the rest. The deviations of the ray tracing approach are not very surprising, since the features of the scattering interface are in the range of the wavelength but wave-optical effects are not considered in this approach. The reason for the large deviation of the results from G_T^B is the absence of the term $n_{\mathrm{TCO}} - n_{\mathrm{Si}}$, which is present in G_T. Therefore the pupil functions G_T and G_T^B deviate considerably from each other for TCO-silicon interfaces. The assumption in G_T^B that only the phase shift obtained in the second material is sufficient to describe the scattered field clearly does not work for TCO-silicon interfaces.

We can also analyse the validity of the different approaches by comparing the angles θ_{max} at which AID$\cdot \sin\theta$ takes its maximum. Table 5.2 shows the average

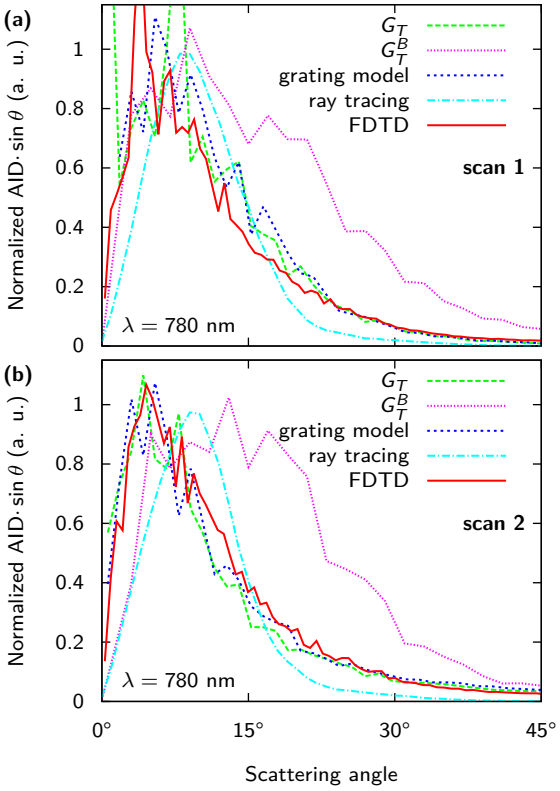

Figure 5.10.: The AID· sin θ in a half space filled with a non-absorbing silicon-like material obtained with four approximate model and FDTD calculations. The results shown in (a) and (b) were obtained with different AFM scans.

Table 5.2.: The angle θ_{max} at which AID· sin θ takes its maximum.

Approach	θ_{max}
(ARTA)	(4.2°)
FDTD	4.3°
G_T	5.4°
G_T^B	8.5°
grating model	3.9°
ray tracing approach	8.8°

$\theta_{\max}$ from scans 1 and 2 as they were obtained from the fitting procedure described in Appendix A. Similar to what we discussed above, $\theta_{\max}$ from the FDTD, G_T and the grating model are close to each other while the maximum angles from G_T^B and the ray tracing approach are much higher.

5.7. Reflection at interfaces between TCO and different materials

In this section evaluate the scattering model on predicting the AID_R at interfaces of TCO with different materials. To evaluate the AID_R at such interfaces, we prepared three samples each for the two ZnO:Al morphologies with broad craters shown in Figs. 3.4 (c) and (d). We left the first samples as they were, deposited one-µm thick a-Si:H layers on the second samples and deposited 300 nm of silver on the third samples.

In difference to the results on reflection presented in Fig. 5.4 (b) and 5.6 (b), here we had to measure from the glass side. Before the scattered light is measured, it therefore passes the ZnO:Al-glass and the glass-air interface. To simulate the measured AID, we thus had to take several effects into account similar to the effects discussed in Sections 3.6 and 5.6.

We first corrected for the transmission at the ZnO:Al-glass and the glass-air interface with the Fresnel equations. Secondly, we corrected the angles with Snell's law. Thirdly, we had to take into account that the detector does not detect a single ray but a pencil of rays that covers a certain solid angle. After passing through a (flat) interface, this pencil has a different solid opening angle. Its étendue, however, is conserved [90]. We thus obtain the factor $n_{\mathrm{TCO}}^{-2} \cdot \cos\theta_{vac} / \cos\theta_{\mathrm{TCO}}$. In Section 5.6 we did not compare the models directly to the measurements but compared them to results obtained with the FDTD method, because the models assume interfaces between two halfspaces. The measured values, however, also contain light that is reflected back into the sample at the Si-air interface and then reflected and scattered again at the rough ZnO:Al-Si interface, and higher orders. In principle, the same is true here, but the secondary interfaces in our experiment are much less reflective: While the reflectance of the Si-air interface investigated in Section 5.6 is 33.2% at 600 nm and normal incidence, the reflectance of the ZnO:Al-glass and glass-air interfaces is only 0.8% and 4.1%, respectively. It therefore is a good approximation to neglect these higher order effects, even though one then can expect larger deviations at higher angles, where the reflectivity is higher. Furthermore we can neglect secondary reflections from the Si-air interface of the second sample since at 600 nm only about 0.1% of light that is transmitted into the silicon will reach the ZnO:Al interface again after it is reflected at the Si-air interface.

Figure 5.11 shows the measured and simulated AID_R at ZnO:Al-air, ZnO:Al-Si and ZnO:Al-silver interfaces for the two different morphologies. For the mea-

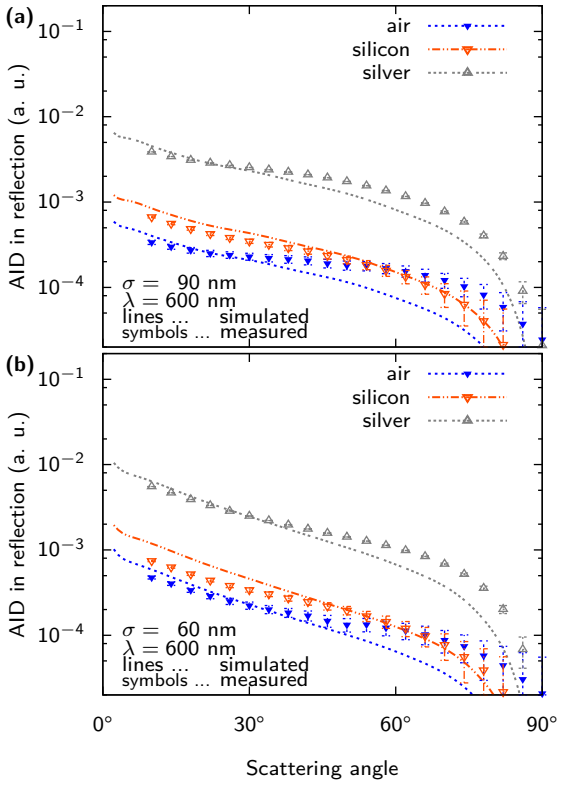

Figure 5.11.: Simulated and measured angular intensity distribution in reflection for three different ZnO:Al-material interfaces. The measurement deviations are determined according to Ref. [69].

sured values we used the average of *p*- and *s*-polarisation, since the light passes several interfaces at oblique incidence, before it reaches the detector. As we can see, the agreement in general is good and the model predicts the material-dependent changes of the AID_R correctly. The deviations at larger angles are indeed higher what can be expected from the discussion above. For the ZnO:Al-air interfaces the deviations at larger angles are larger than for the other interfaces. It is unclear whether this is a feature of the measured sample or a stray-light effect of the ARTA setup. In this evaluation we have discussed the AID_R of interfaces between TCO and different materials. The AID_R within Si, *e.g.* at Si-TCO or Si-metal interfaces has not been evaluated in this work and remains an important topic for future research.

5.8. Conclusions

In this chapter we presented a full model to calculate the angular intensity distribution (AID) of light that is scattered at nano-textured interfaces. In difference to the model presented in Section 4.4 the model presented in this chapter is applicable to interfaces between arbitrary materials. Further, we managed to extend the model also to reflection.

To prove the strength of the model, we evaluated it at three different cases. First, we looked at the predictions of the AID and haze in both transmission and reflection at TCO-air interfaces. Secondly, we evaluated how the model predicts the AID in transmission at TCO-silicon interfaces. Thirdly, we evaluated the model for predicting the AID in reflection at interfaces between TCO and air, silicon or silver.

For the AID in transmission we used two different pupil functions: When G_T^B is used, only the phase shift is taken into account, which light obtains in the material into which it is scattered. In G_T the phase shift light obtains when travelling through the whole interface is considered. These two cases lead to nearly the same results for the AID_T at TCO-air interfaces. For the prediction of the haze it is better when G_T is used. When calculating the AID_T at TCO-silicon interfaces, the results obtained from the two approaches deviate a lot. Using G_T leads to much better agreement with measured and FDTD results.

After having discussed the fundamentals of the scalar scattering theory in the last chapter and presenting a very flexible model in this chapter, we focus on the applicability of the scalar scattering theory at oblique incidence in the next chapter.

The game of science is, in principle, without end. He who decides one day that scientific statements do not call for any further test, and that they can be regarded as finally verified, retires from the game.

Sir Karl Raimund Popper

6 The scattering model at oblique incidence

6.1. Introduction

Up to now we only looked at scattering of light under normal incidence. Since solar cells operate under various incident angles of the light, it is important to know whether the scalar scattering theory can also be applied to predict scattering under oblique incidence correctly.

In Section 6.2 we investigate how the scattering model can be expanded to oblique incidence. We then evaluate the model by comparing its predictions to measured data in Section 6.3

6.2. Theory

To start this discussion we take another look at the Fraunhofer diffraction integral as formulated in Eq. (5.12),

$$U(p,q) = \iint G(\xi,\eta) e^{-ik_0(p\xi+q\eta)} \mathrm{d}\xi \, \mathrm{d}\eta.$$

By using the definition of p and q from Eq. (5.11) we find

$$U(l-l_0, m-m_0) = \iint G(\xi,\eta) e^{-ik_0[(l-l_0)\xi+(m-m_0)\eta)]} \mathrm{d}\xi \, \mathrm{d}\eta, \tag{6.1}$$

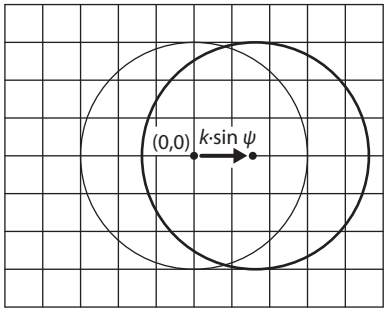

Figure 6.1.: The shift in k-space due to oblique incidence at an angle ψ.

where l_0 and m_0 are the direction cosines of the incident light, and l and m are the direction cosines of the outgoing light.

Oblique incidence therefore leads to a *shift* in k-space, as illustrated in Fig. 6.1. Due to the isotropy of the scattering sample we may assume without loss of generality that $m_0 = 0$. Then, following the definition of l_0 in Section 5.2, $l_0 = \sin\psi_1$, where ψ_1 is the angle of incidence. The shift in k-space thus is given by

$$k_{\text{shift}} = k_0 n_1 \sin\psi_1, \tag{6.2}$$

where k_0 is the wavenumber of the light *in vacuo* and n_1 is the refractive index of the incident medium. We note that because of Snell's law,

$$n_1 \sin\psi_1 = n_2 \sin\psi_2, \tag{6.3}$$

k_{shift} is invariant and thus the same in the two materials that form the interface.

Besides this shift, we also have to take a look at possible changes in the pupil function. For G_T [Eq. (5.14b)], the logical adaption would be

$$G_T^{\text{I}}(\psi_1; x, y) = \sqrt{\frac{T}{A}} \exp[i\beta_T(\psi_1; x, y)], \tag{6.4}$$

where the phase shift $\beta_T(\psi_1; x, y)$ is given by

$$\begin{aligned} \beta_T(\psi_1; x, y) &= k_0 \left[n_1 \frac{z - z_0}{\cos\psi_1} + n_2 \frac{z_1 - z}{\cos\psi_2} \right] \\ &= k_0 \left[\frac{n_1}{\cos\psi_1} - \frac{n_2}{\cos\psi_2} \right] z(x, y) - \frac{k_0 n_1 z_0}{\cos\psi_1} + \frac{k_0 n_2 z_1}{\cos\psi_2}. \end{aligned} \tag{6.5}$$

With this adaption we incorporate the idea that the path length of the light through the rough structure is increased by a factor $1/\cos$ due to the oblique incidence, as indicated in Fig. 6.2. Similar to Section 5.4, the second and third terms do not influence the shape of the AID and can be neglected.

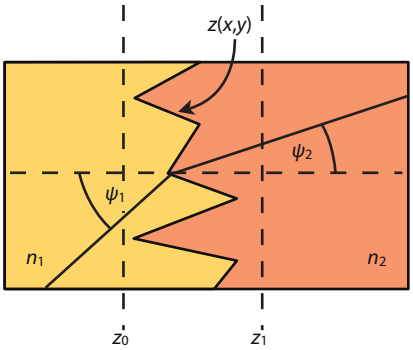

Figure 6.2.: Illustrating the phase light obtains when traveling through the interface at an oblique angle.

Similarly we obtain for G_R

$$G_R(\psi_1; x, y) = \sqrt{\frac{R}{A}} \exp\left[ik_0 \frac{z(x,y)}{\cos\psi_1} 2n_1\right], \tag{6.6}$$

where we assume that the incident angle ψ_1 is equal to the angle of the specular reflected light.

6.3. Experimental evaluation

Before we evaluate the scattering model for oblique incidence, we first take a look at measured data. Figure 6.3 shows the measured AID_T and AID_R for SnO_2:F at several incident angles in both p- and s-polarisation. In contrast to normal incidence, at oblique incidence a decoupling of the scattered fields of the two polarisations is visible. This effect is stronger for reflection. The AID in p-polarisation decays faster than in s-polarisation. With the scalar scattering theory, as formulated in Chapter 5, only a constant shift between the two polarisations due to the Fresnel equations can be explained. The decoupling in shape cannot be explained with the scalar scattering theory.

To compare the calculated to the measured AID, we thus take the average of the two measured polarisations,

$$\mathrm{AID}_T^{\mathrm{avg}} = \frac{1}{2}\left(\mathrm{AID}_T^p + \mathrm{AID}_T^s\right). \tag{6.7}$$

Figure 6.4 shows the simulated and measured AID_T for SnO_2:F at oblique incidence at different angles. In (a), the simulations were performed with the pupil function G_T^{I} from Eqs. (6.4) and (6.5). We first note that the peaks are indicated

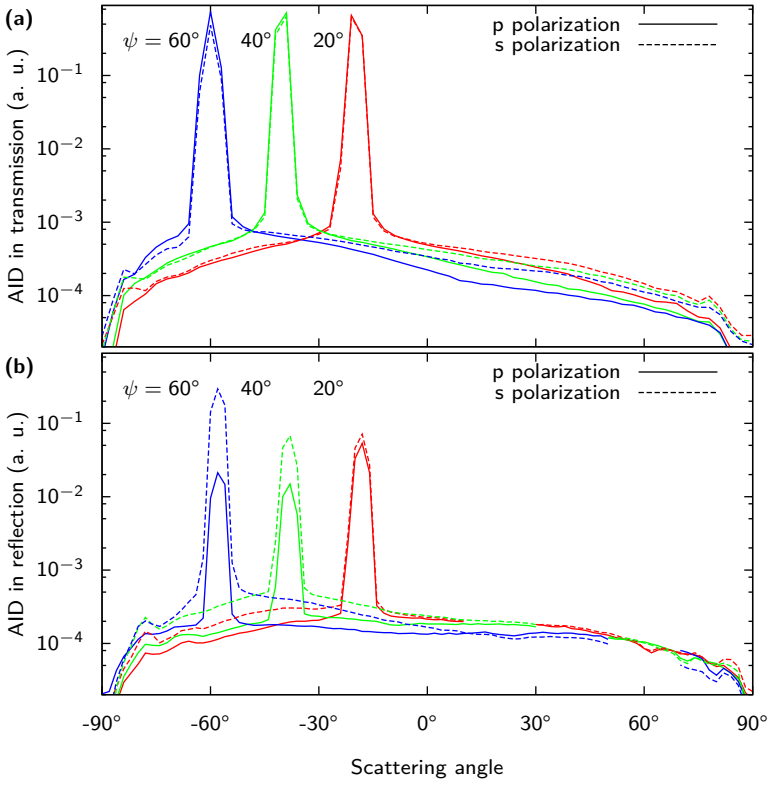

Figure 6.3.: The (a) AID_T and (b) AID_R of SnO_2:F ($\sigma_r \approx 40$ nm) under different incident angles for both *p*- and *s*-polarisation at 600 nm. In (b) at some angles no measurement data is shown because these angles are not accessible for the ARTA, as depicted in Fig. 3.8.

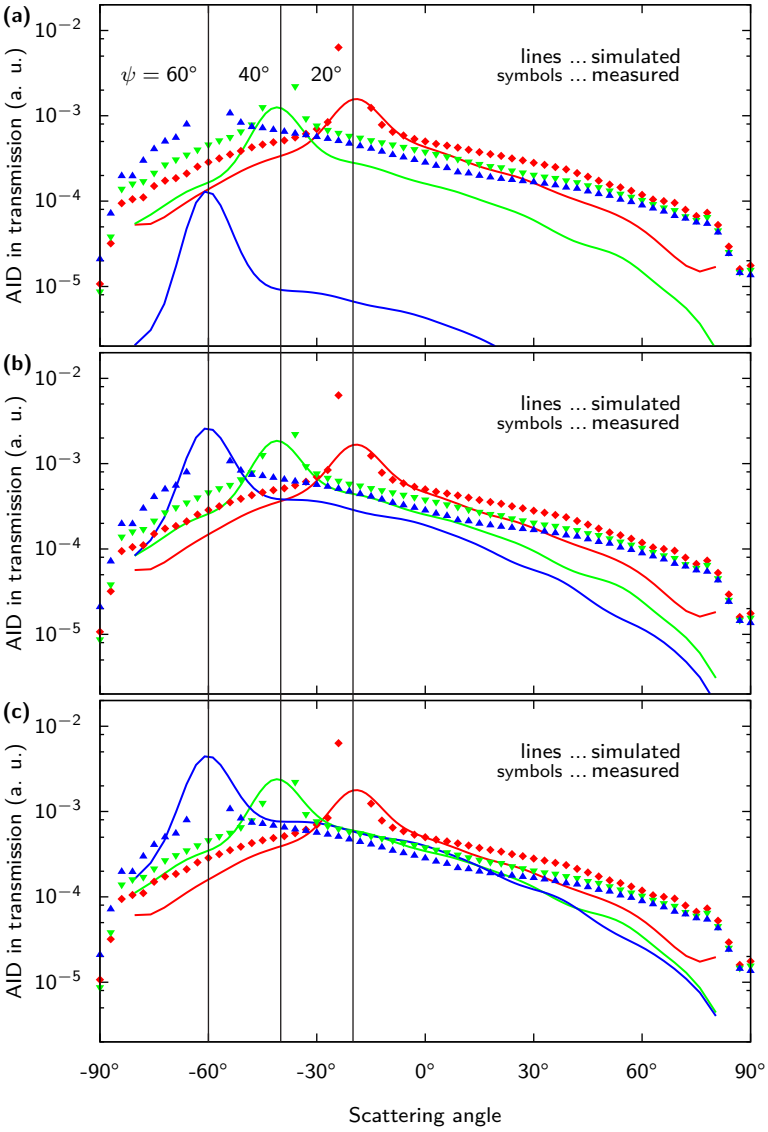

Figure 6.4.: Simulated and measured AID_T of SnO_2:F ($\sigma_r \approx 40$ nm) at oblique incidence at 600 nm. In the simulations the pupil function was calculated according to (a) Eq. (6.4), (b) Eq. (5.14b) and (c) Eq. (6.9).

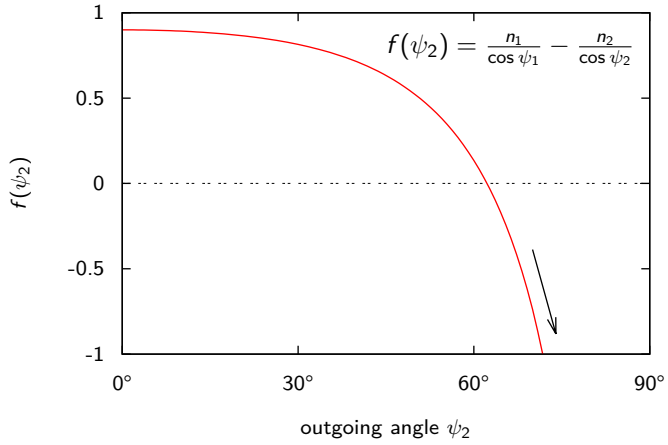

Figure 6.5.: The function $f(\psi_2)$ present in Eq. (6.5) plotted for $n_1 = 1.9$ and $n_2 = 1$.

at the right positions,* At 20°, also the intensity around the peak is close to the measured one, however further away from the peak the simulated AID decays much faster than the measured one. At 40° and mainly at 60° the simulated AID is much lower than the measured one.

To understand the underestimation at large angles, we take a closer look at the function

$$f(\psi_2) = \frac{n_1}{\cos\psi_1} - \frac{n_2}{\cos\psi_2}, \tag{6.8}$$

that is present in Eq. (6.5) and plotted in Fig. 6.5 for $n_1 = 1.9$ and $n_2 = 1$. We see that this function gets more negative with larger angles; at $f(60°) \approx 0.13$. Therefore the simulated AID is much too small.

In Fig. 6.4 (b) we tested how the simulations react on using the pupil function for normal incidence, Eq. (5.14b), for all angles. The results are closer to the measurements than in (a). However, also here, the AIDs for 40° and 60° are too low. This indicates that the interface that is "seen" by the light indeed seems rougher at larger incident angles. We therefore altered the pupil function empirically,

$$G_T^{\mathrm{II}}(\psi_1; x, y) = \sqrt{\frac{T}{A}} \exp\left[ik_0 z(x,y)(n_1 - n_2)\frac{2}{\cos\psi_1 + \cos\psi_2}\right]. \tag{6.9}$$

The idea of this alteration is that the increase is the average of the increase that would be expected in each of the materials separately. Figure 6.4 (c) shows that this assumption indeed leads to better agreement between simulated and measured results. The biggest problem is the bad agreement at larger angles.

Figure 6.6 shows the simulated and measured AID_R for different incident angles. Similar to transmission, also here the AID at large angles decays too fast.

*Due to the smoothing with Bezier splines (Appendix B) the peak is not shown at its full height.

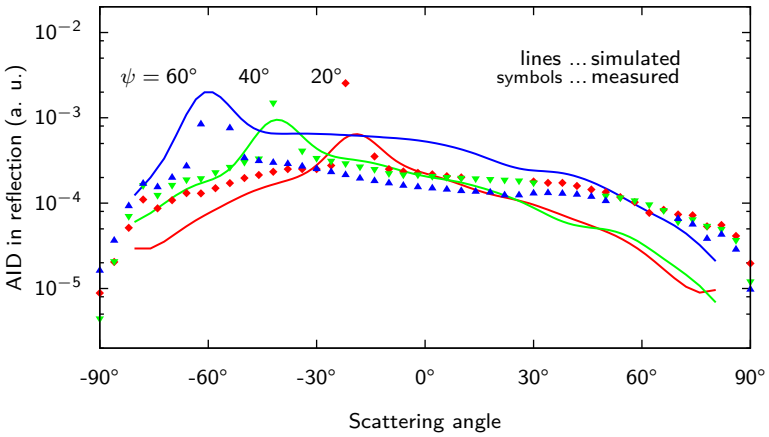

Figure 6.6.: Simulated and measured AID_R of SnO_2:F ($\sigma_r \approx 40$ nm) at oblique incidence at 600 nm. In the simulations the pupil function was calculated according to Eq. (6.6).

While the intensity level for 20° and 40° is close to the measured values, the intensities at 60° are estimated too high.

6.4. Conclusions

In this chapter we have discussed how the scattering model can be expanded to oblique incidence. While this is possible without much problems in theory, in practise number of problems arise:

- At oblique incidence, the light depolarises at interfaces between two materials. This effect gets more severe for larger incident angles.
- At large incident angles, the interface features might partially shade features laying behind them, which would make our approach invalid.

Despite these problems we could show that the scattering model is able to predict the peak angle and also the intensity level close to the peak. For future work it might be interesting to study how the scalar scattering model can be extended to a model based on the vector-theory of light. If such a model is based on Fourier transforms as well, it might be possible to combine the fast calculations of our scattering model with the enhanced accuracy of the vector theory of light. Recently, Haug *et al.* used plane wave expansions to calcuate reflection and scattering at textured metallic surfaces in *p*- and *s*-polarization [112]. For further reading on diffraction theory in the vector approach we refer to Nieto-Vesperinas [113]. As discussed in Eq. 5.17 and the preceding paragraph, we used a heuristic normalization introduced by Harvey *et al.* It might be important to study whether an improved model without such a normalisation leads to better agreement.

Computers are useless.
They can only give you answers.

Pablo Picasso

7 Simulating complete solar cells

7.1. Introduction

In this chapter we discuss how to combine the scattering model with the opto-electric ASA simulation tool that has been developed at the Delft University of Technology for more than 25 years [114–117]. We evaluate this combination by simulating and measuring the *J-V* characteristics, the external quantum efficiency and the reflectance of solar cells with different interface morphologies. Combining the scattering model with ASA is very valuable, since it allows us to study the effect of different nano-textured interfaces on the performance of solar cells. The chapter is structured as follows: In Section 7.2 we discuss the experimental solar cell series that was prepared for the validation of the simulations. In Section 7.3 we discuss opto-electric simulations of cells with different nano-textured interface morphologies and validate the obtained results by comparing them with measured data. The results presented in this chapter were published in Ref. [105].

7.2. Experimental solar cell series

The scattering model is developed in the far-field regime, *i.e.* it predicts the field at distances that are at least several wavelengths away from the scattering object. State-of-the-art thin-film silicon solar cells are deposited with an i-layer thickness between 250 and 300 nm. Taking the real part of the refractive index of amorphous silicon to be approximately 4, light with 600 nm wavelength *in vacuo* has a wavelength of about 150 nm inside silicon. Having the light being scattered at

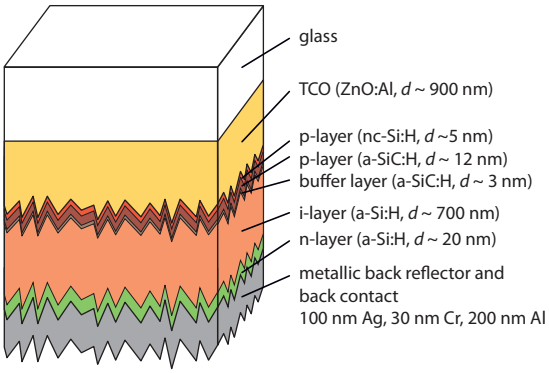

Figure 7.1.: Illustrating thin-film silicon solar cells as they were deposited for this contribution. The layer thickness is denoted by d. (Layer thicknesses not in scale.)

both sides of the i-layer, near field effects that are present at scales smaller than the wavelength might become important [118], making the use of the scattering model arguable. We therefore decided to prepare solar cells with an intrinsic layer thickness of approximately 700 nm. At this thickness the application of the far field approach is more justified.

Figure 7.1 illustrates the detailed structure of the prepared solar cells with the nominal layer thicknesses d. As TCO we used RF magnetron sputtered ZnO:Al, which was surface-textured by etching it in hydrochloric acid with 0.5% HCl mass fraction [61]. We varied the etching time between 0 s and 75 s with 15 s steps in between. To minimise the effect of changing TCO thickness on its transmittance and sheet resistance, we varied the deposition time and hence the initial TCO thickness. This was done in order to keep the average TCO thickness after etching approximately constant.

Onto the TCO we deposited a nanocrystalline hydrogenated silicon (nc-Si:H) p-layer, an amorphous hydrogenated silicon carbide (a-SiC:H) p-layer, an a-SiC:H buffer layer, an amorphous hydrogenated silicon (a-Si:H) i-layer, and an a-Si:H n-layer. Finally we deposited silver, chromium and aluminium layers on the back using a mask with square openings with 0.16 cm^2 area. The Ag layer acts as optical back reflector. Together with the Cr and the Al layers it forms the electric back contact. As last processing step, the solar cells were annealed for 30 minutes at 130°C. The solar cells were deposited onto stripes with 2×10 cm^2 area. Each stripe contained 30 solar cells.

The top panels of Fig. 7.2 show AFM scans of 5×5 μm^2 for the ZnO:Al after 15 s, 30 s and 45 s etching time. The morphology shows the typical crater like features of etched ZnO:Al; the rms roughness is 35 nm, 70 nm and 95 nm, respectively. The bottom panels show the back of p-i-n structures with an i-layer thickness of 700 nm that were deposited on the back of these ZnO:Al layers (see below). The

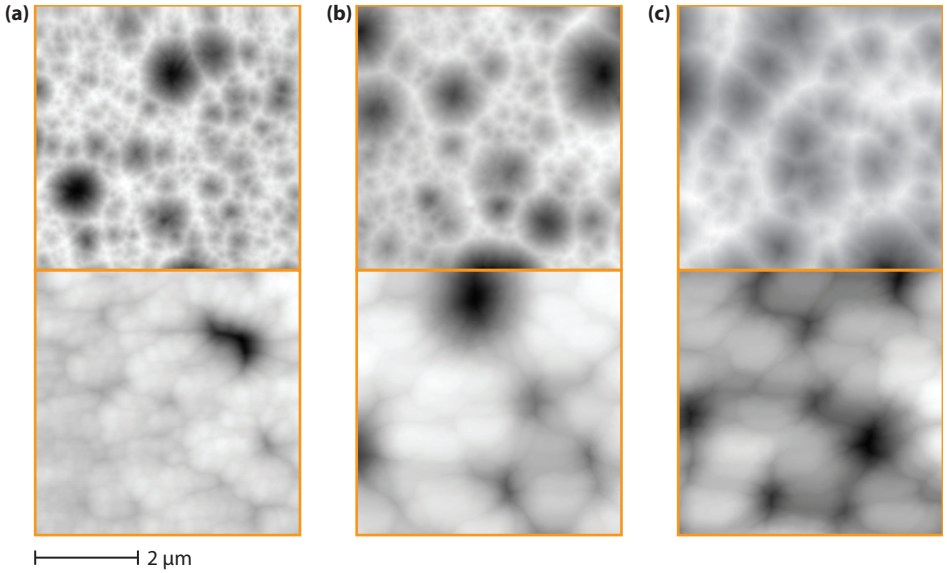

Figure 7.2.: Atomic force microscopy scans of ZnO:Al etched in HCl of 0.5% mass fraction (top) and of the back of p-i-n structures deposited on the ZnO:Al (bottom). The etch times were (a) 15 s, (b) 30 s and (c) 45 s. The scans consist of 256×256 points and are 5×5 µm^2 large.

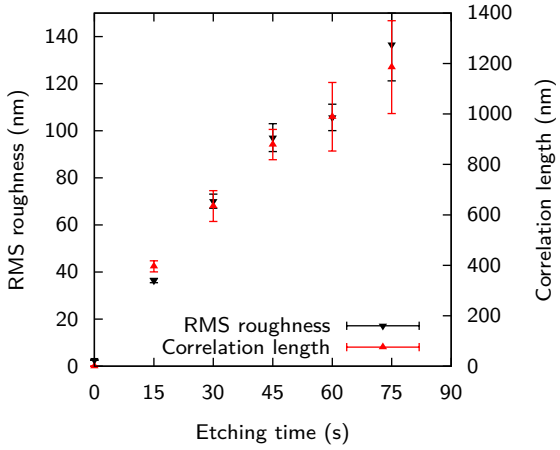

Figure 7.3.: The RMS roughness and correlation length of the etched ZnO:Al layers onto which the solar cells were deposited.

Table 7.1.: The dependence of the external parameters of the deposited solar cells on the rms roughness of their front TCO layers. The parameters were measured with an Pasan IIc sun simulator / solar tester setup and averaged on the best 10 cells of stripes with 30 cells. The solar cell area was 0.16 cm^2.

σ_r (nm)	V_{oc} (mV)	J_{sc} (mA/cm^2)	FF (%)	Efficiency (%)
flat (2)	885	14.4	60.6	7.77
35	888	16.3	63.9	9.25
70	887	16.9	62.6	9.42
95	887	17.1	63.6	9.64
105	866	14.5	59.3	7.46
135	869	14.6	59.1	7.50

morphology is smoother than of the ZnO:Al interfaces resulting in a lower rms roughness of about 15 nm, 50 nm and 85 nm, respectively. The AFM scans were obtained with the instrument from Veeco mentioned in Section 3.2. Figure 7.3 shows the RMS roughness and the correlation length of the ZnO:Al layers as a function of the etching time. The shown values are the averages of σ_r and ℓ_c for five different AFM scans. As we can see from the figure, σ_r and ℓ_c are proportional to each other, which indicates that the depths of the craters (related to σ_r) and the width of the craters (related to ℓ_c) grow at proportional rates during etching.

Table 7.1 and Fig. 7.4 show the average external parameters of the 10 best cells of each stripe. They were determined with an Pasan IIc sun simulator / cell tester setup. We observe that the first four stripes (flat and with $\sigma_r \approx 35, 70, 95$ nm) show a very stable open circuit voltage (V_{oc}) and fill factor (FF), while the short circuit current density (J_{sc}) and thus the efficiency are increasing with the roughness. The two stripes with the highest σ_r have the lowest efficiency compared to the first four stripes. Since the first four stripes form a very stable set of samples with different surface morphologies, we will use those for validating the combination of the new scattering model with `ASA`.

7.3. Simulating solar cells with ASA

In this section we validate the combination of the scattering model with the `ASA` opto-electric device simulator. For the simulations of the solar cells we used a layer structure as in Fig. 7.1. We assumed two scattering interfaces: The interface of ZnO:Al with the nc-Si:H p-layer and the interface of the a-Si:H n-layer with the back metal. To calculate the AID and haze in transmission and reflection for light traversing in forward and backward direction for the two interfaces, we used the program described in Appendices C and D. As input we used AFM scans of 20×20 µm^2. As discussed in Appendix E, an AFM resolution of $N = 512$ is required in this case. Since we only had scans with $N = 256$ available, we generated scans with $N = 512$ from those with $N = 256$ through linear interpolation.

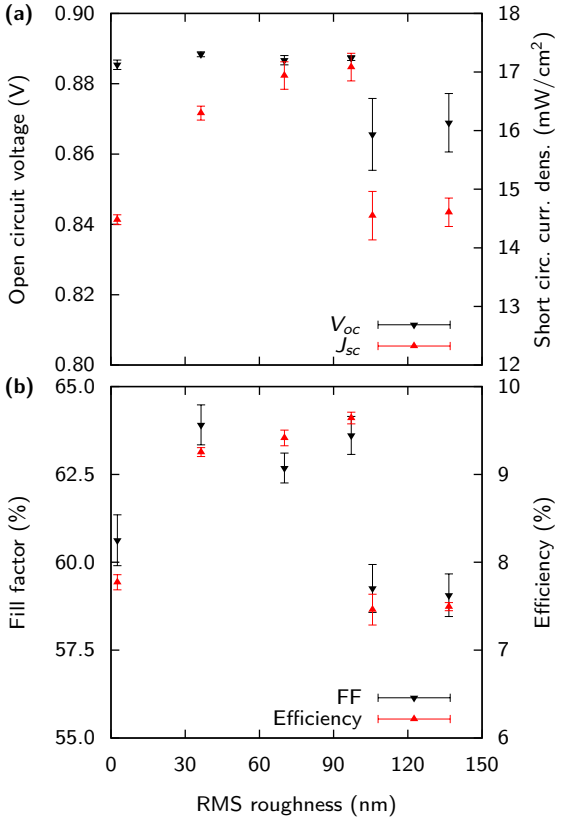

Figure 7.4.: The external parameters of the deposited solar cells in dependence of the RMS roughness of their front TCO layers. The parameters were measured with an Pasan IIc sun simulator / solar tester setup and averaged on the best 10 cells of stripes with 30 cells. The solar cell area was 0.16 cm^2.

In our simulations we tested two different morphologies for the Si-metal interface: First we used the accurate morphology obtained from an AFM scan of the back of the p-i-n structure. Secondly we assumed that both scattering interfaces at either side have the same morphology, *i.e.* the morphology of the ZnO:Al.

To obtain the generation profile with `ASA`, we used the `GENPRO 3` module. In `GENPRO 3`, light that hits a scattering interface is split into a specular coherent component and a scattered incoherent component, according to the haze. The specular component then is treated according to coherent thin-film optics and thus also predicts interference. Since the scattered light is treated incoherently, `GENPRO 3` is dealing with partially coherent light.

We found an offset between the J_{sc} values obtained from the measured external quantum efficiency (EQE) and from the *J-V* measurement with the solar simula-

Table 7.2.: The factor $\beta = J_{sc}(\text{EQE})/J_{sc}(J\text{-}V)$ that is used to scale the measured J-V values. For the flat cell the average value of the other three cells is taken.

σ_r (nm)	β (–)
35	0.937
70	0.921
95	0.911
flat (2)	0.923 (avg.)

tor. Since for calculating J_{sc} from the EQE the AM 1.5 spectrum is used, just as for determining J_{sc} in `ASA`, we decided to scale the measured J-V curves with a factor $\beta = J_{sc}(\text{EQE})/J_{sc}(J\text{-}V)$ before comparing them to the `ASA` results. Due to a calibration error for the EQE measurement of the flat cell, the EQE was out of scale by a constant factor over the whole spectrum. We scaled the J-V curve with $\bar{\beta}$, *i.e.* the mean of the β values of the other solar cells. We further scaled the EQE of the flat cell such that $J_{sc}(\text{EQE}) = \bar{\beta} J_{sc}(J\text{-}V)$ was satisfied. All used values for β are shown in Table 7.2, where we see that the deviations increase with roughness.

Figure 7.5 shows the simulated and measured EQE and J-V characteristics of the flat cell (a), the cell deposited onto ZnO:Al with moderate roughness ($\sigma_r \approx 35$ nm) (b) and the cell with high roughness ($\sigma_r \approx 95$ nm) (c). The EQE was measured without bias light. In the flat cell scattering can be neglected. Thus it can be assumed that thin-film optics is sufficient for calculating the absorption profile. We therefore used the flat cell for the calibration of the electric parameters in order to obtain a good fit between the simulations and the measurements. Thereafter we calibrated the thicknesses of the different layers. While the TCO thickness determines the interference fringes up to approximately 600 nm, the i-layer thickness determines the interference fringes for longer wavelengths, where the Si becomes transparent. The thickness of the p-layer can be used to calibrate the EQE in the blue, since this layer absorbs a significant amount of the blue light. The results of the calibrated simulations for the flat cell are shown in Fig. 7.5 (a). The fits for both the EQE and the J-V characteristics are very good. After calibrating `ASA` for the flat cell, the cells with nano-textured interfaces could be simulated straightforwardly. We introduced two scattering layers into the solar cell as described at the beginning of this section. We used the same electrical parameters and layer thicknesses as for the flat cells, only the TCO thickness and the series resistance, which mainly controls the fill factor, had to be calibrated for each cell. To take the anti-reflective (AR) effect of the rough interfaces into account, we included a 1 nm thick non-absorptive effective layer with constant refractive index $n = 3$ between the TCO layer and the first p-layer. A summary of all used layers and their thicknesses is given in Table 7.3.

As can be seen in Fig. 7.5 (b) and (c), the fits for the rough cells are very satisfying when we use accurate interface morphologies for both scattering interfaces (solid red lines). In (b) the intensity of the interference fringes is slightly underestimated by the simulations. In (c) the simulated EQE slightly underestimates

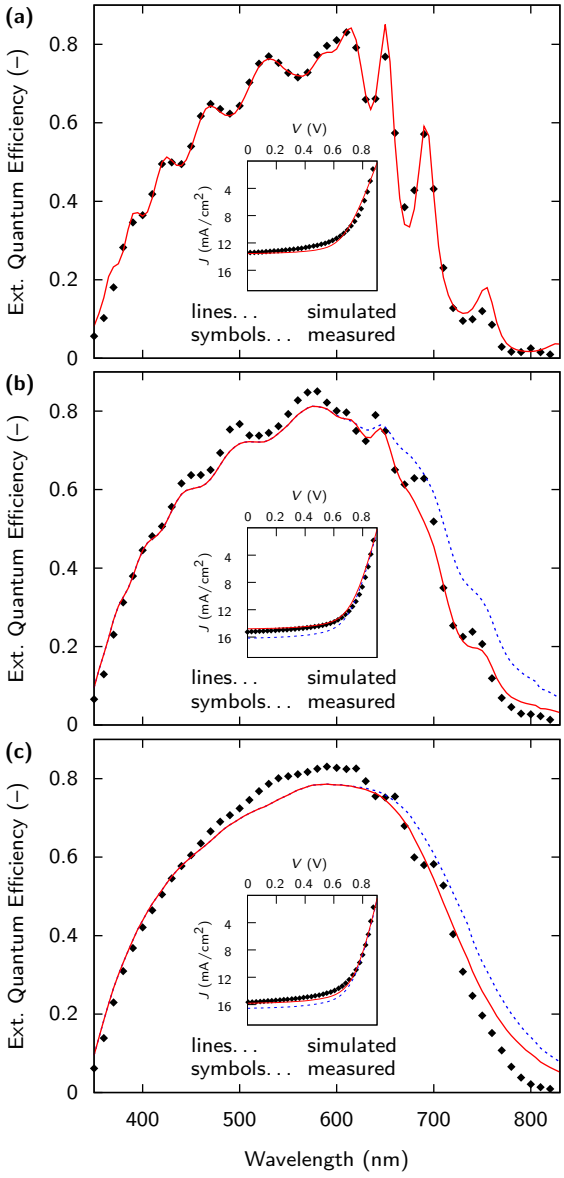

Figure 7.5.: The results of the simulations with ASA for the cell with (a) flat interfaces, with (b) $\sigma_r \approx 35$ nm and with (c) $\sigma_r \approx 95$ nm (c). The large figures show the EQE while the insets show the J-V characteristics. The red full lines in (b) and (c) show results of simulations were the accurate morphology of the Si-metal interface was used. For the simulations represented by the blue dashed lines it was assumed that the Si-metal interface has the same morphology as the TCO-Si interface.

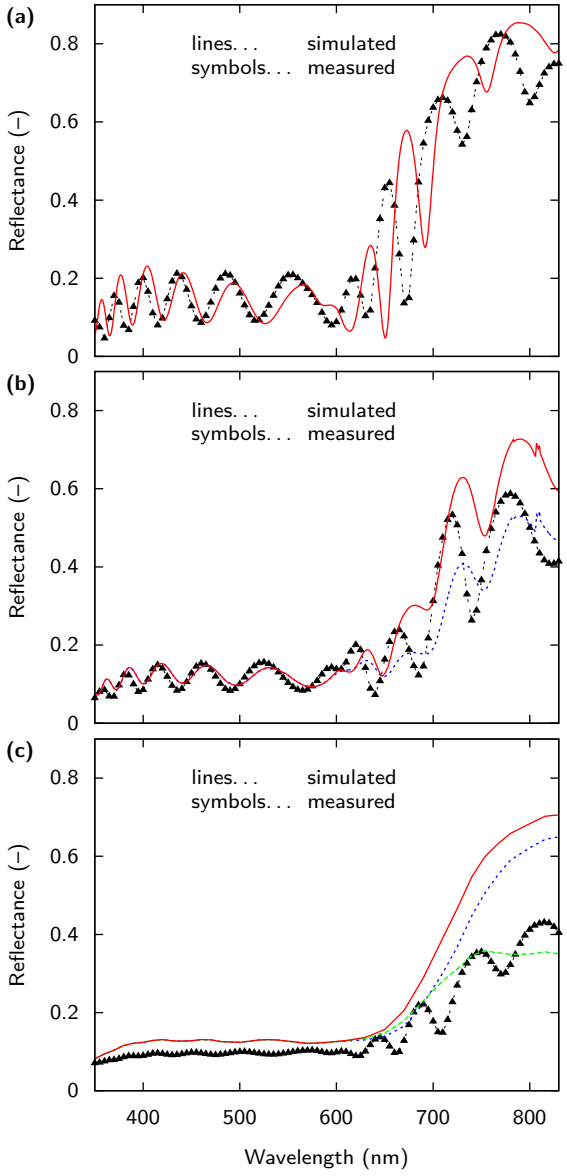

Figure 7.6.: The simulated and measured reflectivity of the cell with (a) flat interfaces, with (b) $\sigma_r \approx 35$ nm and with (c) $\sigma_r \approx 95$ nm (c). The red full lines in (b) and (c) show results of simulations were the accurate morphology of the Si-metal interface was used. For the simulations represented by the blue dashed lines it was assumed that the Si-metal interface has the same morphology as the TCO-Si interface.

Table 7.3.: The used layers and their thicknesses for the ASA simulations. The first row characterises the three simulated cells by their TCO morphology. All values are in nm.

Morphology	**flat**	$\sigma_r \approx$ **35**	$\sigma_r \approx$ **95**
glass	10^6	10^6	10^6
ZnO:Al	900	840	650
effective AR layer	–	1	1
nc-Si:H p-layer	6	6	6
a-SiC:H p-layer	8	8	8
a-SiC:H buffer layer	5	5	5
a-Si:H i-layer	744	744	744
a-Si:H n-layer	20	20	20
effective Al like layer	1	1	1
silver back reflector	300	300	300

the measured EQE between 450 nm and 600 nm and overestimates it above 700 nm. One reason for the shortcomings seen in (c) is the assumption that the solar cell consists of flat layers with rough interfaces that scatter the light. However, the maximal feature height of the 95 nm ZnO:Al is approx. 800 nm making the applicability of this flat-layer approach doubtful.

The intensity of the interference fringes above approximately 600 nm is strongly underestimated in both (b) and (c). Since the haze decreases with increasing wavelength, one would expect the intensity of the fringes increasing with the wavelength. This indeed can be observed at the measured EQE, while it obviously is not the case for the simulated data. The scattering model itself predicts the trend of the haze correctly, as shown in Fig. 5.6. However, above 600 nm light that is reflected from the (textured) Si-metal interface at the back becomes important. The presence of two scattering interfaces leads to increased complexity. GENPRO 3 does not take into account that the two scattering interfaces have correlated morphologies. In general, the shape of the EQE is predicted well for all three cases shown. The scattering model therefore allows predicting the influence of nano-textured interfaces on the performance of thin-film silicon solar cells.

The blue dashed lines in Fig. 7.5 (b) and (c) show the simulation results when one assumes that the interface morphologies at the TCO-Si and at the Si-metal interface are the same. Since in this case the smoothing effect of the p-i-n layers on the morphology is neglected, the scattering is too high resulting in an overestimated EQE above 600 nm. We observed (not shown) that one can get a good fit in the red part of the spectrum when adding a 1-nm thick layer with the optical properties of aluminium between the n-layer and the silver back reflector. Several authors used such a layer and argued that the reflectivity of interfaces between n-type a-Si:H and Ag is lower than expected from the Fresnel equations [99, 119]. It seems that in these papers the overestimated scattering at the back was compensated by artificially reducing the reflectance of the Si-metal interface.

In Fig. 7.6 the simulated and measured reflectivity of the different solar cells is

shown. Since the dots that were used for measuring the *J-V* characteristics and the EQE were scratched by these measurements, the reflectivity had to be measured at different dots, leading to slightly different layer thicknesses and thus interference fringes. Besides this mismatch between simulated and measured interference fringes, the results for the flat cell, shown in Fig. 7.6 (a), are very satisfying. For the cell with $\sigma_r \approx 35$ nm, shown in Fig. 7.6 (b), a good match is observed up to about 600 nm. For longer wavelength, the intensity of the interference is underestimated, as already discussed above. While using the accurate morphology leads to an overestimated *R* (red line), assuming that the Si-metal interface has the morphology of the TCO leads to a better match (blue dashed line). There is no good match between simulations and measurements for the cell with $\sigma_r \approx 95$ nm. The simulated *R* is higher than the measured one, even below 600 nm. Above 600 nm, the difference becomes very big for both morphologies of the TCO-Si interface. In the simulations, no interference is seen at all. The green dashed line shown in (c) assumes the accurate morphology at the rough back interface, but aluminum instead of silver. There, the match is much better. However, this assumption leads to a much too low EQE for long wavelengths (not shown). A possible reason for the mismatch between simulated and measured *R* for cells with rough interfaces is parasitic plasmonic absorption that is present at rough Si-Ag interfaces and cannot be modelled with ASA yet. It might be an interesting future project to study how plasmonic absorption at rough metal interfaces can be implemented in ASA.

In this chapter we validated the scattering model on solar cells with a 700-nm thick i-layer. We used a thick i-layer because the far field approach used to develop the scattering model is more justified for thicker i-layers. For thinner i-layers with a thickness of 250 nm to 300 nm, as they are used in state-of-the-art solar cells, also near field optics may be important for accurate modeling [118]. Further, for cells with thin i-layers the applicability of the flat-layer approach is even less justified than for the case of the 700 nm cell studied in this work. Even though the partial destruction of the coherence of the light will be predicted well by the scattering model when it is combined with `GENPRO 3`, simulating solar cells with thin i-layers remains a complex topic. We, however, expect that the achievements presented in this work are well applicable to microcrystalline solar cells, which contain i-layers with thicknesses in the order of micrometers.

7.4. Conclusions

In this chapter we combined the scattering model presented in chapter 5 with the opto-electric `ASA` simulation software and tested it by simulating and measuring the *J-V* curves, the EQE and the reflectivity of solar cells with different surface morphologies. This test showed that the scattering model is able to predict the influence of the nano-textured interfaces on the solar cell performance.

One of the things that I think we have learned is that we should all be very careful about making predictions about the future.

William Jefferson Clinton

8 Optimised interface morphologies

8.1. Introduction

One of the major motivations for developing models is that they enable us to simulate physical systems, which have not (yet) been realised experimentally.* Furthermore, models allow to investigate the effect of a changed parameter much faster than it usually is possible with experiments. Modelling then can help to deepen the understanding of the physics that governs the studied system. It therefore is natural to apply scattering models for investigating morphologies that lead to a maximised photo-current in thin-film silicon solar cells. Several authors have tackled this problem in recent years:

Fahr *et al.* succeeded in simulating a one-dimensional interface morphology that suppresses k-space domains related to evanescent waves and to small angles [120]. They did this by using the iterative Fourier transform algorithm [121]. Dewan *et al.* and Peters *et al.* calculated the optimal period/height combination for one-dimensional gratings [122, 123]. All three, Fahr *et al.*, Dewan *et al.* and Peters *et al.* calculated the absorption in thin-film silicon layers with the rigorous coupled wave approach (RCWA) [124–126]. RCWA is a fast rigorous method to solve Maxwell's equations at (one-dimensional) gratings. Čampa *et al.* performed an optimisation for one-dimensional gratings [127], for which they applied the finite elements method (FEM) [93]. Bittkau *et al.* calculated and measured the field

*Of course, one must be very careful about the assumptions made in the model and thus the applicability of the model to the studied problem!

directly above a one-dimensional section of a ZnO:Al texture [118]. They further performed one-dimensional calculations of the absorption in a silicon layer and performed an optimisation by stretching the texture vertically. For their calculations they used the method by Chandezon *et al.* [128, 129]. Martins *et al.* succeeded in superposing one-dimensional gratings with different periods such that scattering into small angles was suppresses and thus more energy was scattered into large angles [130].

Rockstuhl *et al.* managed to extend the work presented in Ref. [120] to two-dimensional surfaces [131]. In their paper they also study the effects of vertically stretching ZnO:Al and ZnO:B textures, similar to the textures we discussed in Section 3.2. Dewan *et al.* managed to transfer their work to two-dimensional structures as well [132]. They approximated the nano-textured surface with square-based pyramids and performed an optimisation on the base-length and height of the pyramid. Both Rockstuhl *et al.* and Dewan *et al.* used implementations of the FDTD method for their optical simulations [91, 92]. Isabella *et al.* performed three-dimensional optical simulations of solar cells with one- and two-dimensional gratings and performed optimisations for different grating-periods and -heights with the FEM method [133].

From this little literature review we can conclude the following: While simulations performed on one-dimensional textures can be performed fast, *e.g.* with RCWA or Chandezon's method, calculations on two-dimensional systems are usually done with much more cumbersome FDTD or FEM approaches.

Our scattering model discussed in Chapter 5 and applied to full solar cells in Chapter 7 allows us to investigate scattering on two-dimensional optimised nano-textures much faster, although approximate. To perform this optimisation we need two building blocks beside the scattering model: The first building block is an algorithm that is able to create nano-textured surfaces. The second building block is an optimisation algorithm. To evaluate the results obtained from the optimisations we calculated the external quantum efficiency with `ASA`. We describe the used algorithms in Section 8.2. In Section 8.3 we discuss the results obtained from the optimisation procedure. In Section 8.4 we evaluate the consequences of these results on the design of surface textures. Finally, in Section 8.5 we compare our results with work from other authors. The content of Sections 8.2–8.4 was published in Ref. [134].

8.2. Theory

8.2.1. Generating nano-textures with the Perlin noise algorithm

To generate nano-textured surfaces on our computer, we used the Perlin noise algorithm that was developed by Ken Perlin in the 1980s [135, 136]. For our application Perlin noise is very well suited since it combines randomness with well

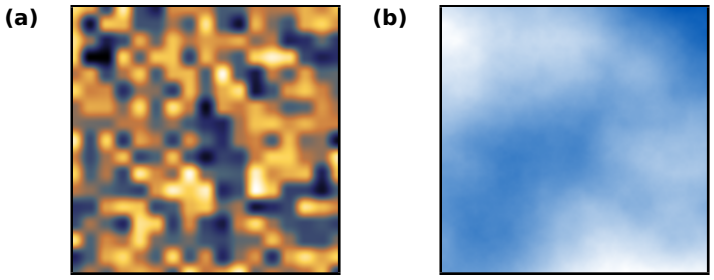

Figure 8.1.: (a) A surface texture generated with the Perlin noise algorithm. For this texture, the feature size is one sixteenth of the side length of the square. (b) A fractal surface texture looking like a cloudy sky generated by superposing Perlin noise of feature size 1, ½, ¼... with respect to the side length. The rms roughness of each generation scales with the feature size.

controlled lateral feature sizes. For example, to generate a random texture with a mean feature distance of 1 on a square with side length 10, we have to assign a random number $z(x,y)$ between 0 and 1 to every point of the rectangle with integer coordinates, *e.g.* (3,5). The values of the points in between these integer coordinates are then given as an interpolation of the neighbouring integer coordinates. We used a cosine interpolation in order to assure that the first derivative of the surface is continuous. The points in the square enclosed by the square (0,0), (0,1), (1,0), (1,1) are given by

$$\begin{aligned} z(x,y) = {} & z(0,0)c(x)c(y) + z(0,1)c(x)f(y) \\ & + z(1,0)f(x)c(y) + z(1,1)f(x)f(y), \end{aligned} \tag{8.1}$$

where

$$c(x) = \frac{1}{2}\left[1 + \cos\left(\frac{x}{\pi}\right)\right] \qquad \text{and} \qquad f(x) = \frac{1}{2}\left[1 - \cos\left(\frac{x}{\pi}\right)\right]. \tag{8.2}$$

Figure 8.1 (a) shows an example of a texture generated with Perlin noise, whose lateral feature size ℓ[†] is one sixteenth of the side length of the square. In this and all subsequent textures the average plane was subtracted. When we superpose different *generations* of Perlin noise with lateral feature size 1, ½, ¼... with respect to the side length, we can generate a fractal surface texture that looks like "cloudy sky", as illustrated in Fig. 8.1 (b). We just have to assure that the rms roughness σ_r of the generations scales with its feature size, *i.e.*

$$z_{\text{tot}}(x,y) = z_1(x,y) + \tfrac{1}{2}z_2(x,y) + \tfrac{1}{4}z_4 + \ldots, \tag{8.3}$$

where the subscript denotes the inverse of the feature size as a fraction of the side length.

[†]The lateral feature size ℓ is not to be confused with the correlation length ℓ_c introduced in Section 3.2.

8.2.2. The simulated annealing algorithm

To perform the optimisation we used the simulated annealing algorithm [137, 138]. This Monte-Carlo algorithm [139] allows optimising systems, which are controlled by a set of parameters $\mathbf{c}$, via a *cost function* C that is minimised during the optimisation. An optimised set of system parameters is found by "cooling" the system just as a molten metal crystallises to configurations of lowest potential energy when it is cooled. By cooling the system fast, small crystals will emerge. Their energy is slightly higher than that of the large crystals emerging when the system is cooled down slowly. Thus there is a trade-off between the cooling rate and the quality of the optimisation. In detail the optimisation is done as follows:

Before the optimisation starts a cost function must be defined that is minimised during the optimisation just as the potential energy of a molten metal is minimised during cooling. Further an initial set of parameters $\mathbf{c}_0$ needs to be chosen, usually with random numbers, and a starting temperature T_0 needs to be set. At the beginning of every optimisation step one system parameter is chosen randomly that is slightly varied (or "tweaked") depending on a random number. Next, the cost C_i is calculated with the changed parameter set $\mathbf{c}_i$. If $C_i < C_a$, where the subscript a denotes the last accepted set of parameters, $\mathbf{c}_i$ is accepted as new parameter set, $\mathbf{c}_a = \mathbf{c}_i$. Else, C_i is accepted according to the probability

$$\mathfrak{P} = \exp \frac{C_a - C_i}{T_i}, \tag{8.4}$$

which is analogous to the Maxwell-Boltzmann distribution, $\exp(-E/kT)$. At the end of each step, the system is cooled with a constant factor d, $T_{i+1} = dT_i$. Clearly, the smaller d the faster the system will cool. Due to this cooling, $\mathfrak{P}$ decreases as the simulation progresses, *i.e.* it becomes more unlikely that the parameter set $\mathbf{c}_i$ is accepted if $C_i > C_a$. If $T \equiv 0$ throughout the simulation, $\mathfrak{P}$ will always be 0. Such a simulation is called *greedy*.

8.2.3. Optimising nano-textures

To study optimised surface textures we combined the Perlin noise algorithm with simulated annealing. We generated textures similar to the fractal textures in Eq. (8.3) but with the difference that we used variable sets of coefficients $\mathbf{c} = (c_1, c_2, c_4 \ldots)$ instead of the fractal set (1, ½, ¼...). At the beginning of every optimisation run we generated ten Perlin textures of every generation and we generated an initial set of coefficients $\mathbf{c}_0$. We thus had ten different textures generated with the same set of coefficients,

$$z^{0,j}(x,y) = c_1^0 z_1^j(x,y) + c_2^0 z_2^j(x,y) + c_4^0 z_4^j + \ldots, \tag{8.5}$$

where $j \in \{1, 2, 3 \ldots 10\}$. The total cost then is given as the average of the cost of every of the ten textures. We used different cost functions, which are discussed in detail in the next section.

We further used the *random search* method. In that method the set of coefficients **c** is kept constant throughout a simulation run. However, for every optimisation step a new set of textures z_k^j is generated, which is added onto the last accepted set z_k^a. The so obtained texture then is renormalised such that the total rms roughness stays constant. This texture is accepted according to the same rules as in the simulated annealing algorithm.

8.3. Optimisation results

As first optimisation we performed a random search for fractal textures. As a cost function we used the (negative) haze in transmission at 600 nm at an interface between TCO and air. For this optimisation one wavelength was sufficient since the haze of random textures decreases monotonically with the wavelength if the refractive indices of the materials do not vary too strongly, as discussed in Section 5.3. As a reference surface we used Asahi U-type [75], which is known to be one of the best TCOs available on the market for a-Si:H single junction TFSSC. This TCO has a pyramid-like structure and an rms roughness $\sigma_r \approx 40$ nm. During this and all subsequent optimisations, the rms roughness of the texture was kept constant at 40 nm.

Figure 8.2 shows the results of this optimisation. While the haze indeed is significantly higher than that of the reference, the AID of the fractal surface decays much faster, *i.e.* the light is scattered into much smaller angles. Therefore also the (simulated) EQE is smaller than that of the reference sample. The EQE was simulated with the `ASA` software as described in Chapter 7. Here and in all forthcoming `ASA` simulations we used the same electrical parameters, optical constants and layer thicknesses. We assumed one scattering layer between the TCO and the silicon, as illustrated in the sketch next to Fig. 8.2 (c). The haze and AID of this layer were calculated with our scattering model as discussed in Chapter 5.

This result reconfirms that the haze alone is not sufficient to judge the effectiveness of a scattering surface, but that also the AID must be taken into account. Further this optimisation shows that fractal interfaces are not suitable light scatterers. We therefore performed simulated annealing optimisations to find optimised sets of coefficients **c**. We performed optimisations for TCO-air and TCO-silicon interfaces.

As cost function for the TCO-air system, we used the absorption in a layer, whose thickness is equal to its penetration depths during one pass,[‡]

$$C_{\text{air}}^{\text{TCO}}(\lambda) = \sum_i \text{AID}(\lambda, \theta_i) \left[1 - \exp\left(-\frac{1}{\cos\theta_i}\right)\right], \tag{8.6}$$

where the sum extends over all angles larger than 10°. To optimise for more wavelengths at once, we also combined more of such terms, $C_{\text{tot}} = C(\lambda_1) + C(\lambda_2) + \ldots$

[‡]For better readability we use the notation λ instead of λ_0, *i.e.* we omit the subscript in this chapter.

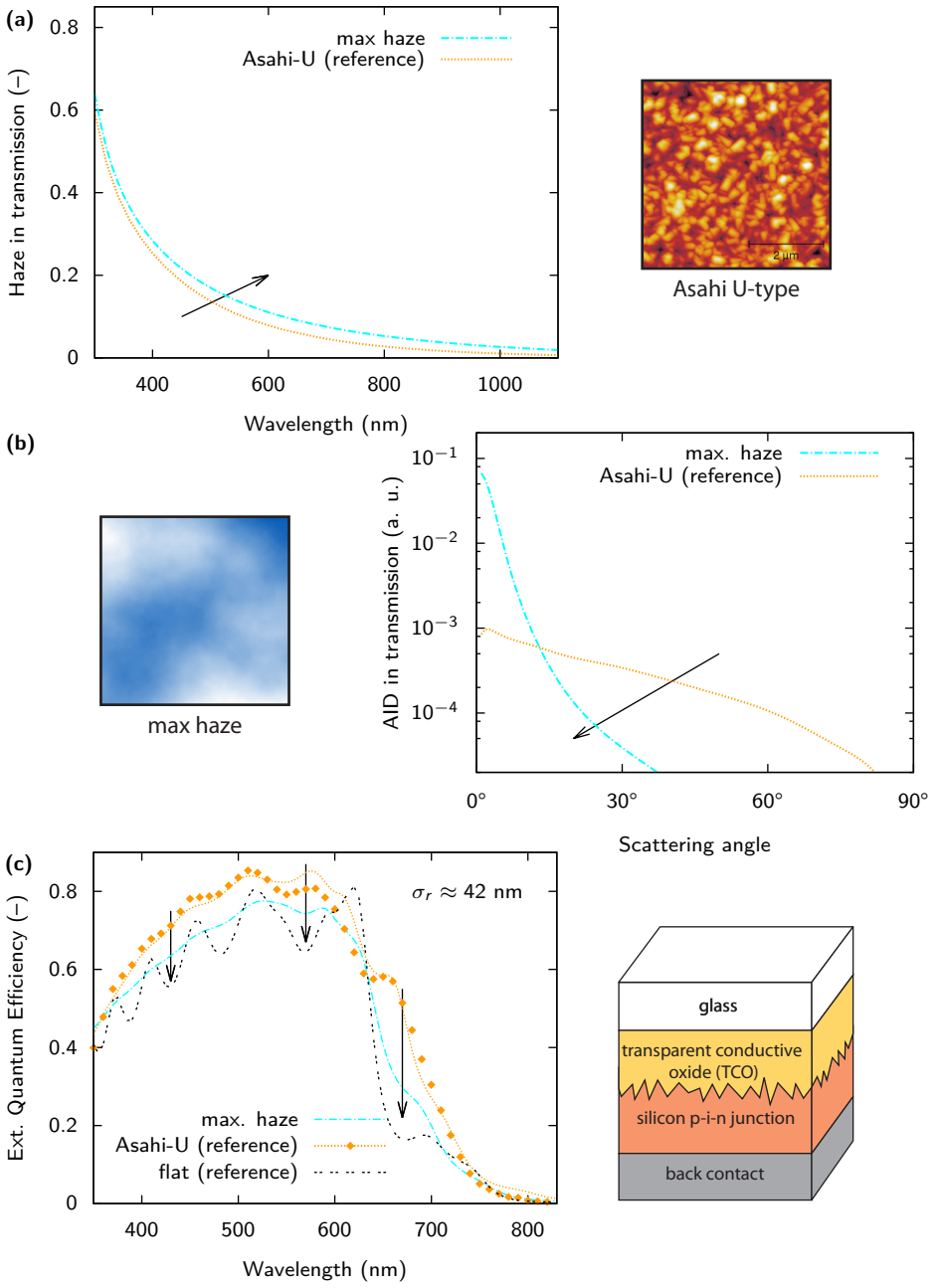

Figure 8.2.: (a) Haze and (b) AID_T for a Perlin fractal optimised for maximal haze and reference Asahi U-type ($\sigma_r \approx 40$ nm for both). While the haze of the fractal is higher than that of Asahi U, the AID_T decays much faster, (c) leading to a lower EQE. Also the measured EQE of a cell on Asahi-U (dots) and the simulated EQE of a flat cell are shown.

Table 8.1.: Optimal lateral feature size

TCO-air	312 nm
TCO-Si	78 nm

The results of these optimisations were very surprising: Independent of the optimisation was done for one or two wavelengths, only one generation of Perlin textures survived while all other generations were suppressed. In the case of 600 nm the surviving texture has a feature size of 312 nm. This result is independent of the σ_r of the texture, at least for values between 40 and 200 nm.

For the TCO-silicon system we considered the absorption in a 300 nm thick a-Si:H layer at a single pass. Again we only considered the light that was scattered into angles larger than 10°. Further, we limited the wavelength range from 600 to 900 nm, with a step size of 50 nm. We did not take wavelengths shorter than 600 nm into account since for these wavelengths the penetration depth in a-Si:H is much shorter than the layer thickness, thus the light is absorbed in any case. We weighted the cost function with the incident photon flux in each of these intervals, according to the AM 1.5 spectrum. As cost-function we thus obtained

$$C_{\mathrm{Si}}^{\mathrm{TCO}} = \sum_{i,j} \mathrm{AM}_i^{1.5}(\lambda_i) \cdot \lambda_i \cdot \mathrm{AID}(\lambda_i, \theta_j) \left\{ 1 - \exp\left[-\frac{\alpha(\lambda_i) d}{\cos\theta_j} \right] \right\}, \qquad (8.7)$$

where $\alpha(\lambda_i)$ is the the absorption coefficient of a-Si:H and d is the thickness of the layer, in our case $d = 300$ nm. $\mathrm{AM}_i^{1.5}(\lambda_i)$ is the incident irradiance from the AM 1.5 spectrum in the wavelength interval $(\lambda_i - \Delta\lambda/2, \lambda_i + \Delta\lambda/2)$ and $\Delta\lambda = \lambda_{i+1} - \lambda_i$. The multiplication with λ_i is done since we want to maximise the number of absorbed photons.

Again we obtained the same result: all generations except one were suppressed. In this case the optimisations led to an optimal feature size of 78 nm. This feature size is much smaller than the optimal feature size at TCO-air interfaces, which can be understood from the fact that the wavelength inside a-Si:H is about a factor 4 shorter than in air. Table 8.1 summarises the optimal lateral feature size for TCO-air and TCO-silicon systems.

8.4. Parameter study

To evaluate and understand the results from the simulations we studied the influence of ℓ and σ_r on the scattering parameters and the performance of solar cells in more detail. Figures 8.3 (a) and 8.4 (a) show the haze and AID of Perlin textures with different lateral feature sizes ℓ at TCO-air interfaces. The rms roughness of the Perlin textures was constant, $\sigma_r = 40$ nm. To obtain optimised textures, a short random search was performed for every value of ℓ. While the haze increases slightly with ℓ, the AID decays much faster. We therefore have to take the

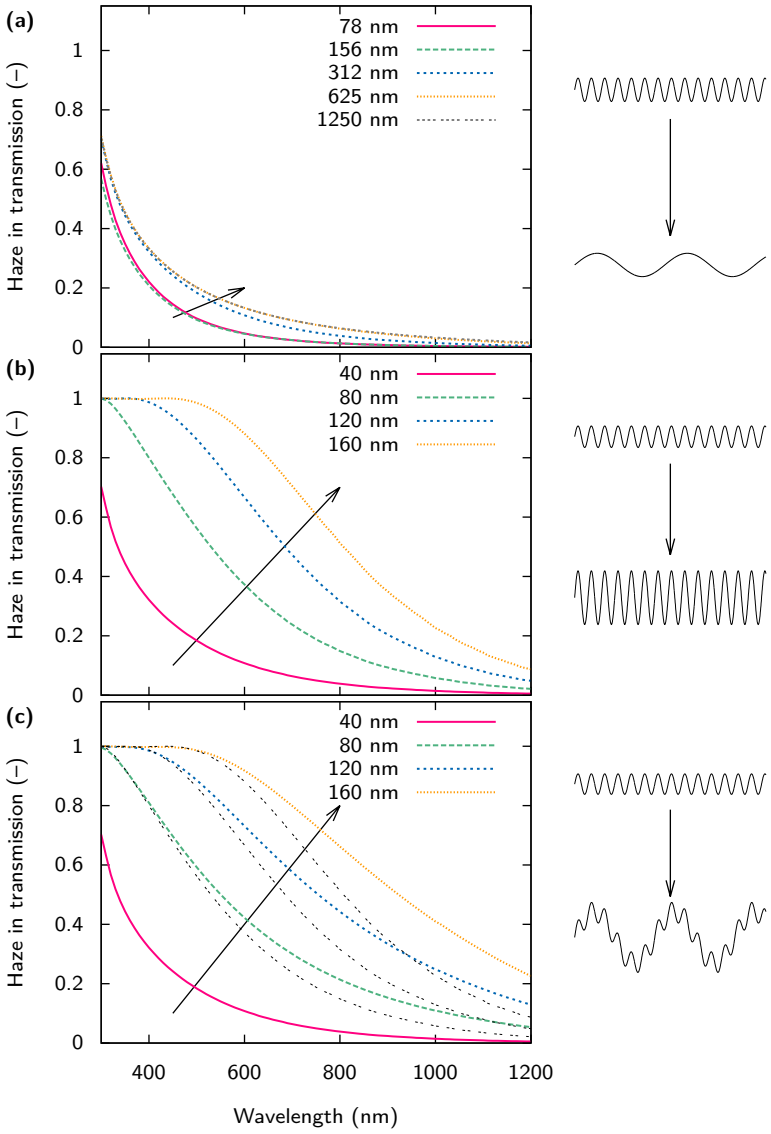

Figure 8.3.: Influence of the lateral feature size ℓ and rms roughness σ_r of TCO-air interfaces on the haze: (a) Influence of changing ℓ at Perlin textures with $\sigma_r \approx 40$ nm. (b) Influence of changing σ_r at Perlin textures with $\ell = 312$ nm. (c) Influence of superposing a structure with $\ell = 312$ nm ($\sigma_r \approx 40$ nm) with a structure with $\ell = 1250$ nm, such that the total σ_r is 80, 120 or 160 nm. The dashed black lines show the haze values presented in (b).

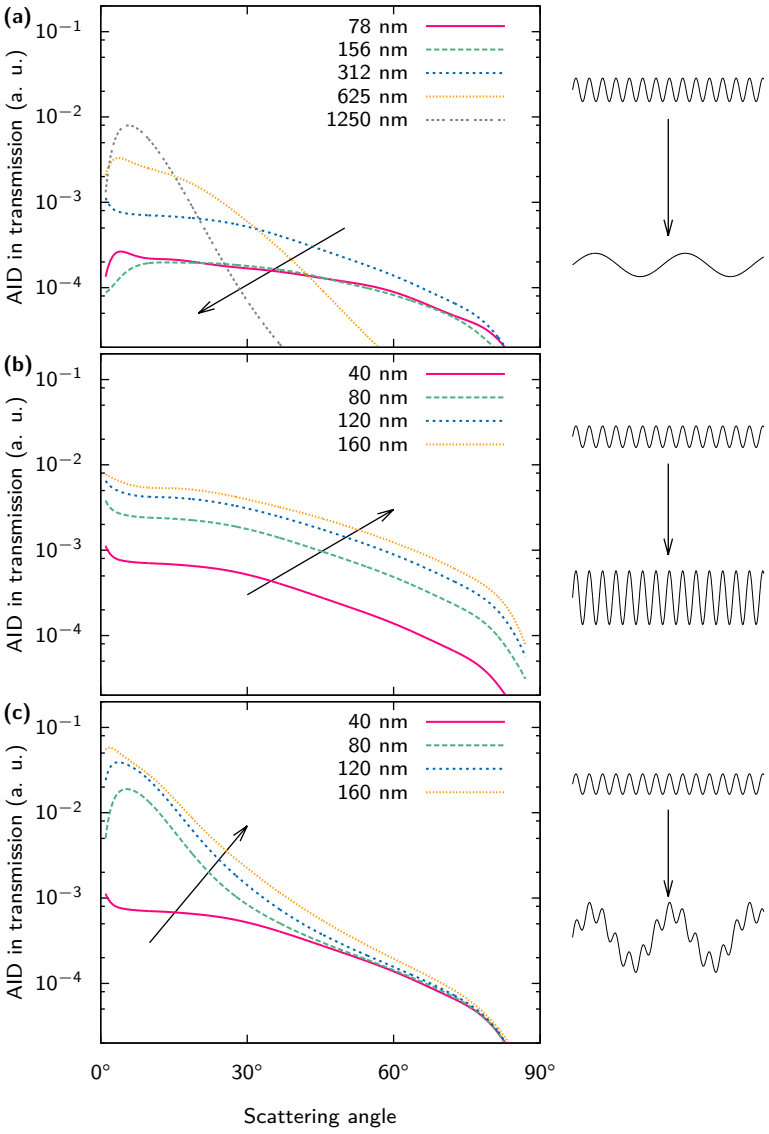

Figure 8.4.: Influence of the lateral feature size ℓ and rms roughness σ_r of TCO-air interfaces on the AID: (a) Influence of changing ℓ at Perlin textures with $\sigma_r \approx 40$ nm. (b) Influence of changing σ_r at Perlin textures with $\ell = 312$ nm. (c) Influence of superposing a structure with $\ell = 312$ nm ($\sigma_r \approx 40$ nm) with a structure with $\ell = 1250$ nm, such that the total σ_r is 80, 120 or 160 nm.

trade-off between increasing haze and faster decaying AID into account. At very small lateral feature sizes the haze decays because the light does not see a nano texture any more but experiences the surface as an effective medium [131].

Besides studying the influence of changing ℓ when σ_r is kept constant, we also investigated the influence of a changing σ_r when ℓ is constant in Figs. 8.3 (b) and 8.4 (b). As expected, the haze reacts strongly upon changing σ_r. However, the AID_T does not change the shape at all, it merely shifts towards higher intensities.

These results indicate that the shape of the AID_T is controlled by lateral features while the horizontal features (and especially σ_r) control the haze. However, larger values of ℓ are beneficial for the haze as well.

Nano-textures with small ℓ size but a high σ_r (*i.e.* textures with sharp spikes) are very interesting from an optical point of view but have a detrimental effect on the electrical properties of the solar cell [140–142]. Modulated surface textures (MST) could be a possible solution to this problem. MST have been studied *e.g.* by Isabella *et al.* [143, 144]. In an MST, nano textures with low σ_r and ℓ are superposed with textures with high σ_r and ℓ. With this approach high σ_r values and small lateral features can be combined without the creation of sharp spikes. Figures 8.3 (c) and 8.4 (c) show the haze and AID_T of textures that were created by superposing the texture with $\ell = 312$ nm and $\sigma_r = 40$ nm with a texture with $\ell = 1250$ nm such that the total σ_r value is 80, 120 and 160 nm, respectively. We observe that the haze of these structures is higher than that of the $\ell = 312$ nm structures shown in Fig. 8.3 (b). However, the AID_T is only higher at narrow angles; at large angles the superposed texture shows hardly any effect. This shows that MST indeed can have a beneficial effect on the haze and the AID_T at small angles, however, they do not improve scattering into large angles.

As final part of this parameter study we take a look at (simulated) EQE curves of solar cells with Perlin textures with different lateral feature sizes. Again we assumed one rough interface between the TCO and the silicon layers. Figure 8.5 (a) shows the EQE for Perlin textures with different values of ℓ and $\sigma_r = 40$ nm. According to Table 8.1, the optimal lateral feature size is 78 nm. Here, hardly any difference between 78 and 156 nm lateral feature size can be seen. The simulated EQE of a solar cell with Asahi-U (not shown) would be nearly identical to that of the 156 nm Perlin texture, which can be understood from the fact that the correlation length of Asahi-U is about 175 nm. In Fig. 8.5 (b) we studied the effect of superposing textures with different lateral feature sizes (78 and 312 nm) while keeping σ_r constant. The calculated EQE is highest for the cell with the pure 78 nm texture and lowest for cell with the pure 312 nm texture. The EQE of the cell with a superposed texture lies in between those values, confirming the optimisation results that a texture with one optimised lateral feature size is superior to a texture consisting of a superposition of textures with different ℓ values. Figure 8.5 (c) shows the EQE for Perlin textures with different values of ℓ and $\sigma_r = 80$ nm. Here the 78 nm texture is slightly superior to the 156 nm texture. In an experiment, however, the sharper spikes of the 78 nm texture could induce higher electrical losses making the 156 nm texture more optimal in the end.

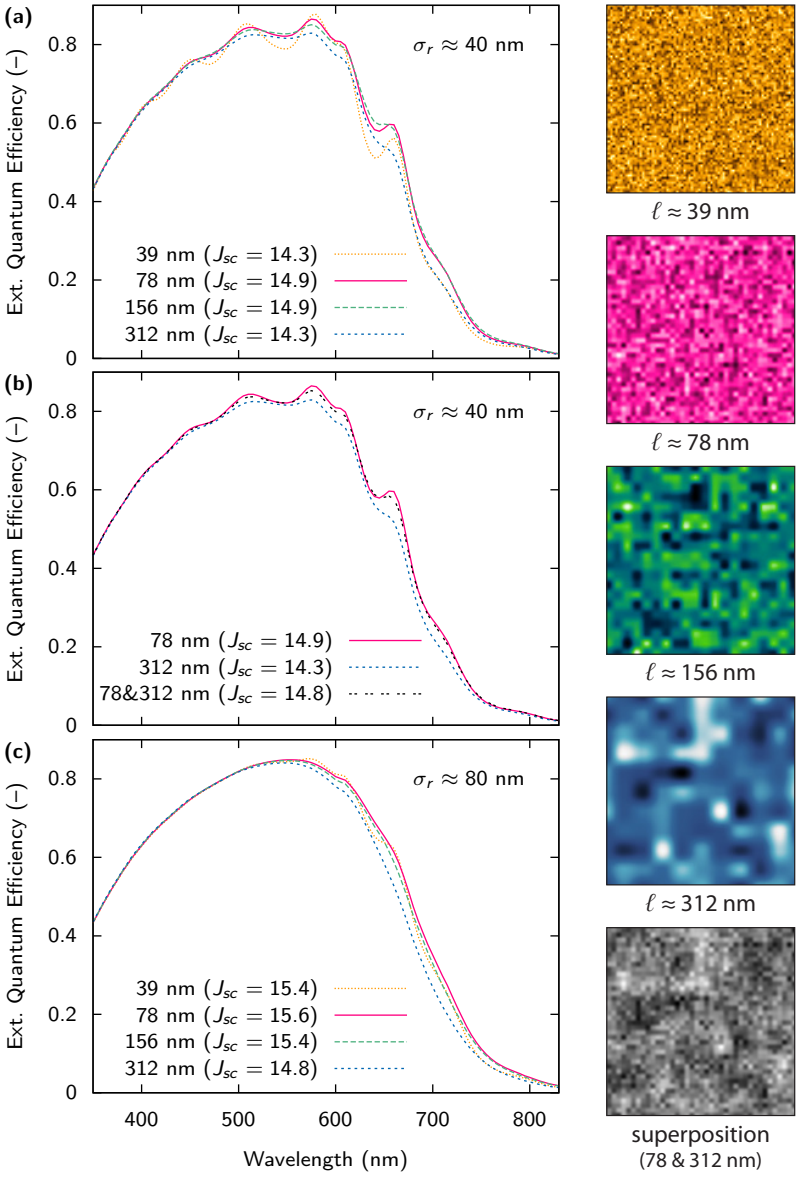

Figure 8.5.: (a) The EQE for an thin-film a-Si:H solar cell with Perlin textures with different lateral feature sizes and $\sigma_r \approx 40$ nm and (b) with superposition of two Perlin textures with different feature sizes. (c) Like (a), but with $\sigma_r \approx 80$ nm. The J_{sc} values are in mA/cm^2. The side length of the shown textures is 3 µm.

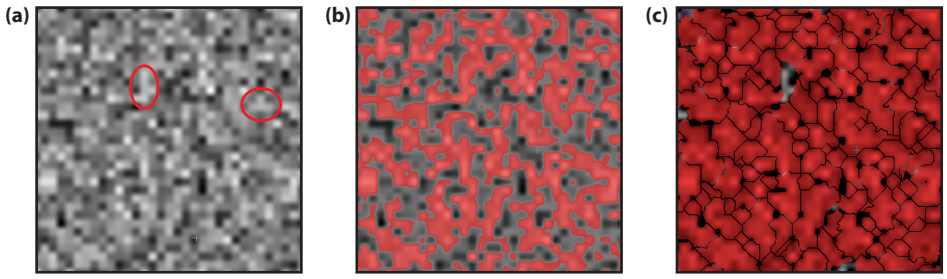

Figure 8.6.: (a) Two grains indicated on a Perlin texture with $\ell = 312$ nm. (b) The grains (in red) as obtained with the *threshold* method (c) and with the *watershed* method. The side length of the textures is 10 µm. The methods are described in Ref. [74]

8.5. Discussion

In this discussion we relate the results discussed above to recent research results from other authors. First, we want to mention recent results by Boccard *et al.* on a highly efficient a-Si:H/nc-Si:H tandem solar cell with an initial efficiency of 14.1% *et al.* [145]. Their cell contains a MST with very large smooth features from etched glass and small sharp features from ZnO:B. Even though they see a beneficial effect of the MST they argue that this effect is not only due to enhanced light trapping, but also due to less parasitic absorption in the doped layers, electrodes and back reflectors. Further, the loss in V_{oc} compared to their flat cell is lower than that of the reference single-texture cell, which can be attributed to less defects in the active layers of the MST-cell.

Secondly, we compare the results presented in Fig. 8.5 (a) and (c) to results for optimised periodic gratings for a-Si:H cells. Čampa *et al.* found that for one-dimensional rectangular gratings a period (height) of 300 nm (300 nm) is optimal [127]. Isabella *et al.* reported an optimal period (height) of 400 nm (300 nm) for one-dimensional rectangular gratings and 500 nm (450 nm) for two-dimensional gratings [133].

We found the optimal lateral feature size of the Perlin textures to be between 78 and 156 nm for a-Si:H. At first sight, there seems to be a big discrepancy between our results and those from Čampa *et al.* and Isabella *et al.* To resolve this discrepancy we take another look at Perlin textures, *e.g.* in Fig. 8.6 (a). We observe that most features are clustered in small groups of similar height that we call grains. Two of these grains are indicated in Fig. 8.6 (a). The scattering is mainly controlled by the grains and not by the small features that build up the grains.

To analyse the size of these grains in more detail, we performed a grain analysis, as shown in Fig. 8.6 (b) and (c). In (b) we used the *threshold* algorithm: The points with a height above 50% of the maximal height of the texture belong to grains. In (c), the *watershed* algorithm was used. In this algorithm, a drop of wa-

Table 8.2.: Average grain sizes radius of Perlin textures with different lateral feature sizes. All values are in nm.

ℓ	**threshold**	**watershed**
39	78	82
78	160	158
156	338	337
312	770	650

ter is placed at every point of the surface. Then the drops will flow together at the local minima (in this case the tops) and form little lakes – the grains. Both algorithms were described by Klapetek [74, 146]. As we can see, the grains obtained with the watershed algorithm are much better defined. To analyse the grain size we look at the radius r that a disk with the area of the grain would have.

Table 8.2 shows the average grain size radius $\bar{r}$ for the textures with different ℓ. We see that the differences between $\bar{r}$ obtained by the two methods is very small. Roughly speaking, $\bar{r} \approx 2\ell$. As we see from Fig. 8.6 (c) the texture can be interpreted as a *randomised* two-dimensional grating with period $2\bar{r}$, which is approximately 4ℓ. The optimal feature sizes between 78 and 156 nm therefore correspond to periods between 312 and 625 nm, which is in agreement with the findings by Čampa *et al.* and Isabella *et al.*

8.6. Conclusions

In this chapter we applied our scattering model to investigate optimised interface morphologies. To generate random nano-textures we superposed textures with different lateral feature sizes ℓ that were generated with the Perlin noise algorithm. An optimisation performed with the simulated annealing algorithm revealed that textures with one optimised ℓ have a broader AID than textures made up from superpositions of different ℓ, if the rms roughness σ_r is kept constant. These results were confirmed by `ASA` simulations of the EQE and short circuit current. Further, the haze increases if σ_r increases. However, a combination of optimised ℓ and high σ_r may lead to sharp spikes that deteriorate the solar cell. Modulated surface textures are a way to overcome this problem by combining textures with large ℓ and σ_r with textures with optimised small ℓ. Such textures have a high haze and strong forward scattering. However, scattering into large angles is mainly controlled by the small features and cannot be increased with the MST concept.

Too many fragments of the spirit have I scattered in these streets, and too many are the children of my longing that walk naked among these hills, and I cannot draw from them without a burden and an ache.

Khalil Gibran

9 Conclusions and Outlook

9.1. Conclusions

Thin-film silicon solar cells contain nano-textured interfaces that scatter the incident light. This scattering leads to an increased average photon-path length in the absorber layer of the solar cell and thus to increased absorption. Therefore more light can be converted into electricity.

In this thesis we developed a scattering model to predict how light is scattered at nano-textured surfaces. The major achievements of our work are:

- We developed a model based on the scalar scattering theory that is able to predict two far field scattering properties, *i.e.* the angular intensity distribution and the haze, for both transmission and reflection. This model is based on the fact that the transmitted field directly behind the texture is related to the scattering object with Fourier transforms. The model uses easy assumptions to calculate the field behind the texture. We further have shown that the model works for interfaces created between different materials.
- The model also allows to get first estimations for the scattering properties at oblique incidence. However, in this case the deviations between measured and simulated values are larger. These deviations probably are due to the vector-character of light that becomes more important at oblique incidence, but is neglected by the scalar scattering theory.
- We showed that the scattering model combined with the `ASA` opto-electrical device simulator is able to predict the effect of nano-textures onto the external parameters of thin-film silicon solar cells. It is therefore possible to

estimate the effect of nano-textures on the solar cell performance by only using an AFM scan and the $n, \tilde{k}$ data of the materials surrounding the interface as input.

- An optimisation procedure allowed us to study how to optimise nano-textures. This optimisation revealed that the lateral feature size of the nano-texture is crucial for scattering into wide angles. Scattering into wide angles is crucial if the optical path length should be increased. We further could show that the vertical feature size has hardly any effect on the shape of the AID, but strongly influences the haze. If the rms roughness of the nano-textures is kept constant, a nano-texture with an optimal lateral feature size is preferable to a nano-texture that is obtained as superposition of different lateral feature sizes.

9.2. Recommendations

In contrast to Autumn 2008, when the work on this thesis started, we are now able to predict the AID and haze of nano-textured surfaces very accurately. However, several questions have not been answered in this thesis and are an important topic for future research:

- In Chapter 6 we saw that the scalar scattering theory shows weaknesses in predicting the scattering properties at oblique incidence. It might therefore be important to reformulate the scattering model as a vector model that takes the polarisation of the light into account more accurately.
- The far field approaches investigated in this thesis show their weaknesses when the layers become thinner than the wavelength, since near-field optics becomes important. Further, for very rough layers the approach performed in Chapter 7, *i.e.* assuming the the solar cell consists of flat layers with rough interfaces in between, becomes questionable. It therefore is very interesting to study how these shortcomings can be resolved.
- In the scattering model we assumed that the total reflectance R and transmittance T of the interface do not change when the interface is made rough. It is an important question how the real changes of R and T can be modelled. For example, effective medium approximations could be used [147]. Due to the large number of parameters in this approach it should be easily possible to find a model that fits well. However, the physical significance of such a multi-parameter model is questionable.
- In Chapter 8 we mentioned that nano-textures with small lateral features and high vertical features might be very good light scatterers but may have a detrimental effect on the electrical properties of the solar cells. It is thus important to investigate how the influence of the nano-textures on the electrical properties can be predicted.

A

Normalising the AID by using a fitting function

In Section 5.6 we compared AIDs obtained from various approaches. To be able to perform this comparison, two measures have to be taken. First, we do not plot the AID but the AID$\cdot \sin\theta$, which corresponds to the intensity that is scattered into the *ring* corresponding to the scattering angle θ. Contrary to the AID, which has its maximum at $\theta = 0°$, AID$\cdot \sin\theta$ peaks at larger angles. The position of this peak indicates how strongly the light is scattered away from the specular direction. Secondly, we normalise this peak to 1. The AID from several approaches is zigzag-like, as can be seen in Figs. 5.9 and 5.10. Fitting the highest point of the zigzag-like data to 1 does not allow a good comparison of the different AIDs. We therefore fit a function to the data. Subsequently we scale the data such that the peak of the fitting function is at 1. As fitting function we can use

$$f(\theta) = \frac{a}{\tan\theta} \exp\left[-\frac{1}{2}\left(\frac{\ln(\tan\theta) - b}{c}\right)^2\right] \tag{A.1}$$

with the fitting parameters a, b and c. This function resembles the log-normal distribution [148] with the difference that θ was substituted by $\tan\theta$. This substitution is performed in order to ensure that $f(\theta) \to 0$ at 0° and 90° as this is the case for AID$\cdot \sin\theta$. The function $f(\theta)$ takes its maximum $f_{\max}(\theta) = a \cdot \exp(0.5\,c^2 - b)$ at $\tan\theta_{\max} = \exp(b - c^2)$. Figure A.1 shows, as an example, $f(\theta)$ fitted to AID$\cdot \sin\theta$ inside the silicon layer as obtained by FDTD.

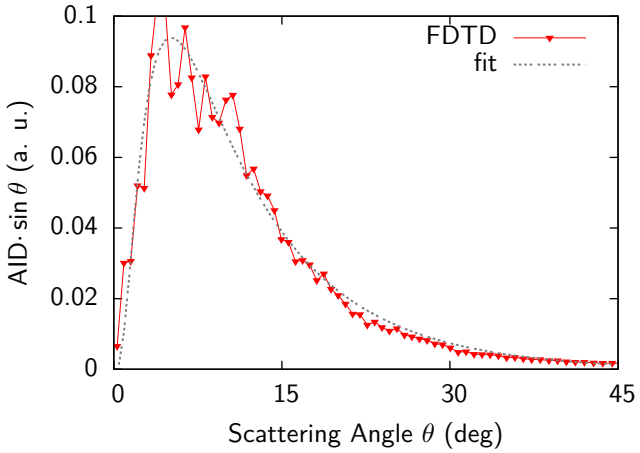

Figure A.1.: The function $f(\theta)$ [Eq. (A.1)] fitted to AID$\cdot \sin\theta$ inside the silicon layer as obtained by FDTD.

B

Smoothing with Bézier curves

In Chapters 4, 5 and 6 we smoothened the simulated AIDs with Bézier curves. In this appendix we discuss their mathematical and historical background.

In the 1960s, Pierre Bézier, a mechanical engineer at the French automaker Renault, searched for a method to describe geometrical shapes such that they could be communicated to all departments involved in the production of a car in an easy and exact way [149, 150]. He finally reached this goal by defining the points P_0 and P_N at which the curve starts and ends, respectively, and the *Bézier points* $P_1, \ldots, P_{N-1}$ that govern the shape of the curve. In particular, a Bézier curve of degree N is defined as polynomial of degree N,

$$\mathbf{B}(t) = \sum_{i=0}^{N} \binom{N}{i} (1-t)^{N-i} t^i \mathbf{P}_i, \tag{B.1}$$

where $t \in [0, 1]$. The binomial $\binom{N}{i}$ is defined as

$$\binom{N}{i} = \frac{N!}{i! \cdot (N-i)!}. \tag{B.2}$$

To elude the construction of Bézier curves, we will discuss the construction of a quadratic $(N = 2)$ and a cubic $(N = 3)$ curve in more detail. Figure B.1 (a) shows the construction of a quadratic Bézier curve in detail. Between the points $\mathbf{P}_0$ and $\mathbf{P}_1$ the linear Bézier curve $\mathbf{s}_{01}$ is defined as

$$\mathbf{s}_{01}(t) = \mathbf{P}_0 + t(\mathbf{P}_1 - \mathbf{P}_0). \tag{B.3}$$

Similar the linear curve $\mathbf{s}_{12}$ is defined as

$$\mathbf{s}_{12}(t) = \mathbf{P}_1 + t(\mathbf{P}_2 - \mathbf{P}_1). \tag{B.4}$$

The quadratic Bézier curve between $\mathbf{P}_0$ and $\mathbf{P}_2$ with the Bézier point $\mathbf{P}_1$ is then given by

$$\mathbf{B}(t) = \mathbf{s}_{01}(t) + t[\mathbf{s}_{12}(t) - \mathbf{s}_{01}(t)]. \tag{B.5}$$

A cubic Bézier curve is constructed analogously, as shown in Fig. B.1 (b). Starting with the linear curves $\mathbf{s}_{01}$, $\mathbf{s}_{12}$ and $\mathbf{s}_{23}$, quadratic curves are constructed with

$$\mathbf{q}_1(t) = \mathbf{s}_{01}(t) + t[\mathbf{s}_{12}(t) - \mathbf{s}_{01}(t)], \tag{B.6a}$$
$$\mathbf{q}_2(t) = \mathbf{s}_{12}(t) + t[\mathbf{s}_{23}(t) - \mathbf{s}_{12}(t)]. \tag{B.6b}$$

The cubic Bézier curve between $\mathbf{P}_0$ and $\mathbf{P}_3$ with the Bézier points $\mathbf{P}_1$ and $\mathbf{P}_2$ is then given by

$$\mathbf{B}(t) = \mathbf{q}_1(t) + t[\mathbf{q}_2(t) - \mathbf{q}_1(t)]. \tag{B.7}$$

To smooth the AID curves in Chapters 4, 5 and 6, we used the program `gnuplot` [151]. For smoothing of a set of N datapoints, a Bézier curve of degree N is constructed, which starts at the first point and ends at the last point. The other points are used as Bézier points. Figure B.2 shows the raw data and smoothed Bézier curves of two different AIDs. As we can see, the smoothed curves run nicely through the raw data.

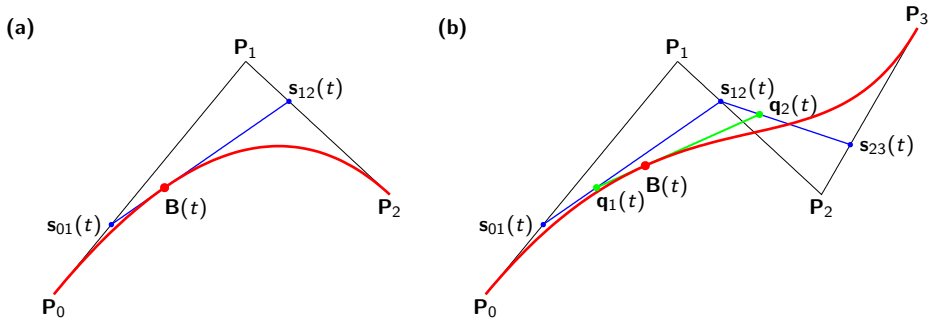

Figure B.1.: Illustrating the construction of (a) a quadratic Bézier curve and (b) a cubic Bézier curve. In the figure, the points $\mathbf{s}_{ij}$, $\mathbf{q}_i$ and $\mathbf{B}$ are shown for the parameter value $t = 0.3$.

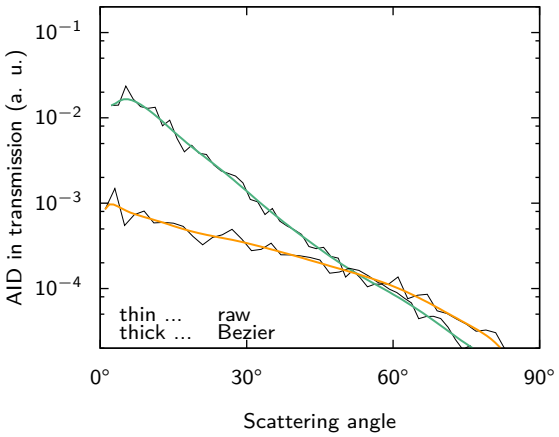

Figure B.2.: Raw calculation data and smoothed Bézier curves of two different AIDs.

C

The scattering program

In this appendix we briefly discuss the structure of `fourier_1.0`, the final version of the scattering program that we used to generate the AID and haze files for this project. In Section C.1 we discuss the directory structure of the program and the used input files. In Section C.2 we discuss the structure of the program itself.

C.1. Directory structure and input files

Figure C.1 shows the directory structure of the main directory. The directories `/morphology` and `/refractive` contain the input AFM pictures and the files with the $n, \tilde{k}$ data of the used materials, respectively. The morphology files are `ASCII` files as they are exported from Gwyddion with a four-line header [146]. The directory `/lib` contains two libraries: `fttw++_1.03` contains the implementions of the FFTW library for C++, as described in more detail in Appendix D. The library `r1279` is an implementation of the `r1279` pseudo-random number generator [152]. It was used for the optimizations done in Chapter 8.

The program files are located in directory `fourier_1.0`. Beside the program files, that are discussed in Section C.2, this directory contains several input files and the directory `/results`:

- `filelist.txt`: An example of this file is shown in Table C.1. This file contains the names of the files that are treated in one run. The two integer numbers following the filename assign the two materials between which the interface is created, as they are defined in the file `materials.txt`. The first of the two numbers is assigned to the material through which the light

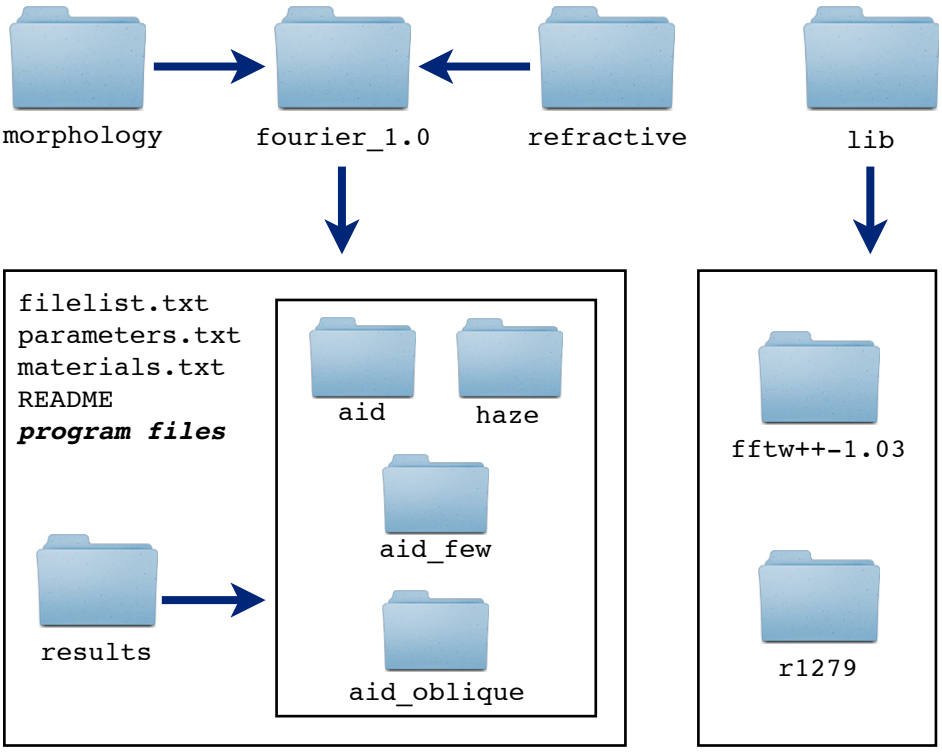

Figure C.1.: The directory structure of the program `fourier_1.0`.

Table C.1.: An example of the file `filelist.txt`.

```
M3_00_090420.txt 3 0
Asahi_090414.txt 1 0
L671_20_090326.txt 2 0
L671_40_090414.txt 2 0
exit 0
```

Table C.2.: An example of the file `parameters.txt`.

```
wavelength_start 3.e-7
wavelength_stop 10.e-7
wavelength_step 1.e-8
angle_in 0
angle_intervals 45
gwyd_resolution 256
arta_scale 70
```

impinges on the interface. The material files are stored in the directory `/morphology`. The last line must be `exit 0`.

- `parameters.txt`: This file contains the parameters that are needed to run the program. A sample file is shown in Table C.2. The first two lines specify the minimum and maximum wavelengths for which the calculation should be done. In the third line, the interval between two wavelength steps is defined. The incident angle of light *in vacuo* is defined with the parameter `angle_in`. The parameter `angle_intervals` defines the angular resolution of the the AID. The resolution of the input AFM height profile is specified with the parameter `gwyd_resolution`. To be able to compare the calculated AID with measured values, it has to be multiplied by the factor given in `arta_scale`.

- `materials.txt`: This file is depicted in Table C.3. It assigns the material codes used in `filelist.txt` to files with $n, \tilde{k}$-data. These files are stored in the directory `/refractive`.

- `/results`: This directory contains four sub-directories. In the directories `/aid` and `/haze` the result files are stored such that they can be used as input for `ASA` directly. Their input format is specified in more detail in the `ASA` manual [153]. In the directory `/aid_few`, the AID is given for 450, 600 and 750 nm. These files were used to produce the AID-graphs throughout this thesis but are only used for normal incidence. For oblique incidence, as discussed in Chapter 6, the results are found in the directory `/aid_oblique`.

Table C.3.: An example of the file `materials.txt`.

#	MAT_FILE	NAME
0	null	vacuum
1	fto_sap.nk	SnO2:F_AGC
2	azo_sap.nk	ZnO:Al_TUD
3	bzo_epfl.nk	ZnO:B_EPFL
4	tud_i-aSi.nk	a-Si:H_TUD
5	azo_L1467.nk	ZnO:Al_TUD_Sep_2010
6	azo_juelich.nk	ZnO:Al_FZJ
7	uc_Si_Juelich.nk	uc-Si:H_FZJ
8	tud_ag.nk	Silver_TUD
9	ag_palik.nk	Silver_Palik
10	azo_L1730.nk	ZnO:Al_TUD_Feb_2011
11	L1936.nk	ZnO:Al_TUD_Jul_2011
12	a5471.nk	a-Si:H_TUD_May_2011
13	tud_al.nk	AluminIum_TUD
14	bzo_1-9.nk	ZnO:B_1-9
15	bzo_1-8.nk	ZnO:B_1-8
16	bzo_1-7.nk	ZnO:B_1-7
17	end.	

C.2. Program structure

The program files are summarized in Table C.4.

- `main.cpp`: The main program.
- `bornapprox.cpp` and `.h`: The function `approx` to calculate the AID and haze. This function is described in detail in Appendix D.
- `bornfunctions.cpp` and `.h` contain many little routines that are used during the calculation.
- `interface.cpp` and `.h`: Here, the class `Interface` is defined, which contains amongst others the morphology of the interface and the two materials between which the interface is formed. Furthermore this class allows calculating statistical parameters. It contains the output-file names as strings.
- `init_fin.cpp` and `.h`: These files contain the functions `initialize` and `finalize`. In `initialize`, the file `parameters.txt` is read. Further the number of files in `filelist.txt` before the line `exit 0` are counted. In `finalize` the data are written in the output files.
- `scatter.cpp` and `.h`: Here, the class `ScatterPar` is defined that is used to store the AID and haze data.

Table C.4.: The program files used in `fourier_1.0`.

`main.cpp`	
`bornapprox.cpp`	`bornapprox.h`
`bornfunctions.cpp`	`bornfunctions.h`
`interface.cpp`	`interface.h`
`init_fin.cpp`	`init_fin.h`
`scatter.cpp`	`scatter.h`
	`init_par.h`
	`mathphysconst.h`

- `init_par.h`: The structure `InitPar` in which the data from `parameters.txt` are stored.
- `mathphysconst.h`: Some mathematical and physical constants.

Talk is cheap. Show me the code.

Linus Torvalds

D
The C++ scattering function

In Appendix C we discussed the structure of the scattering program that we used to perform the calculations with the scattering model presented in Chapters 4, 5 and 6. In this appendix we discuss the structure of the `C++` function `approx` that contains the core of the program:

First, the program has to be initialised by calling the necessary libraries:

```
//THIS IS FILE bornapprox.cpp

#include "mathphysconst.h"
#include "Array.h"
#include "fftw++.h"
#include "bornfunctions.h"

using namespace std;
using Array::array2;

void approx(string model, double* refr_mat1, double* refr_mat2,
  int gwyd_rsltn, int nu, double arta_scale, double angle_in, double
  wavelength_vac, double size, double** height, double* angle_out,
  double* aid, double* aid_cal, double& haze, double* angle_out_oblique,
  double* aid_oblique){
```

The first step in the actual course of the program is initialising the Fourier transform. Here several constants like the wavenumber are defined. `Nx` and `Ny` are the line- and row-number of the input AFM file, respectively. The `array` class that we use here was developed by Bowman [154]. Then the incident angle `angle_in` given *in vacuo* is used to calculate the angles in materials 1 and 2. Finally, the

reflection and transmission of a flat interface between these two materials is calculated. For normal incidence, the complex refractive index is used. For oblique incidence, only the real part of the refractive index is taken into account.

```
// Initialize the fourier transform
complex<double> imunit(0.0, 1.0);
double wavenumber_vac = 2*PI/wavelength_vac;
double wavenumber_mat1 = wavenumber_vac*refr_mat1[0];
double wavenumber_mat2 = wavenumber_vac*refr_mat2[0];
const unsigned int Nx = gwyd_rsltn, Ny = gwyd_rsltn;
const unsigned int Nyp=Ny/2+1;
size_t align=sizeof(Complex);

array2<double> h1(Nx,Ny,align), k(Nx, Ny, align);
array2<Complex> g(Nx,Ny,align);

// Calculate angles of incidence and refration in rad
  (angle_in always is the angle in air)

double angle_air, angle1, angle2;
angle_air = angle_in*PI/180.;
angle1 = snellius(angle_air, 1.0, refr_mat1[0]);
angle2 = snellius(angle_air, 1.0, refr_mat2[0]);

// Caculcate R and T (for flat interface, with real refractive index
  for oblique incidence and complex refractive index otherwise)
double R_0, T_0;
if (angle_in != 0){
  R_0 = reflectivity(angle1, refr_mat1[0], refr_mat2[0]);
  T_0 = transmissivity(angle1, refr_mat1[0], refr_mat2[0]);
  }
else{
  R_0 = refl_complex(refr_mat1, refr_mat2);
  T_0 = trans_complex(refr_mat1, refr_mat2);
  }
```

Here, the pupil functions are calculated according to Eqs. (6.9) [`model == "phase"`] or (6.6) [`model == "refl"`]. For normal incidence, these equations reduce to Eqs. (5.14b) and (5.14c).*

```
// The phase shift is used as exponent
double phase_shift;

if (model == "trans")
  for (unsigned int i = 0; i < Nx; i++)
    for (unsigned int j = 0; j < Ny; j++){
      phase_shift = wavenumber_vac*height[i][j]*(refr_mat1[0]-refr_mat2[0])
```

*In earlier versions of the program also Eqs. (5.14a) and (6.4) were implemented. They are now omitted due to their bad performance as discussed in Chapters 5 and 6.

```
        /(.5*(cos(angle1)+cos(angle2)));
      g(i,j)  = cos(phase_shift);
      g(i,j) += imunit*sin(phase_shift);
      g(i,j) *= sqrt(T_0)/Nx;
      }
else if (model == "refl")
  for (unsigned int i = 0; i < Nx; i++)
    for (unsigned int j = 0; j < Ny; j++){
      phase_shift = wavenumber_vac*height[i][j]*2.*refr_mat1[0]
        /cos(angle1);
      g(i,j)  = cos(phase_shift);
      g(i,j) += imunit*sin(phase_shift);
      g(i,j) *= sqrt(R_0)/Nx;
      }
else{
  cerr << "Requested model not known, STOP." << endl;
  exit(1);
  }
```

Here the fast Fourier transform is actually performed. We used the `FFTW` library, developed by Frigo and Johnson [103].

```
// First order 3D FFT approximation

fft2d Forward(-1,g);
Forward.fft(g);
```

The angles are related to the field in k-space according to Eq. (4.30), which contains the coordinates K_x and K_y in k-space. The FFT, however, maps a $N \times N$ array to an $N \times N$ array, but does not give the vectors of the points of the array. We therefore have to calculate them. The reciprocal distance between two points in k-space is given by $2\pi/D$, *i.e.* the reciprocal of the side length D of the AFM scan. Therefore, a point (p, q) on the array corresponds to the vector $2\pi/D \cdot (p, q)$. The reciprocal distance to $(0, 0)$ is then given by

$$K(p, q) = \frac{2\pi}{D}\sqrt{p^2 + q^2}. \tag{D.1}$$

According to this equation, the K-values are assigned to elements of the array `k(i,j)`. The (i, j) pairs correspond to the (p, q) pairs as illustrated in Fig. D.1.

```
// Assign k values to FFT points
// 1st quadrant
for (unsigned int j=0; j < Nyp; j++){
  for(unsigned int i=0; i < Nyp; i++)
    k(i,j) = k_vec(i, j, size);
// 2nd quadrant
  for(unsigned int i= Nyp; i < Nx; i++)
    k(i,j) = k_vec((Nx-i), j, size);
```

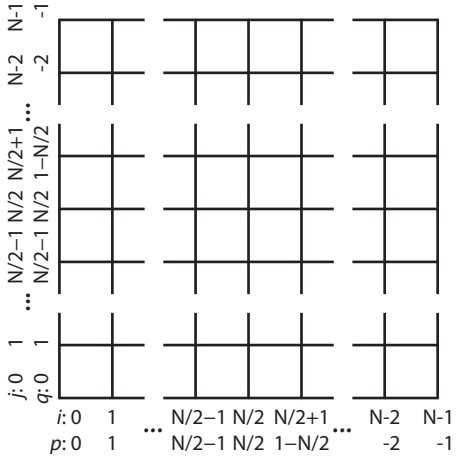

Figure D.1.: Illustrating the relation between the points (p, q) and (i, j) for calculating the k-vectors, if N is even.

```
  }
for (unsigned int j=Nyp; j < Ny; j++){
// 3rd quadrant
  for(unsigned int i= 0; i < Nyp; i++)
    k(i,j) = k_vec(i, (Ny-j), size);
// 4th quadrant
  for(unsigned int i= Nyp; i < Nx; i++)
    k(i,j) = k_vec((Nx-i), (Ny-j), size);
  }
```

Now, the real array `h1(i,j)` is determined as the absolute value of the complex array `g(i,j)` that was the output of the FFT. Further, the field is normalised.

```
// Normalize FFT and calculate absolute value [Nx = sqrt(Nx*Ny)]
for (unsigned int i=0; i < Nx; i++)
  for(unsigned int j=0; j < Ny; j++)
    h1(i,j) = abs(g(i,j))/Nx;
```

To determine the AID at an angle θ, we average the squared field `h1*h1` over all angles inside an angle interval $(\theta - \Delta\theta, \theta + \Delta\theta)$, according to Eq. (5.21). Before we can start we have to determine the shift in k-space at non-normal incidence. To increase the sampling size, we apply this shift in negative and positive K_x and K_y directions when summing up the AID.

```
// Now we can start to extract AID and haze
// this k_shift is true for both materials since n*sin(angle) is
  an invariant
int k_shift = k_index(wavenumber_mat1*sin(angle1), size);
int i_pos_shift, i_neg_shift, j_pos_shift, j_neg_shift;
```

```
// Average over the values to obtain AID
double angle_int, angle_small, k_small, angle_large, k_large, sum;
double aid_tot = 0.0;
int counter;
angle_int = 0.5*PI/nu;
for (int p = 0; p < nu; p++){
  angle_small = angle_int*p;

  angle_large = angle_int*(p+1);
  if (model == "refl"){
    k_small = wavenumber_mat1*sin(angle_small);
    k_large = wavenumber_mat1*sin(angle_large);
  }
  else{
    k_small = wavenumber_mat2*sin(angle_small);
    k_large = wavenumber_mat2*sin(angle_large);
  }
  sum = 0.0;
  counter = 0;
  for (unsigned int i=0; i < Nx; i++)
    for(unsigned int j=0; j < Ny; j++){
        i_pos_shift = (i+k_shift+Nx)%Nx;
        i_neg_shift = (i+k_shift+Nx)%Nx;
        j_pos_shift = (j+k_shift+Ny)%Ny;
        j_neg_shift = (j+k_shift+Ny)%Ny;
        // to exclude (0,0) component from evaluation
        if ((((i_pos_shift == 0) or (i_neg_shift == 0)) and (j == 0))
          or ((i == 0) and ((j_pos_shift == 0) or (j_neg_shift == 0))))
          continue;
        if ((k(i,j) > k_small) && (k(i,j) < k_large)){
          sum += .25*h1(i_pos_shift,j)*h1(i_pos_shift,j);
          sum += .25*h1(i_neg_shift,j)*h1(i_neg_shift,j);
          sum += .25*h1(i,j_pos_shift)*h1(i,j_pos_shift);
          sum += .25*h1(i,j_neg_shift)*h1(i,j_neg_shift);
          counter++;
          }
        }

  angle_out[p] = 90./nu*(0.5+p);
```

Now the AID can be determined. We determine two different values: First, `aid_cal` is the AID as it would be measured with the ARTA [see Section 3.4]. Secondly, `aid` is the AID as it is used in `ASA`. It is `aid_cal` multiplied with a sine. We further sum up all the AIDs in `aid_tot`, as we need it for normalisation in the end. This summation is done by

$$\mathrm{AID}_{\mathrm{tot}} = \sum_{\theta} \mathrm{AID}(\theta) \cdot \Omega_{\mathcal{R}(\theta)}, \tag{D.2}$$

where $\Omega_{\mathcal{R}(\theta)}$ is the solid angle covered by the ring $\mathcal{R}(\theta)$ as defined in Eq. (3.18).

```
  aid[p]  = 0;
  aid_cal[p] = sqrt(-1);
  if (counter != 0){
    aid[p]  = sum/counter;
    aid[p] *= cos(angle_int*(0.5+p));
    if (model != "refl")
      aid_cal[p] = aid[p];
    else if (refr_mat1[0] == 1.0)
      aid_cal[p] = aid[p];
    // Calculate AID for solid angle by multiplying with sine
    aid[p] *= sin(angle_int*(0.5+p));
    aid_tot += aid[p]*4.0*PI*sin(0.5*angle_int);
    }
  }
```

Here, we correct the AID_R for measuring from the glass side. We applied this correction in Section 5.7.

```
//Calculate AID in R corrected for measuring through glass
if ((model == "refl") && (refr_mat1[0] != 1.0)){
  double angle_tco_rad;
  for (int p = 0; p < nu; p++){
    angle_small = angle_int*p;
    angle_large = angle_int*(p+1);
    k_small = wavenumber_vac*sin(angle_small);
    k_large = wavenumber_vac*sin(angle_large);
    sum = 0.0;
    counter = 0;
    for (unsigned int i=0; i < Nx; i++)
      for(unsigned int j=0; j < Ny; j++)
        if ((k(i,j) > k_small) && (k(i,j) < k_large)){
          sum += h1(i,j)*h1(i,j);
          counter++;
          }
    // angle that has to be considered in mat1
    angle_tco_rad = snellius(angle_int*(0.5+p),1.0, refr_mat1[0]);
    aid_cal[p]  = sqrt(-1);
    if (counter != 0){
      aid_cal[p]  = sum/counter;
      aid_cal[p] *= cos(angle_tco_rad);
      aid_cal[p] *= transmissivity_back_refl(angle_out[p]*PI/180.,
        refr_mat1[0]);
    }
  }
}
```

For evaluating the model at oblique incidence we cannot use the summation in rings as done before, but we have to calculate it along axes in k-space. This in-

creases the noise, which can be reduced by taking the average of more AFM input files. As before, we apply the shift in k-space in negative and positive K_x and K_y directions when summing up the AID.

```
//Calculate AID in transmission along axes (for evaluation)
double wavenumber_eval;
if (model == "refl")
  wavenumber_eval = wavenumber_mat1;
else
  wavenumber_eval = wavenumber_mat2;
for (unsigned int i=0; i < Nx/2; i++)
  angle_out_oblique[i] = asin(k(i,0)/wavenumber_eval);
for (unsigned int i=Nx/2; i < Nx; i++)
  angle_out_oblique[i] = -1*asin(k(i,0)/wavenumber_eval);
for (unsigned int i=1; i < Nx; i++){
  i_pos_shift = (i+k_shift+Nx)%Nx;
  i_neg_shift = (-i-k_shift+2*Nx)%Nx;
  aid_oblique[i]  = .25*h1(i_pos_shift,0)*h1(i_pos_shift,0);
  aid_oblique[i] += .25*h1(i_neg_shift,0)*h1(i_neg_shift,0);
  aid_oblique[i] += .25*h1(0,i_pos_shift)*h1(0,i_pos_shift);
  aid_oblique[i] += .25*h1(0,i_neg_shift)*h1(0,i_neg_shift);
  aid_oblique[i] *= cos(angle_out_oblique[i]);
  angle_out_oblique[i] *= 180/PI;
  }
```

Here, the haze is calculated according to Eq. (5.22).

```
//Calculate haze
double tot = 0.0;
double tot_full = 0.0;
double wavenumber_max;

if  (model == "refl")
  wavenumber_max = wavenumber_mat1;
else
  wavenumber_max = wavenumber_mat2;

for (unsigned int i=0; i < Nx; i++)
  for(unsigned int j=0; j < Ny; j++){
    tot_full += h1(i,j)*h1(i,j);
    if (k(i,j) < wavenumber_max){
      i_pos_shift = (i+k_shift+Nx)%Nx;
      i_neg_shift = (i-k_shift+Nx)%Nx;
      j_pos_shift = (j+k_shift+Ny)%Ny;
      j_neg_shift = (j-k_shift+Ny)%Ny;
      tot += .25*h1(i_pos_shift,j)*h1(i_pos_shift,j);
      tot += .25*h1(i_neg_shift,j)*h1(i_neg_shift,j);
      tot += .25*h1(i,j_pos_shift)*h1(i,j_pos_shift);
      tot += .25*h1(i,j_neg_shift)*h1(i,j_neg_shift);
```

```
      }
    }

haze  = (tot-h1(0,0)*h1(0,0));
haze /= tot;
//to avoid haze = nan
if ((refr_mat1[0]/refr_mat2[0]*sin(angle1) > 1.) and (model != "refl"))
  haze = 0.0;
```

Finally, the AID is normalised according to Harvey [107]. This is done by

$$\texttt{corr\_fac} = \frac{\Xi_{\text{dif}}}{\text{AID}_{\text{tot}}} = \frac{H_{\Xi} \cdot \Xi_{\text{tot}}}{\text{AID}_{\text{tot}}}, \tag{D.3}$$

where Ξ stands for either R or T. We note that AID_{tot} does not contain the $(0,0)$ component, *i.e.* it corresponds to the scattered light. The `aid_cal` is further multiplied by a factor `arta_scale` that is dependent on the ARTA setup.

```
// normalize the AID determine dif
double corr_fac = haze*tot_full/aid_tot;
double corr_fac_cal = corr_fac/arta_scale;
for (unsigned int i = 0; i < Nx; i++)
  aid_oblique[i] *= corr_fac_cal;
tot = tot_full;
for (int p = 0; p < nu; p++){
  aid[p] *= corr_fac;
  aid_cal[p] *= corr_fac_cal;
  // to avoid AID = nan due to T = 0
  if ((refr_mat1[0]/refr_mat2[0]*sin(angle1) > 1.)
    and (model != "refl")){
    aid[p] = 0.;
    aid_cal[p]=0.;
    }
  }
return;
}
```

E

Choosing suitable size and resolution of the AFM input file

During the derivation of the scattering model in Section 5.3 we saw that only k-vectors with a norm smaller than $k_0 n$ contribute to the scattered field [Eq. (5.16)],

$$K_x^2 + K_y^2 < k_0^2 n^2. \tag{E.1}$$

K_x and K_y are the vectors in k-space, λ_0 and $k_0 = 2\pi/\lambda_0$ are the wavelength and the wavenumber of light *in vacuo*, respectively, and n is the refractive index of the material into which the light is scattered.*

As input for the scattering model AFM files are used. These files consist of an $N \times N$ array of data points taken from a square with side length D. In the fast Fourier transforms that we use to calculate the field U [Eqs. (5.13a) and (5.13b)] the $N \times N$ array is transformed to another $N \times N$ array. The distance between neighbours in this array in k-space is

$$k_{\min} = \frac{2\pi}{D}, \tag{E.2}$$

i.e. the density of points in k-space is solely defined by the AFM scan size D.

The array in k-space is centered around $(K_x, K_y) = (0, 0)$. The biggest circle that fits into this array therefore has the radius

$$k_{\max} = \frac{2\pi}{D}\left(\frac{N}{2} - 1\right). \tag{E.3}$$

*For this discussion it is of no importance whether the light is transmitted or reflected.

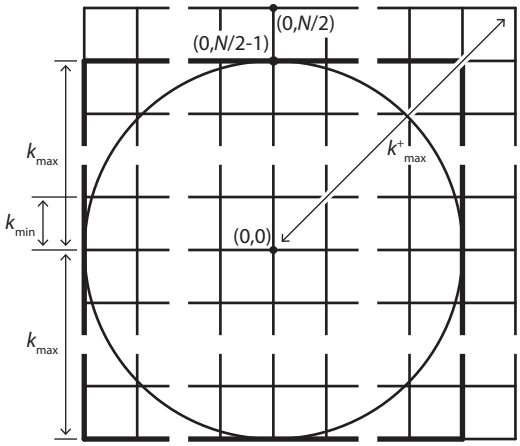

Figure E.1.: Illustrating the distances $k_{\min}$, $k_{\max}$ and $k^{+}_{\max}$ in k-space, when N is even.

The $N/2-1$ comes from the fact that we only use arrays, where N is even, as illustrated in Fig. E.1. The outhermost corner point in the array corresponds to the k-number

$$k^{+}_{\max} = \frac{2\pi}{D}\frac{N}{2}\sqrt{2} = \frac{\sqrt{2}\pi N}{D}. \tag{E.4}$$

We note two important properties of the k-space:

1. Changing the resolution of the AFM scan does not change the density of points but the area covered in k-space.
2. Changing both the AFM scan size and the resolution at the same rate does not change the area covered in k-space but changes the resolution.

To investigate which combinations of D and N are suited for calculating the scattering parameters, we first look at the wavenumbers of several λ_0-n combinations, shown in Table E.1. Table E.2 shows $k_{\min}$ and $k_{\max}$ for several combinations of D and N. Table E.2 further shows the absolute and relative number of used points $\#_{\text{abs}}$ and $\#_{\text{rel}}$, respectively, in the k-space array for several combinations of λ_0 and n. $\#_{\text{abs}}$ was approximated by

$$\#_{\text{abs}} \approx \frac{k_0^2 n^2 \pi}{k_{\min}^2} = \pi\left(\frac{Dn}{\lambda_0}\right)^2 \tag{E.5}$$

and $\#_{\text{rel}}$ is given by

$$\#_{\text{rel}} = \frac{\#_{\text{abs}}}{N^2}. \tag{E.6}$$

A high $\#_{\text{abs}}$ is important for obtaining smooth results. For scattering into air the combination $D = 20$ µm, $N = 256$ shows both the highest absolute and relative #. However, for scattering into silicon ($n \approx 4$), the resolution is not high

Table E.1.: Wavenumbers $k_0 n$ (in m^{-1}) of different λ_0-n combinations.

n \ λ_0	**300 nm**	**1 200 nm**
1	$2.09 \cdot 10^7$	$5.24 \cdot 10^6$
2	$4.19 \cdot 10^7$	$1.05 \cdot 10^7$
4	$8.38 \cdot 10^7$	$2.09 \cdot 10^7$

Table E.2.: The parameters k_{min} and k_{max} dependent on D and N. Absolute and relative number # of used points in the k-space array dependent on D, N, λ_0, and n.

D	N	k_{min}	k_{max}	n	λ_0 =**300 nm**		λ_0 =**1 200 nm**	
(µm)	**(–)**	**(m^{-1})**	**(m^{-1})**	**(–)**	**$\#_{abs}$**	**$\#_{rel}$**	**$\#_{abs}$**	**$\#_{rel}$**
10	256	$6.28 \cdot 10^5$	$7.98 \cdot 10^7$	1	3 491	5.3%	218	0.3%
				4	55 851	85.2%	3 491	5.2%
10	512	$6.28 \cdot 10^5$	$1.60 \cdot 10^8$	1	3 491	1.3%	218	0.1%
				4	55 851	21.3%	3 491	1.3%
20	256	$3.14 \cdot 10^5$	$3.99 \cdot 10^7$	1	13 963	21.3%	873	1.3%
				4	223 402	340.9%	13 963	21.3%
20	512	$3.14 \cdot 10^5$	$8.01 \cdot 10^7$	1	13 963	5.3%	873	0.3%
				4	223 402	85.2%	13 963	5.3%

enough. Here $N = 512$ should be used. For $n = 4$, at 300 nm $k_0 n > k_{max}$. However, already at 320 nm $k_0 n < k_{max}$ is met again, which is sufficient for solar cell applications.

In Ref. [105], Fig. 10, we unfortunately used AFM scans with $D = 20$ µm and $N = 256$. Therefore for short wavelength $k_0 n > k_{max}$ for the light that was scattered into the silicon. At large angles, the AID thus was set to zero. The effect onto the haze in transmission in silicon is illustrated in Fig. E.2 for two ZnO:Al samples and one SnO_2:F sample. For the ZnO:Al samples the difference in haze is very small, for $N = 256$ the haze is slightly overestimated. For SnO_2:F the difference is bigger, because SnO_2:F scatters stronger into large angles than ZnO:Al.

For the calculations in Chapter 7 we generated AFM files with $N = 512$ from those with $N = 256$ through interpolation. We then could analyse the effect on the scattering parameters and the EQE. Luckily we found that the AID of the etched ZnO:Al decays sufficiently fast making the effect of the badly chosen N very small: The short-circuit current density for the cell with $\sigma_r = 35$ nm decreases by 0.7%, the one for the cell with $\sigma_r = 95$ nm by 0.8%. For cells on SnO_2:F, the effect is slightly bigger with 1.2%.

Recommendation

For the vast majority of solar-cell applications an AFM scan size of $D = 20$ µm and a resolution of $N = 512$ is optimal.

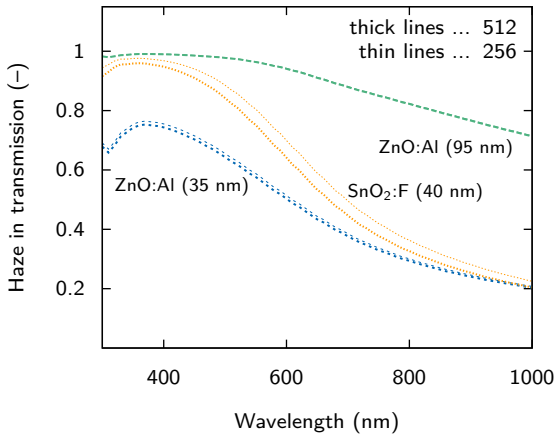

Figure E.2.: Illustrating the difference of calculating H_T in silicon with $N = 256$ (thin lines) and $N = 512$ (thick lines).

Bibliography

[1] G. Jones, Curr. Biol. **15**, R484 (2005).

[2] J. W. Strutt, Philos. Mag. (4) **41**, 107 (1871).

[3] C. Bohren and D. Huffman, *Absorption and scattering of light by small particles* (John Wiley & Sons, Inc., New York, NY, USA, 1983).

[4] E. Haeckel, *Kunstformen der Natur* (Bibliograph. Inst., Leipzig und Wien, 1904).

[5] B. Nienhuis, `commons.wikimedia.org/wiki/File:Droitwichtransmitter.jpg`.

[6] K. Jarolimek, Personal communication.

[7] H. Ibach and H. Lüth, *Solid-State Physics*, 4th ed. (Springer-Verlag, Berlin, Germany, 2009).

[8] H. W. Deckman, C. R. Wronski, H. Witzke, and E. Yablonovitch, Appl. Phys. Lett. **42**, 968 (1983).

[9] E. Yablonovitch, J. Opt. Soc. Am **72**, 899 (1982).

[10] M. Zeman, O. Isabella, K. Jäger, R. Santbergen, R. Liang, S. Solntsev, and J. Krč, MRS Proceedings **1245**, A03_03 (2010).

[11] M. A. Green, *Third Generation Photovoltaics*, edited by T. Kamiya, B. Monemar, H. Venghaus, and Y. Yamamoto, Springer Series in Photonics (Springer-Verlag, Berlin, Germany, 2003).

[12] W. Shockley and H. J. Queisser, J. Appl. Phys. **32**, 510 (1961).

[13] P. Würfel, *Physics of Solar Cells* (WILEY-VCH Verlag GmbH & Co. KGaA, Weinheim, Germany, 2005).

[14] G. Conibeer, Mater. Today **10**, 42 (2007).

[15] A. Einstein, Ann. Phys. (4) **322**, 891 (1905).

[16] D. Neamen, *Semiconductor Device Physics: Basic Principles*, 4th ed. (McGraw-Hill, New York, NY, USA, 2012).

[17] ASTM Standard G173-03, *Standard Tables for Reference Solar Spectral Irradiances: Direct Normal and Hemispherical on 37° Tilted Surface* (ASTM International, West Conshohocken, PA, USA, 2008).

[18] A. Jäger-Waldau, *PV Status Report 2011* (European Comission, Joint Research Centre, Institute for Energy, Ispra, VA, Italy, 2011).

[19] D. M. Chapin, C. S. Fuller, and G. L. Pearson, J. Appl. Phys. **25**, 676 (1954).

[20] M. A. Green, K. Emery, Y. Hishikawa, W. Warta, and E. D. Dunlop, Prog. Photovolt: Res. Appl. **20**, 606 (2012).

[21] K. L. Chopra, P. D. Paulson, and V. Dutta, Prog. Photovolt: Res. Appl. **12**, 69 (2004).

[22] "PHOTON module price index," 25 May 2012, `www.photon-international.com/newsletter/document/65647.pdf`.

[23] J. Poortmans and V. Arkhipov, eds., *Thin Film Solar Cells: Fabrication, Characterization and Applications* (John Wiley & Sons, Inc., Hoboken, NJ, USA, 2006).

[24] K. Bädeker, Ann. Phys. (4) **327**, 749 (1907).

[25] O. Kluth, *Texturierte Zinkoxidschichten für Silizium-Dünnschichtsolarzellen*, Ph.D. thesis, RWTH Aachen, Forschungszentrum Jülich, Germany (2001).

[26] P. Drude, Ann. Phys. (4) **306**, 566 (1900).

[27] N. W. Ashcroft and N. D. Mermin, *Solid State Physics, HRW International Editions* (Saunders College, Philadelphia, PA, USA, 1976).

[28] D. Mergel and Z. Qiao, J. Phys. D Appl. Phys. **35**, 794 (2002).

[29] F. Ruske, A. Pflug, V. Sittinger, B. Szyszka, D. Greiner, and B. Rech, Thin Solid Films **518**, 1289 (2009).

[30] J. Sap, O. Isabella, K. Jäger, and M. Zeman, Thin Solid Films **520**, 1096 (2011).

[31] E. Fortunato, D. Ginley, H. Hosono, and D. C. Paine, MRS Bull. **32**, 242 (2007).

[32] K. H. Wedepohl, Geochim. Cosmochim. Ac. **59**, 1217 (1995).

[33] R. A. Street, *Hydrogenated amorphous silicon* (Cambridge University Press, Cambridge, UK, 1991).

[34] D. E. Carlson and C. R. Wronski, Appl. Phys. Lett. **28**, 671 (1976).

[35] D. L. Staebler and C. R. Wronski, Appl. Phys. Lett. **31**, 292 (1977).

[36] N. Gupta, G. F. Alapatt, R. Podila, R. Singh, and K. F. Poole, Int. J. Photoenergy **2009**, 154059 (2009).

[37] S. N. Agbo, *Growth and Characterization of Thin Film Nanocrystalline Silicon Materials and Solar Cells*, Ph.D. thesis, Delft University of Technology, Delft, the Netherlands (2012).

[38] H. Binder, *Lexikon der chemischen Elemente* (Hirzel Verlag, Stuttgart, Germany, 1999).

[39] A. Tanaka, Toxicol. Appl. Pharm. **198**, 405 (2004).

[40] B. Unger, Opt. Photon. News **20**, Issue 9, 26 (2009).

[41] P. Jackson, D. Hariskos, E. Lotter, S. Paetel, R. Wuerz, R. Menner, W. Wischmann, and M. Powalla, Prog. Photovolt: Res. Appl. **19**, 894 (2011).

[42] A. Chirilă, S. Buecheler, F. Pianezzi, P. Bloesch, C. Gretener, A. Uhl, C. Fella, L. Kranz, J. Perrenoud, S. Seyrling, *et al.*, Nat. Mater. **10**, 857 (2011).

[43] T. Tinoco, C. Rincón, M. Quintero, and G. S. Pérez, Phys. Status Solidi A **124**, 427 (1991).

[44] The Economist, "Solar power: A painful eclipse," 15 October 2011.

[45] B. E. McCandless and J. R. Sites, *Handbook of Photovoltaic Science and Engineering*, edited by A. Luque and S. Hegedus (John Wiley & Sons, Ltd, Chichester, England, 2003) Chap. 14, Cadmium Telluride Solar Cells, p. 617.

[46] R. U. Ayres and L. Ayres, *A Handbook of Industrial Ecology* (Edward Elgar Publishing, Cheltenham, UK, 2002).

[47] J. Zayed and S. Philippe, Int. J. Toxicol. **28**, 259 (2009).

[48] B. Kippelen and J.-L. Bredas, Energy Environ. Sci. **2**, 251 (2009).

[49] B. O'Regan and M. Grätzel, Nature **353**, 737 (1991).

[50] J. Wu, Z. Lan, S. Hao, P. Li, J. Lin, M. Huang, L. Fang, and Y. Huang, Pure Appl. Chem. **80**, 2241 (2008).

[51] J. Chen, T. Peng, K. Fan, and J. Xia, J. Mater. Chem. **21**, 16448 (2011).

[52] A. Luque, P. G. Linares, E. Antolín, E. Cánovas, C. D. Farmer, C. R. Stanley, and A. Martí, Appl. Phys. Lett. **96**, 013501 (2010).

[53] J. de Wild, A. Meijerink, J. Rath, W. van Sark, and R. Schropp, Sol. Energ. Mat. Sol. C. **94**, 1919 (2010).

[54] T. Trupke, M. A. Green, and P. Würfel, J. Appl. Phys. **92**, 1668 (2002).

[55] K. Tanabe, Electron. Lett. **43**, 998 (2007).

[56] K. Bittkau, R. Carius, and C. Lienau, Phys. Rev. B **76**, 035330 (2007).

[57] K. Bittkau, T. Beckers, S. Fahr, C. Rockstuhl, F. Lederer, and R. Carius, Phys. Status Solidi A **205**, 2766 (2008).

[58] J. Krč, M. Zeman, F. Smole, and M. Topič, J. Appl. Phys. **92**, 749 (2002).

[59] J. Krč, M. Zeman, O. Kluth, F. Smole, and M. Topič, Thin Solid Films **426**, 296 (2003).

[60] D. Dominé, P. Buehlmann, J. Bailat, A. Billet, A. Feltrin, and C. Ballif, Phys. Status Solidi-R **2**, 163 (2008).

[61] M. Berginski, J. Hüpkes, W. Reetz, B. Rech, and M. Wuttig, Thin Solid Films **516**, 5836 (2007).

[62] J. Bennett and L. Mattsson, *Introduction to surface roughness and scattering* (Optical Society of America, Washington, DC, USA, 1989).

[63] W. Driscoll and W. Vaughan, *Handbook of Optics* (McGraw-Hill, New York, NY, USA, 1978).

[64] S. Schröder, T. Herffurth, H. Blaschke, and A. Duparré, Appl. Opt. **50**, C164 (2011).

[65] D. Dominé, F.-J. Haug, C. Battaglia, and C. Ballif, J. Appl. Phys. **107**, 044504 (2010).

[66] K. Bittkau, M. Schulte, T. Beckers, and R. Carius, Proc. SPIE **7725**, 77250N (2010).

[67] K. Bittkau, M. Schulte, M. Klein, T. Beckers, and R. Carius, Thin Solid Films **519**, 6538 (2011).

[68] K. Jäger, O. Isabella, L. Zhao, and M. Zeman, Phys. Status Solidi C **7**, 945 (2010).

[69] K. Jäger, O. Isabella, R. A. C. M. M. van Swaaij, and M. Zeman, Meas. Sci. Technol. **22**, 105601 (2011).

[70] K. Jäger, M. Schulte, K. Bittkau, M. Ermes, M. Zeman, and B. E. Pieters, Proc. SPIE **8001**, 800106 (2011).

[71] M. Schulte, K. Bittkau, K. Jäger, M. Ermes, M. Zeman, and B. E. Pieters, Appl. Phys. Lett. **99**, 111107 (2011).

[72] F. J. Giessibl, Rev. Mod. Phys. **75**, 949 (2003).

[73] *NT-MDT Catalogue on SPM Accessories*, Tech. Rep. (2012) `http://www.ntmdt-tips.com/data/media/nt-mdt_afm_probes_29_03_12.pdf`.

[74] P. Klapetek, *Characterization of randomly rough surfaces in nanometric scale using methods of modern metrology*, Ph.D. thesis, Masaryk University, Brno, Czech Republic (2003).

[75] K. Sato, Y. Gotoh, Y. Wakayama, Y. Hayashi, K. Adachi, and N. Nishimura, Rep. Res. Lab., Asahi Glass Co. Ltd. **42**, 129 (1992).

[76] O. Kluth, B. Rech, L. Houben, S. Wieder, G. Schöpe, C. Beneking, H. Wagner, A. Löffl, and H. Schock, Thin Solid Films **351**, 247 (1999).

[77] J. Springer, A. Poruba, M. Vanecek, S. Fay, L. Feitknecht, N. Wyrsch, J. Meier, A. Shah, T. Repmann, O. Kluth, H. Stiebig, and B. Rech, in *17th European Photovoltaic Solar Energy Conference* (Munich, Germany, 2001) p. 2830.

[78] G. T. Georgiev and J. J. Butler, Appl. Opt. **46**, 7892 (2007).

[79] R. Ulbricht, Electrotech. Z **21**, 595 (1900).

[80] J. A. Jacqez and H. F. Kuppenheim, J. Opt. Soc. Am. **45**, 460 (1955).

[81] A. Roos and C. G. Ribbing, Appl. Opt. **27**, 3833 (1988).

[82] A. M. Nilsson, A. Jonsson, J. C. Jonsson, and A. Roos, Appl. Opt. **50**, 999 (2011).

[83] H. Schade and Z. E. Smith, Appl. Opt. **24**, 3221 (1985).

[84] A. von Finck, M. Hauptvogel, and A. Duparré, Appl. Opt. **50**, C321 (2011).

[85] C. Amra, D. Torricini, and P. Roche, Appl. Opt. **32**, 5462 (1993).

[86] G. Serrot, M. Bodilis, X. Briottet, and H. Cosnefroy, Proc. SPIE **3494**, 34 (1998).

[87] W. Zhang, F. Wang, Z. Wang, and H. Wang, Proc. SPIE **7658**, 76582P (2010).

[88] P. A. van Nijnatten, Thin Solid Films **442**, 74 (2003).

[89] O. Isabella, A. Campa, M. C. R. Heijna, W. Soppe, R. van Erven, R. H. Franken, H. Borg, and M. Zeman, in *23rd European Photovoltaic Solar Energy Conference* (Valencia, Spain, 2008) p. 2320.

[90] T. Markvart, J. Opt. A-Pure Appl. Op. **10**, 015008 (2008).

[91] K. Yee, IEEE T. Antenn. Propag. **14**, 302 (1966).

[92] A. Taflove and S. C. Hagness, *Computational Electrodynamics: The Finite-Difference Time-Domain Method*, 3rd ed. (Artech House, Inc., Norwood, MA, USA, 2005).

[93] J. Jin, *The finite element method in electromagnetics* (John Wiley & Sons, Inc., New York, NY, USA, 2002).

[94] M. Born and E. Wolf, *Principles of optics*, 7th ed. (Cambridge University Press, Cambridge, UK, 1999).

[95] J. D. Jackson, *Classical Electrodynamics*, 3rd ed. (John Wiley & Sons, Inc., New York, NY, USA, 1999).

[96] H. Davies, Proc. Inst. Elec. Engrs. **101**, 209 (1954).

[97] H. E. Bennett and J. O. Porteus, J. Opt. Soc. Am. **51**, 123 (1961).

[98] C. K. Carniglia, Opt. Eng. **18**, 104 (1979).

[99] M. Zeman, R. A. C. M. M. van Swaaij, J. W. Metselaar, and R. E. I. Schropp, J. Appl. Phys. **88**, 6436 (2000).

[100] K. Jäger and M. Zeman, Appl. Phys. Lett. **95**, 171108 (2009).

[101] F. Simonetti, Phys. Rev. E **73**, 036619 (2006).

[102] J. Cooley and J. Tukey, Math. Comput. **19**, 297 (1965).

[103] M. Frigo and S. Johnson, Proc. IEEE **93**, 216 (2005).

[104] M. Schulte, K. Bittkau, B. E. Pieters, S. Jorke, H. Stiebig, J. Hüpkes, and U. Rau, Prog. Photovolt: Res. Appl. **19**, 724 (2011).

[105] K. Jäger, M. Fischer, R. A. C. M. M. van Swaaij, and M. Zeman, J. Appl. Phys. **111**, 083108 (2012).

[106] G. Kirchhoff, Wied. Ann. **254**, 663 (1883).

[107] J. E. Harvey, C. L. Vernold, A. Krywonos, and P. L. Thompson, Appl. Opt. **38**, 6469 (1999).

[108] M. Plancherel and M. Leffler, Rend. Circ. Mat. Palermo **30**, 289 (1910).

[109] K. Bittkau, W. Bottler, M. Ermes, V. Smirnov, and F. Finger, J. Appl. Phys. **111**, 083101 (2012).

[110] A. F. Oskooi, D. Roundy, M. Ibanescu, P. Bermel, J. D. Joannopoulos, and S. G. Johnson, Comput. Phys. Commun. **181**, 687 (2010).

[111] K. Bittkau, Personal communication.

[112] F.-J. Haug, A. Naqavi, and C. Ballif, J. Appl. Phys. **112**, 024516 (2012).

[113] M. Nieto-Vesperinas, *Scattering and Diffraction in Physical Optics*, 2nd ed. (World Scientific Publishing Co. Pte. Ltd., Singapore, 2006).

[114] M. Burgelman, J. Verschraegen, S. Degrave, and P. Nollet, Prog. Photovolt: Res. Appl. **12**, 143 (2004).

[115] B. Pieters, *Characterization of Thin-Film Silicon Materials and Solar Cells through Numerical Modelling*, Ph.D. thesis, Technische Universiteit Delft, the Netherlands (2008).

[116] M. Zeman and J. Krc, J. Mater. Res. **23**, 889 (2008).

[117] B. Vet, B. Grancic, O. Isabella, S. Solntsev, and M. Zeman, in *24*$^{\text{th}}$ *European Photovoltaic Solar Energy Conference* (Hamburg, Germany, 2009) p. 2682.

[118] K. Bittkau and T. Beckers, Phys. Status Solidi A **207**, 661 (2010).

[119] H. Stiebig, A. Kreisel, K. Winz, N. Schultz, C. Beneking, T. Eickhoff, H. Wagner, and M. Meer, in *1994 IEEE First World Conference on Photovoltaic Energy Conversion*, Vol. 1 (Hawaii, USA, 1994) p. 603.

[120] S. Fahr, C. Rockstuhl, and F. Lederer, Appl. Phys. Lett. **92**, 171114 (2008).

[121] R. W. Gerchberg and W. O. Saxton, Optik **35**, 237 (1972).

[122] R. Dewan, V. Jovanov, C. Haase, H. Stiebig, and D. Knipp, Appl. Phys. Express **3**, 092301 (2010).

[123] M. Peters, M. Rüdiger, H. Hauser, M. Hermle, and B. Bläsi, Prog. Photovolt: Res. Appl. , DOI: 10.1002/pip.1151.

[124] M. G. Moharam and T. K. Gaylord, J. Opt. Soc. Am. **71**, 811 (1981).

[125] M. G. Moharam and T. K. Gaylord, J. Opt. Soc. Am. **72**, 1385 (1982).

[126] M. G. Moharam, D. A. Pommet, E. B. Grann, and T. K. Gaylord, J. Opt. Soc. Am. A **12**, 1077 (1995).

[127] A. Čampa, O. Isabella, R. van Erven, P. Peeters, H. Borg, J. Krč, M. Topič, and M. Zeman, Prog. Photovolt: Res. Appl. **18**, 160 (2010).

[128] J. Chandezon, G. Raoult, and D. Maystre, J. Optics **11**, 235 (1980).

[129] J. Chandezon, M. T. Dupuis, G. Cornet, and D. Maystre, J. Opt. Soc. Am. **72**, 839 (1982).

[130] E. R. Martins, J. Li, Y. Liu, J. Zhou, and T. F. Krauss, Phys. Rev. B **86**, 041404 (2012).

[131] C. Rockstuhl, S. Fahr, K. Bittkau, T. Beckers, R. Carius, F.-J. Haug, T. Söderström, C. Ballif, and F. Lederer, Opt. Express **18**, A335 (2010).

[132] R. Dewan, I. Vasilev, V. Jovanov, and D. Knipp, J. Appl. Phys. **110**, 013101 (2011).

[133] O. Isabella, S. Solntsev, D. Caratelli, and M. Zeman, Prog. Photovolt: Res. Appl. , DOI: 10.1002/pip.1257.

[134] K. Jäger, M. Fischer, R. A. C. M. M. van Swaaij, and M. Zeman, MRS Proceedings **1426**, A11_04 (2012).

[135] K. Perlin, SIGGRAPH Comput. Graph. **19**, 287 (1985).

[136] K. Perlin, Comput. Graph. **26**, 3 (2002).

[137] S. Kirkpatrick, C. D. Gelatt, and M. P. Vecchi, Science **220**, 671 (1983).

[138] V. Černý, J. Optimiz. Theory App. **45**, 41 (1985).

[139] N. Metropolis and S. Ulam, J. Amer. Stat. Assoc. **44**, 335 (1949).

[140] H. Sakai, T. Yoshida, T. Hama, and Y. Ichikawa, Jpn. J. Appl. Phys. **29**, 630 (1990).

[141] M. Python, D. Dominé, T. Söderström, F. Meillaud, and C. Ballif, Prog. Photovolt: Res. Appl. **18**, 491 (2010).

[142] C. Battaglia, J. Escarré, K. Söderström, M. Charrière, M. Despeisse, F. Haug, and C. Ballif, Nat. Photonics **5**, 535 (2011).

[143] O. Isabella, J. Krč, and M. Zeman, Appl. Phys. Lett. **97**, 101106 (2010).

[144] O. Isabella, F. Moll, J. Krč, and M. Zeman, Phys. Status Solidi A **207**, 642 (2010).

[145] M. Boccard, C. Battaglia, S. Hänni, K. Söderström, J. Escarré, S. Nicolay, F. Meillaud, M. Despeisse, and C. Ballif, Nano Lett. **12**, 1344 (2012).

[146] P. Klapetek, D. Nečas, and C. Anderson, *Gwyddion user guide* (2012), `http://www.gwyddion.net`.

[147] W. R. Tinga, W. A. G. Voss, and D. F. Blossey, J. Appl. Phys. **44**, 3897 (1973).

[148] E. Limpert, W. A. Stahel, and M. Abbt, BioScience **51**, 341 (2001).

[149] P.-J. Laurent and P. Sablonnière, Comput. Aided Geom. D. **18**, 609 (2001).

[150] C. Rabut, Comput. Aided Design **34**, 493 (2002).

[151] T. Williams and C. Kelley, *gnuplot 4.4: An Interactive Plotting Program* (2010), `http://www.gnuplot.info/documentation.html`.

[152] H. G. Katzgraber, ArXiv e-prints (2010), arXiv:1005.4117 [physics.comp-ph] .

[153] M. Zeman, J. van den Heuvel, M. Kroon, J. Willemen, B. Pieters, J. Krč, and S. Solntsev, *Advanced Semiconductor Analysis - opto-electronic simulator for amorphous and crystalline semiconductor devices – User's manual* (2011).

[154] J. C. Bowman, "High-performance multi-dimensional C++ Array class," `http://www.math.ualberta.ca/~bowman`.

Summary

Nano-textured interfaces between two media of different refractive indices scatter light. The angular distribution and the intensity of the scattered light are determined by the geometry of the nano-textures and the difference of the refractive indices of the two media.

Thin-film silicon solar cells (TFSSC), which convert sunlight directly into electricity, have nano-textured interfaces. These interfaces scatter the light incident on the solar cell. The scattering leads to a longer average path length of the photons in the absorber layer of the solar cell. Therefore more light can be absorbed and thus converted to electricity. To introduce nano-textured interfaces into the solar cells, usually transparent conductive oxide (TCO) layers are used. Some TCO materials obtain nano-textured surfaces during the production process, while others are made rough by post processing, *e.g.* by etching. Nano-textures have been successfully implemented in TFSSC for almost 30 years by academia and industry; however, theoretical investigations on the relation between the nano-textures and the scattered fields have only been performed for about ten years.

It is very important to investigate how the nano-textures can be optimised. In this thesis a scattering model is developed to tackle this important problem. The scattering model is based on the scalar scattering theory, *i.e.* it neglects the vector-character of the electromagnetic field and thus the light. Despite this strong assumption we can show that the model is suitable for simulating descriptive parameters of the scattered field in both reflection and transmission. The model is based on the fact that the transmitted field behind the nano-texture and the scattered field are related via Fourier transforms. By making simple assumptions for the transmitted field the model can be implemented using Fast Fourier transform algorithms, *i.e.* the model is very fast. The scattering model is formulated such that in principle it works at interfaces between arbitrary materials. We can successfully evaluate it for several of these interfaces. We further show that the model is also able to produce first predictions for the scattering parameters at oblique incidence. However, in this case the deviations between measured and simulated values are larger.

Combining the scattering model with the `ASA` opto-electrical device simulator allows to predict how the nano-textures affect the performance of solar-cells. This combination can also be used to perform the major motivation for the development of scattering models: To investigate how the morphology of the nano-textures can be optimised.

For this optimisation we use the "simulated annealing" optimisation algorithm. The optimisation and a subsequent evaluation reveal that the lateral feature size of the nano-textures is crucial for scattering into large angles: The smaller the lateral feature size, the more light is scattered into large angles. If, however, the lateral feature size becomes too small, less light is scattered since the nano texture then appears as effective medium. The vertical feature size hardly influences the shape of the scattered field. Nonetheless, it determines the fraction of the total light that is scattered away from the specular direction. If the rms-roughness, a measure for the vertical modulation of the texture, is kept constant, a nano-texture with the optimal lateral feature size is preferable to a texture that consists of a superposition of textures with different lateral feature sizes. However, due to the effect of the nano-textures on the electrical properties of the solar cells, a superposition of a texture consisting of large lateral and vertical features with another texture with small lateral and vertical features is preferable to a texture consisting of small lateral but large vertical features, *i.e.* sharp spikes.

The results of our work give the direction to push absorption in solar cells towards the theoretical limits.

Samenvatting

Nano-getextureerde grensoppervlakken, zoals ze tussen twee verschillende materialen kunnen voorkomen, verstrooien licht. De hoekverdeling en de intensiteit van het verstrooide licht worden door de geometrie van de nano-textuur en het verschil van de twee brekingsindices bepaald.

Dunne-film silicium zonnecellen (DFSZS), middels die zonlicht direct in elektriciteit kan worden omgezet, hebben nano-getextureerde grensoppervlakken. Deze verstrooien het invallende zonlicht. Door de verstrooiing wordt de gemiddelde weglengte van de lichtdeeltjes (fotonen) in de absorberende laag van de zonnecel vergroot. Daardoor kan meer licht geabsorbeerd en vervolgens in elektriciteit omgezet worden. Om nano-getextureerde grensoppervlakken in zonnecellen in te bouwen, worden voornamelijk laagjes van transparante geleidende oxiden (TGO) gebruikt. Sommige TGO-lagen worden door de productieproces ruw; anderen moeten in een nabehandeling ruw gemaakt worden, bijvoorbeeld door etsen. Op universiteiten en in de industrie worden nano-texturen al sinds een jaar of 30 succesvol in DFSZS toegepast. Echter de verhouding tussen nano-texturen en het verstrooide lichtveld wordt pas sinds ongeveer tien jaar theoretisch onderzocht.

Het is heel belangrijk om te weten hoe de nano-texturen geoptimaliseerd kunnen worden. In dit proefschrift gebruiken we een verstrooiingsmodel om dit belangrijke probleem te onderzoeken. Het verstrooiingsmodel is op de scalaire verstrooiingstheorie gebaseerd, waarin het vector-karakter van het elektromagnetische veld en dus het licht wordt genegeerd. Ondanks deze sterke aanname laten wij zien dat het model de descriptieve parameters van het verstrooide veld in reflectie én transmissie kan voorspellen. Het model is op het feit gebaseerd dat het getransmitteerde veld achter het verstrooiende object en het verstrooide lichtveld via Fouriertransformaties met elkaar gerelateerd zijn. Door het gebruiken van eenvoudige aannames voor het veld achter het verstrooiende object is het model zeer snel, omdat voor de implementatie *Fast Fourier transform* algoritmes gebruikt kunnen worden. Het verstrooiingsmodel is zo geformuleerd dat het in principe voor grensoppervlakken tussen willekeurige materialen werkt. Wij kunnen het dan ook met succes voor grensoppervlakken tussen verschillende materialen evalueren. Wij laten verder zien dat het model ook voorspellingen over de verstrooiingsparameters kan doen als licht onder een schuine hoek invalt. In dat geval is het verschil tussen de gemeten en de berekende waarden echter groter.

De combinatie van het verstrooiingsmodel met de `ASA` opto-elektrische simu-

latiesoftware maakt het mogelijk om het effect van de nano-getextureerde overgangen op de prestatie van DFSZC te bestuderen. Deze combinatie is noodzakelijk om aan de hoofdmotivatie voor de ontwikkeling van het verstrooiingsmodel te voldoen: Namelijk het onderzoeken hoe de morfologie van de nano-getextureerde overgangen geoptimaliseerd kan worden.

Voor deze optimalisatie gebruiken we het *simulated annealing* simulatiealgoritme. Door deze optimalisatie en een daaropvolgende evaluatie wordt duidelijk dat de grootte van de laterale kenmerken van de nano-getextureerde overgangen cruciaal is voor verstrooiing in grote hoeken: Hoe kleiner de grootte van deze laterale kenmerken, des te meer licht wordt in grote hoeken verstrooid. Indien de laterale kenmerken echter te klein worden, wordt minder licht verstrooid omdat de nano-textuur dan als een effectief medium werkt. De grootte van de verticale kenmerken beïnvloedt de vorm van het verstrooide veld nauwelijks. Hoe dan ook bepaalt ze de fractie van het licht die wordt verstrooid. Indien de ruwheid constant is, heeft een nano-textuur met een geoptimaliseerde grootte van de laterale kenmerken de voorkeur boven een textuur die uit een superpositie van texturen met verschillende groottes van laterale kenmerken bestaat. Vanwege het effect van de nano-textuur op de elektrische eigenschappen van de zonnecel kan een superpositie van een textuur met grote laterale en verticale groottes en een textuur met kleine laterale en verticale groottes echter geschikter zijn dan een textuur met kleine laterale maar grote verticale kenmerken, dus met scherpe piekjes.

De resultaten van dit werk wijzen de weg om de absorptie van licht in zonnecellen in de richting van de theoretische limiet op te schuiven.

Zusammenfassung

Nano-texturierte Grenzflächen zwischen zwei Medien mit verschiedenen Brechzahlen streuen einfallendes Licht. Die winkelabhängige Verteilung und die Intensität des gestreuten Lichtes werden durch die Geometrie der Grenzfläche und den Unterschied der zwei Brechzahlen bestimmt.

Silizium-Dünnschichtsolarzellen (SDSSZ), welche Sonnenlicht direkt in Elektrizität umwandeln, enthalten nano-texturierte Grenzflächen. Diese Grenzflächen streuen das einfallende Licht. Die Streuung führt zu einer erhöhten gemittelten optischen Weglänge in der Absorberschicht der Solarzelle. Dadurch kann mehr Licht absorbiert und folglich in Elektrizität umgewandelt werden. Meistens werden nano-texturierte Grenzflächen durch transparente, leitende Metalloxidschichten (TCO, von *engl.* transparent conductive oxides) in die Solarzelle integriert. Während manche TCO-Materialen nano-texturierte Oberflächen während des Produktionsprozesses entwickeln, werden andere durch eine Nachbehandlung, zum Beispiel ätzen, mit einer Textur versehen. Nanotexturen in SDSSZ werden schon seit etwa 30 Jahren erfolgreich von Universitäten und der Industrie angewandt; nichtsdestotrotz wird der Zusammenhang zwischen Nanotexturen und dem gestreuten Feld erst seit etwa zehn Jahren theoretisch untersucht.

Es ist sehr wichtig zu untersuchen, wie Nanotexturen optimiert werden können. In dieser Dissertation wird ein Streumodell entwickelt, um dieses wichtige Problem zu bearbeiten. Das Streumodell basiert auf der skalaren Streutheorie, die vektoriellen Eigenschaften des elektromagnetischen Feldes und damit des Lichts werden also ignoriert. Wir können zeigen, dass unser Streumodell trotz dieser starken Vereinfachungen geeignet ist, deskriptive Parameter der gestreuten Feldes in Reflexion und Transmission vorherzusagen. Das Modell baut auf der Tatsache auf, dass das transmittierte Feld hinter der Nanotextur mit dem gestreuten Feld durch Fouriertransformationen in Beziehung steht. Mittels einfacher Annahmen für das transmittierte Feld kann das Modell mit Hilfe des *Fast-Fourier-Transform*-Algorithmus numerisch implementiert werden und ist dadurch sehr schnell. Das Streumodel ist so formuliert, dass es für Grenzflächen zwischen beliebigen Materialien anwendbar ist, was wir auch erfolgreich für einige Fälle testen. Weiters zeigen wir, dass das Model eine erste Abschätzung für die Streuparameter liefern kann, wenn das Licht unter einem Winkel ungleich 90° auf die Grenzfläche auftrifft. Bei dieser Anwendung ist die Abweichung zwischen gemessenen und simulierten Streuparametern jedoch größer.

Die Kombination des Streumodells mit der opto-elektrischen Simulationssoft-

ware ASA erlaubt es uns vorherzusagen, wie die Nanotexturen die Leistungsmerkmale der Solarzelle beeinflußen. Diese Kombination kann auch benützt werden, um die Hauptmotivation für die Entwicklung des Streumodells in Angriff zu nehmen: Nämlich zu untersuchen, wie die Morphologie der Nanotexturen optimiert werden kann.

Für die Optimierungen benützen wir mit den *Simulated-Annealing*-Algorithmus. Durch die Optimierungen und eine anschließende Evaluierung wird deutlich, dass die laterale Größenordnung der Nanotexturen entscheidend für Streuung in große Winkel ist: Je kleiner die laterale Strukturen, desto mehr Licht wird in große Winkel gestreut. Zu kleine laterale Größenordnungen streuen jedoch weniger Licht, da die Nanotexturen dem Licht dann als effektives Medium erscheinen. Die vertikale Größenordnung der Nanotextur beeinflusst die Form des gestreuten Feldes kaum, aber sie kontrolliert den Anteil des Lichts, der von der Hauptrichtung weggestreut wird. Wird die rms-Rauheit, ein Maß für die vertikale Modulation der Textur, konstant gehalten, so ist eine Nanotextur mit optimierter lateraler Größenordnung einer Textur zu bevorzugen, welche aus einer Überlagerung von Texturen mit verschiedenen lateralen Größenordnungen hervorgeht. Da die Nanotextur auch die elektrischen Eigenschaften der Solarzelle beeinflusst, kann eine Superposition von einer Textur mit großen lateralen und vertikalen Größenordnungen mit einer Textur mit kleinen lateralen und vertikalen Größenordnungen jedoch einer Textur überlegen sein, die kleine laterale und große vertikale Größenordnungen aufweist, also scharfe Zacken hat.

Die Ergebnisse unserer Arbeit weisen den Weg, die Absorption des Sonnenlichtes in Solarzellen näher an das theoretische Limit zu bringen.

Publications related to this thesis

Peer-reviewed journal publications

1. **K. Jäger**, M. Fischer, R. A. C. M. M. van Swaaij, and M. Zeman, *A scattering model for nano-textured interfaces and its application in opto-electrical simulations of thin-film silicon solar cells*, J. Appl. Phys. **111**, 083108 (2012).

2. M. Schulte, K. Bittkau, **K. Jäger**, M. Ermes, M. Zeman, and B. E. Pieters, *Angular resolved scattering by a nano-textured ZnO/silicon interface*, Appl. Phys. Lett. **99**, 111107 (2011).

3. **K. Jäger**, O. Isabella, R. A. C. M. M. van Swaaij, and M. Zeman, *Angular resolved scattering measurements of nano-textured substrates in a broad wavelength range*, Meas. Sci. Technol. **22**, 105601 (2011).

4. J. A. Sap, O. Isabella, **K. Jäger**, and M. Zeman, *Extraction of optical properties of flat and surface-textured transparent conductive oxide films in a broad wavelength range*, Thin Solid Films **520**, 1096 (2011).

5. **K. Jäger** and M. Zeman, *A scattering model for surface-textured thin films*, Appl. Phys. Lett. **95**, 111708 (2009).

Oral presentations at conferences and workshops

6. **K. Jäger**, R. A. C. M. M. van Swaaij, and M. Zeman, *The Scalar Scattering Theory: A Multi-Functional Tool for Optimizing Scattering in Thin-Film Silicon Solar Cells*, OSA Topical Meeting on Optical Nanostructures and Advanced Materials for Photovoltaics, Eindhoven, the Netherlands, November 2012, p. PT3C.7.

7. **K. Jäger**, M. Fischer, R. A. C. M. M. van Swaaij, and M. Zeman, *An algorithm for finding optimized interface morphologies in thin film silicon solar cells*, MRS Spring Meeting, San Francisco, California, April 2012; MRS Proceedings **1426**, A11-04 (2012).

8. **K. Jäger**, R. A. C. M. M. van Swaaij, and M. Zeman, *A full scalar scattering model for nano-textured interfaces*, OSA Topical Meeting on Optical Nanostructures and Advanced Materials for Photovoltaics, Austin, Texas, November 2011, p. PWC5.

9. **K. Jäger**, M. Fischer, M. Abatzis, R. A. C. M. M. van Swaaij, S. Solntsev, and M. Zeman, *A Full Scattering Model for Integrated Opto-Electrical Modelling of Solar Cells*, 26th European Photovoltaic Solar Energy Conference, Hamburg, Germany, September 2011, p. 3BO.1.1.

10. **K. Jäger**, M. Schulte, K. Bittkau, A. M. Ermes, M. Zeman, and B. E. Pieters, *Optical scattering properties of a nano-textured ZnO-silicon interface*, International Conference on Applications of Optics and Photonics, Braga, Portugal, May 2011; Proc. SPIE **8001**, 800106 (2011).

11. **K. Jäger**, O. Isabella, R. Santbergen, R. Liang, S. Solntsev, J. Krč, R. A. C. M. M. van Swaaij, and M. Zeman, *Light Trapping Techniques in Thin-Film Silicon Solar Cells*, Colloquium Optische Spektrometrie, Berlin, Germany, March 2011.

12. **K. Jäger**, *The photovoltaic effect and solar cells*, Colloquium Optische Spektrometrie, Berlin, Germany, March 2011.

13. **K. Jäger** and M. Zeman, *A Scattering Model for Transparent Thin Films with Surface Textures*, OSA Topical Meeting on Solar Energy, Tucson, Arizona, June 2010, p. STuC3.

14. **K. Jäger**, O. Isabella, R. Santbergen and M. Zeman, *Light management in thin-film silicon solar cells*, UV/Vis/NIR Spectroscopy Seminar/Workshop, Eindhoven, the Netherlands, October 2009.

Poster presentations at conferences and workshops

15. **K. Jäger**, M. Fischer, R. A. C. M. M. van Swaaij, and M. Zeman, *A scattering model for improving the performance of thin film silicon solar cells*, 2nd Colloquium of the Munich School of Engineering, Munich, Germany, June 2012.

16. **K. Jäger**, M. Fischer, R. A. C. M. M. van Swaaij, and M. Zeman, *Scattering by nano-textured interfaces modelled using the scalar scattering theory*, International Workshop on Modeling of Thin-Film Silicon Solar Cells, Oldenburg, Germany, February 2012.

17. **K. Jäger**, R. A. C. M. M. van Swaaij, and M. Zeman, *Modelling transmitted scattering at transparent surface-textured thin films*, Fysica 2010 – Annual conference of the Dutch Physical Society, Utrecht, the Netherlands, April 2010.

18. **K. Jäger** and M. Zeman, *Modeling scattering properties of roughly textured TCO layers*, Proceedings of the 12th Annual Workshop on Semiconductors for Future Electronics, Veldhoven, the Netherlands, November 2009, p. 153.

19. **K. Jäger**, L. Zhao, O. Isabella and M. Zeman, *Light scattering properties of surface-textured TCO layers*, 23rd International Conference on Amorphous and Nanocrystalline Semiconductors, Utrecht, the Netherlands, August 2009; Phys. Status Solidi C **7**, 945 (2010).

20. **K. Jäger**, L. Zhao, and M. Zeman, *A promising approach to model optical properties of transparent conductive oxides*, Fysica 2009 – Annual conference of the Dutch Physical Society, Groningen, the Netherlands, April 2009.

Other contributions to conferences and workshops

21. M. Zeman, O. Isabella, **K. Jäger**, R. Santbergen, S. Solntsev, M. Topic, and J. Krč, *Advanced light management approaches for thin-film silicon solar cells*, International Conference on Materials for Advanced Technologies, Singapore, June 2011.

22. M. Zeman, O. Isabella, **K. Jäger**, P. Babal, S. Solntsev, and R. Santbergen, *Modeling of Advanced Light Trapping Approaches in Thin-Film Silicon Solar Cells*, MRS Spring Meeting, San Francisco, California, April 2011.

23. M. Zeman, O. Isabella, **K. Jäger**, R. Santbergen, S. Solntsev, and J. Krč, *Advanced Light Trapping in Thin-Film Silicon Solar Cells*, MRS Spring Meeting, San Francisco, California, April 2010.

24. O. Isabella, **K. Jäger**, J. Krč, and M. Zeman, *Light scattering properties of surface-textured substrates for thin-film solar cells*, Proceedings of the 11th Annual Workshop on Semiconductor Advances for Future Electronics and Sensors, Veldhoven, the Netherlands, Novemver 2008, p. 476.

25. O. Isabella, **K. Jäger**, J. Krč, and M. Zeman, *Light management in thin-film silicon solar cells*, A look inside solar cells (Workshop), Ascona, Switzerland, November 2008.

Curriculum vitae

Klaus Jäger was born in the Austrian town of Wörgl in 1983. After receiving his maturity diploma from the Bundesrealgymnasium Wörgl in 2001, he started studying physics, mathematics and philosophy at the University of Innsbruck, Austria. In 2003 he continued his studies of physics at the Swiss Federal Institute of Technology Zurich, from where he graduated as Master of Science ETH in 2008. While always having been interested in theoretical physics, he started to develop a profound interest in renewable energy. During his diploma (MSc) project he could combine those two fields: he used Monte Carlo methods to simulate absorption and scattering of light in poly-dispersions that are present in high temperature solar reactors. With such reactors solar energy can be stored in chemical fuels such as elementary zinc or hydrogen. In 2008, Klaus started working as a PhD student in the Photovoltaic Materials and Devices Laboratory at the Delft University of Technology in the Netherlands. His PhD project was focused on developing and testing scattering models that allow to predict the influence of nano-textured interfaces on the performance of thin-film solar cells. Such models can help to increase the photocurrent and hence the efficiency of thin film solar cells. Klaus is a member of the Nederlandse Natuurkundige Vereniging (NNV) and the Optical Society of America (OSA).